

# Interferometric Millimeter Observations of the High Energy Universe

Thesis by  
Nitika Yadlapalli

In Partial Fulfillment of the Requirements for the  
Degree of  
Doctor of Philosophy

The logo for the California Institute of Technology (Caltech), featuring the word "Caltech" in a bold, orange, sans-serif font.

CALIFORNIA INSTITUTE OF TECHNOLOGY  
Pasadena, California

2024  
Defended June 30, 2023

© 2024

Nitika Yadlapalli

ORCID: 0000-0003-3255-461

All rights reserved except where otherwise noted

## ACKNOWLEDGEMENTS

First and foremost, I am most grateful to my advisor, Vikram Ravi. When I first arrived at Caltech, I had next to no idea what I wanted to do but you helped me flourish into the fully fledged radio astronomer I am today. Through these last five years, I have deeply appreciated both the research guidance and life advice you have given me. Thank you for always having the enthusiasm for both of us on the days I could not find it for myself, for always believing in my abilities, and for propelling me forward into the next phase of my career.

Thank you as well to my co-advisor, Katie Bouman. When we first started working together, you pulled me out of a research slump I had sunken into in the midst of COVID. You gave me back joy and momentum for research during a difficult time and believed in me to no end as I found my footing within the EHT collaboration.

I also wish to extend my deepest thanks to the entire staff of the Owens Valley Radio Observatory, without whom nothing could have succeeded on SPRITE. I owe particular gratitude to Mark Hodges and James Lamb, who always made time for me on countless OVRO visits, Zoom meetings, and impromptu phone calls. It has been a privilege to learn from your knowledge and experience and I hope one day I know even half as much about radio telescopes as you both seem to.

To my fiancé, Dominic—I always knew I would leave graduate school with my PhD but I never dreamed I would also be leaving with my life partner. You have watched me put so much into this thesis, just as I have watched you put so much into yours. I am so excited to see where our journey is going from here.

Finally, I owe this degree to all of the brilliant women who preceded me in this field. I am truly standing on the shoulders of giants.

## ABSTRACT

This thesis explores what can be accomplished in the ways of time-domain astrophysics with a variety of scales of millimeter interferometry. I touch upon techniques in instrumentation, theory, observation, and computation, showcasing the breadth and richness of the field.

The transient millimeter sky is largely comprised of synchrotron sources whose physical properties are just beginning to be revealed. We are entering an age where new wide-field surveys will exponentially increase the number of known transients, including the first wide-field millimeter survey capable of significant transient detections. As we approach this era, resources dedicated to monitoring and follow-up become increasingly more important.

A significant part of my work involves design and commissioning for a new single-baseline millimeter interferometer at the Owens Valley Radio Observatory called SPRITE. Uniquely positioned as a dedicated transient follow-up telescope, SPRITE has the ability to observe nearby transients with a relatively high cadence. In this thesis, I also highlight two specific classes of sources for which millimeter observations may be particularly interesting. I present predictions for millimeter emission from supernovae interacting with dense circumstellar media and discuss their rates of detection in upcoming surveys. I additionally present lower frequency spatially-resolved radio observations of an X-ray binary in an active state.

On the other extreme, this thesis also explores the use of very long baseline interferometry to investigate how high resolution images of supermassive black holes vary over the timescale of a year. In 2017, the Event Horizon Telescope Collaboration (EHTC) observed the supermassive black hole in nearby galaxy M87, producing the first resolved image of the shadow of a black hole and potentially revealing intra-day variability of the observed synchrotron emission around the shadow. I present work on the imaging and preliminary analysis of the 2018 epoch of EHT observations of the black hole in M87, and discuss the EHTC's conclusions of intra-day and year-long variations in the images.

## PUBLISHED CONTENT AND CONTRIBUTIONS

Yadlapalli, N., V. Ravi, and A. Y. Q. Ho (July 2022). “Models of Millimeter and Radio Emission from Interacting Supernovae”. In: *The Astrophysical Journal* 934.1, 5, p. 5. DOI: 10.3847/1538-4357/ac771f. arXiv: 2206.03518 [astro-ph.HE].

N.Y. participated in the calculation and application of models presented in this work as well as the preparation of the manuscript.

Yadlapalli, N. et al. (Mar. 2021). “VLBA Discovery of a Resolved Source in the Candidate Black Hole X-Ray Binary AT2019wey”. In: *The Astrophysical Journal Letters* 909.2, L27, p. L27. DOI: 10.3847/2041-8213/abea19. arXiv: 2012.13426 [astro-ph.HE].

N.Y. participated in the calibration, reduction, and analysis of the data presented in this work along with the preparation of the manuscript.

## TABLE OF CONTENTS

Acknowledgements . . . . .	iii
Abstract . . . . .	iv
Published Content and Contributions . . . . .	v
Table of Contents . . . . .	v
List of Illustrations . . . . .	viii
List of Tables . . . . .	xviii
Chapter I: Introduction . . . . .	1
1.1 The High-Energy Millimeter Sky . . . . .	1
1.2 Challenges Facing Millimeter Telescopes . . . . .	5
1.3 Millimeter Interferometry at the Owens Valley: A Historical Perspective . . . . .	7
1.4 Very Long Baseline Interferometry at Millimeter Wavelengths . . . . .	9
1.5 Thesis Outline . . . . .	10
Chapter II: Commissioning the Stokes Polarization Radio Interferometer for Time-Domain Experiments (SPRITE) . . . . .	12
2.1 Introduction . . . . .	12
2.2 Instrument Overview . . . . .	13
2.3 Observing Strategy . . . . .	25
2.4 Commissioning observations . . . . .	29
2.5 Future Observations . . . . .	34
2.6 Conclusion . . . . .	35
2.7 Acknowledgements . . . . .	36
Chapter III: Models of Millimeter and Radio Emission from Interacting Supernovae . . . . .	37
3.1 Introduction . . . . .	37
3.2 Model Summary . . . . .	41
3.3 Application to Type II <sub>n</sub> /Ib <sub>n</sub> Supernovae . . . . .	46
3.4 Rates of Detection in Blind Surveys . . . . .	53
3.5 Conclusion . . . . .	56
Chapter IV: VLBA Discovery of a Resolved Source in the Candidate Black Hole X-Ray Binary AT2019wey . . . . .	58
4.1 Introduction . . . . .	58
4.2 Observation and Analysis Procedures . . . . .	61
4.3 Results . . . . .	63
4.4 Discussion . . . . .	66
4.5 Conclusion . . . . .	67
Chapter V: Imaging the Supermassive Black Hole in M87 with 2018 Event Horizon Telescope Observations . . . . .	69
5.1 Introduction . . . . .	69

5.2 Description of Observations . . . . .	71
5.3 Pre-Imaging Analysis . . . . .	74
5.4 Imaging Using Regularized Maximum Likelihood . . . . .	79
5.5 Presentation and Analysis of Images . . . . .	84
5.6 Conclusion . . . . .	92
Chapter VI: The Road Ahead . . . . .	93
Bibliography . . . . .	96
Appendix A: SPRITE User Manual . . . . .	116
A.1 Introduction . . . . .	116
A.2 Controlling the Antennas . . . . .	118
A.3 Running the Correlator . . . . .	125
A.4 Receiver Calibration Procedures . . . . .	127
A.5 Antenna Calibration Procedures . . . . .	133
A.6 Setting up an Observation . . . . .	141
A.7 Reducing Observations . . . . .	145
A.8 Putting It All Together: Observing Checklist . . . . .	145
Appendix B: EHT Synthetic Data Generation Tutorial . . . . .	147

## LIST OF ILLUSTRATIONS

<i>Number</i>	<i>Page</i>
1.1 Atmospheric opacity at zenith as a function of observing wavelength. $W_V$ represents total precipitable water vapor in units of millimeters. Reproduced from Findlay, 1971. . . . .	7
1.2 Two Leighton antennas that comprise the single baseline of SPRITE.	8
2.1 Example of data collected on 23 stars for calculation of the optical pointing model coefficients. <i>Top</i> : The smaller, darker markers shown are the true locations and offsets of the stars measured with each antenna. The larger, lighter markers show the pointing coefficients that best reproduce the observed offsets. <i>Bottom</i> : Residuals for the fit shown in the top panel, showing that there is no directional dependence to the fidelity of the model fitting. . . . .	15
2.2 Example of data collected on Jupiter for single dish radio pointing measurements. Light curves are shown for both antennas from scans in both the x- and y-directions across the disk of the planet, which are represented by the first and second portion of the light curves, respectively. This scan measured offsets of $\pm 90$ arcseconds at 10 arcsecond increments. . . . .	16
2.3 Diagram showing how the LO signal for the SIS mixer is generated. The components within the dotted box are located in the basement of the Mayer control building and are one set of components shared between both antennas. Signals leaving the Mayer control building are sent out over optical fiber and modulated back to RF within each of the antennas. The components within the dashed line represent the system in the sidecab of Antenna 2 only. In Antenna 1, the dashed box is replaced by a single synthesizer that generates a 50 MHz signal.	17



- 2.4 Diagram of the SPRITE 2nd stage downconversion system showing how IF signals from both antennas are split into high and low band components to be fed to their respective ROACH2 boards for correlation. The bold arrows represent input signals to the downconverter as well as output signals to the ROACH2. The thick dotted lines indicate clocking signals. One of our ROACH2 boards contains two inputs for two clock signals whereas the other ROACH2 board contains only one clock signal input and splits the signal internally. . . . . 20
- 2.5 Red Pitaya firmware block diagram generated in Simulink. This firmware utilizes the CASPER toolbox blocks as well as Xilinx FPGA blocks. The bottom portion of the diagram shows the main phase adjustment blocks. The signal is read through the ADC and split into two paths: one for the cosine representation of the signal and one is manipulated to extract the sine representation of the signal. Each portion is then multiplied by their respective coefficients defining the phase shift, as defined in Equation 2.5. The calculation of the coefficients at each time step is shown in the top portion of the diagram. The block labelled "phi\_init" controls the quadrature phase switching while the block labelled "phi\_step" controls the fringe rate. For each time step, the total amount to shift the input signal phase is computed and the cosine and sine values of that phase read from pre-programmed BRAM blocks. The output shifted signal is read out on one of the DAC ports while the original un-shifted signal is read out on the second DAC port for testing purposes. See this diagram as well as the original files at <https://github.com/nitikayad96/SPRITE/blob/main/firmware> . . . . . 22
- 2.6 Locations of all sources allowed for use as gain calibrators for SPRITE science observations overlaid on a Mollweide projection of a 100 GHz all-sky map (with the CMB subtracted) created with observations from the *Planck* High Frequency Instrument (Planck Collaboration et al., 2020). The gray points represent sources taken from the ALMA calibrator list while blue points represent sources used as calibrators for CARMA. The red points represent a few science targets of interest located at a variety of coordinates to demonstrate the broad availability of calibrator sources. . . . . 24

2.7	Measurements of elevation dependent double-sideband system temperature of the SPRITE baseline in reasonable weather conditions. Each measurement contains the $T_{\text{sys}}$ of both the high band and low band, shown as dots connected by a line. . . . .	29
2.8	Time averaged spectrum of SiO maser emission in R Leo, zoomed in to corresponding frequencies in both the upper and lower sideband, after sideband separation, shown with and without cross-talk mitigation using $180^\circ$ phase switching. . . . .	29
2.9	Behavior of phase as a function of time and frequency as seen on a 2 hour observation of bandpass calibrator source 3C84 after refinements to the baseline solution. In the bottom panel, red indicates negative phase, blue indicates positive phase, and white indicates zero phase. The top panel of this figure shows the small amount of delay variations over the whole observation. The middle panel shows a band-averaged measurement of phase as a function of time. . . . .	31
2.10	SPRITE measurements of the flux density of ALMA calibrator source J1342+2709 (red points). An ALMA measurement obtained 36 days earlier is indicated as a black line ( $1\sigma$ uncertainty shown as a blue shaded region). . . . .	32
2.11	SPRITE measurements of the flux density of the flaring BL Lac object S2 0109+22 (top) and the binary classical T Tauri system DQ Tau (bottom). The blue shaded region in the bottom panel indicates an approximate quiescent level for the 90 GHz emission from DQ Tau (see text for details). . . . .	33
3.1	Reproduction of 8.5 GHz light curves of four type II <sub>n</sub> SNe. This is meant to show the diversity of light curves that have been observed, highlighting the challenge in constraining a single progenitor model for these events. The data for these was taken from Chandra et al., 2012; Dwarkadas et al., 2016; Chandra et al., 2015; Margutti et al., 2014. . . . .	40

- 3.2 Light curves at 10 GHz and 100 GHz of synchrotron emission originating in the forward shock of an interacting supernova. Three absorption cases are shown here: SSA only, SSA + FFA assuming a  $10^5$  K CSM, and SSA + FFA assuming a  $10^4$  K CSM. The extent of the ionized region contributing to FFA is calculated given the shock breakout pulse properties. We use progenitor radii of  $500 R_{\odot}$  (RSG),  $70 R_{\odot}$  (BSG), and  $5 R_{\odot}$  (WR) and pulse luminosities as shown in Figure 5 of Nakar and Sari, 2010. We use steady wind velocities of 20 km/s (RSG), 250 km/s (BSG), and 1000 km/s (WR). The RSG and BSG scenarios represent type II In SNe while the WR scenario represents a type Ib In SNe. For the 100 GHz light curves, we show a zoomed in panel of the first 250 days to better visualize the time scale of the millimeter peaks. For scale,  $\sim 10^{28}$  erg s $^{-1}$  Hz $^{-1}$  is about 1 mJy at  $\sim 100$  Mpc. . . . . 47
- 3.3 Light curves at 100 GHz (solid lines) and 10 GHz (dashed lines) showing the effects of different ejecta and CSM radial profiles. Adopting an RSG progenitor model and keeping constant  $\dot{M} = 10^{-3} M_{\odot}/\text{yr}$ ,  $T_e = 10^4$  K,  $E = 10^{51}$  ergs, and  $M_{ej} = 5 M_{\odot}$ , the upper panel assumes  $s = 2$  and varies the ejecta profile index,  $n$ , while the middle panel assumes  $n = 10$  and varies the CSM profile index,  $s$ . The bottom panel assumes  $s = 2$  and  $n = 10$  and varies the explosion energy. . . . . 49
- 3.4 Corner plot showing posterior distributions of parameters used to generate a best fit model light curve for the 8.5 GHz data of SN 2006jd. Not all of the parameters are well constrained in this analysis, indicating that late time radio data alone is not sufficient to understand these events. . . . . 51

3.5	Light curves at 8.5 GHz generated from 200 random samples from the MCMC fit to the SN 2006jd data. Using the same random samples, light curves are also generated at 100 GHz. Using all 2000 samples generated in our MCMC analysis, the mean peak location of the 8.5 GHz light curves occurs around 794 days, with a $1\sigma$ spread of 23 days. The mean peak location of all 100 GHz light curves occurs around 61 days with $1\sigma = 15$ days. The potential for detecting the millimeter light curve peak demonstrated here highlights the need for sensitive and early-time follow up observations of sources such as SN 2006jd. . . . .	52
3.6	Areal densities of interacting SNe as a function of their flux densities for various progenitor models. Three mass loss rates are depicted, $\dot{M} = 10^{-2} M_{\odot}/\text{yr}$ , $\dot{M} = 10^{-3} M_{\odot}/\text{yr}$ , and $\dot{M} = 10^{-4} M_{\odot}/\text{yr}$ . All models have values of $T_e = 10^4$ K, $E = 10^{51}$ ergs, $M_{ej} = 5 M_{\odot}$ , $n=10$ , and $s=2$ . Also shown are limiting areal densities for the $5\sigma$ detection thresholds for four different CMB surveys. For comparison, areal densities of other millimeter-bright astrophysical events are also included. The line for AT2018cow is generated using values given in Ho et al., 2021, while the lines for on-axis long gamma-ray bursts (LGRB) and on-axis tidal disruption events (TDE) use values given in Eftekhari et al., 2022. . . . .	54
4.1	Lightcurves showing radio observations (scaled to 4.8 GHz) and X-ray observations from MAXI (2-10 keV). The stars on the plot show the observations discussed in this work. . . . .	61
4.2	CLEAN images of the phase reference (top row), J0418+5457, and the check source (bottom row), 0423+561, for both epochs. The images are consistent with point sources. Also depicted on the images are 15% and 50% flux density contours. . . . .	62
4.3	CLEAN images of AT2019wey for both epochs with 15% and 50% flux density contours. The red dotted line represents the single best fit deconvolved ellipse across both epochs for the source. . . . .	63
4.4	UV-amplitudes of AT2019wey for both epochs, with colorized points representing different baseline pairs. . . . .	64

4.5	Model parameters derived for a Gaussian image plane fit to hour long observation blocks of AT2019wey. All of the geometric parameters are estimations of a deconvolved component. Top left: flux density, top right: position angle measured east of north, bottom left: major axis, bottom right: minor axis. . . . .	65
5.1	The $(u, v)$ -coverage of the EHT observations of M87* for days 2018 April 21 and 2018 April 25. The colored points represent 2018 observations while the light grey points represent $(u, v)$ -coverage of the 2017 April 11 observations. Bands 3 and 2 are shown to visualize the impact of the GLT baselines. . . . .	74
5.2	The visibility amplitudes of the M87* observations as a function of $(u, v)$ -distance. We show results from band 3 on both 2018 April 21 and 2018 April 25 using data from two calibration pipelines, with error bars to signify $\pm 1\sigma$ uncertainty. The light grey points represent amplitudes measured on 2017 April 11 while the black dashed line represents model visibility amplitudes for a symmetric thin ring with diameter equal to $42 \mu\text{as}$ . . . . .	75
5.3	Ground truth image of geometric ring model utilized in synthetic training data. The left panel depicts a field of view (FOV) of $130 \mu\text{as}$ , showing only the compact structure of the synthetic data. The right panel depicts a logarithmic-scale representation of the extended jet feature (FOV = $2900 \mu\text{as}$ ) added to all of the synthetic data sets, visualizing the scale of the extended jet in relation to the compact source. . . . .	78
5.4	The representative images recovered from the HOPS data with all five imaging pipelines for two observing days (April 21 and 25). Each panel shows the fiducial image of the corresponding top set images for DIFMAP, eht-imaging, and SMILI pipelines, and a random sample from the respective posterior for THEMIS and Comrade pipeline. We do not have top sets for band 1 and band 2 from DIFMAP, eht-imaging, and SMILI pipelines on April 25. . . . .	85

- 5.5 Four training geometric models as imaged by each method. The first row shows the visibility amplitudes of the model compared to the visibility amplitudes measured for M87. The second row shows the ground-truth images. The DIFMAP, eht-imaging, and SMILI rows show a fiducial image made from the same parameter sets as the images shown in Fig. 5.4. The THEMIS and Comrade rows show a random draw from the posterior. . . . . 86
- 5.6 Seven geometric validation models plus one GRMHD snapshot as imaged by each method. The first row shows the visibility amplitudes of the model compared to the visibility amplitudes measured for M87. The second row shows the ground-truth images. The DIFMAP, eht-imaging, and SMILI rows show a fiducial image made from the same parameter sets as the images shown in Fig. 5.4. The THEMIS and Comrade rows show a random draw from the posterior. . . . . 87

- 5.7 Visualization of image statistics calculated using the top set images from the `eht-imaging` pipeline for observations taken on April 21 band 3. We emphasize that these images do not represent the posterior probability space for the reconstructions. Each image reconstructed using `eht-imaging` is the maximum a posteriori (MAP) image for a given parameter set. Thus, the statistics shown represent uncertainties that arise from difference choices of regularizer weights, not from an exploration of posterior space. The top row shows top statistics in the image domain while the bottom row shows the visibility domain. Overlaid on the visibility domain panels is the  $(u, v)$ -coverage for the April 21 observation. From left to right, we present the mean image; the standard deviation; the normalized standard deviation, calculated by re-scaling each image to the flux of the mean image; and the fractional standard deviation, calculated by dividing the standard deviation by the mean. The fractional standard deviation panel has been clipped to a maximum value of 1. Portions of the image exhibit large fractional standard deviations due to pixel values very close to zero in the mean image. In the top row, image contours are drawn at 10%, 20%, 40%, and 80% of the peak values from the mean image. In the bottom row, the grey contours represent 0.1%, 1%, and 10% of the peak while the black contours represent 10 and 100 mJy (left three panels) and 0.1 (right most panel). The complex visibilities are calculated by taking a Fourier transform of the images and then we calculated the mean and standard deviation. The absolute value of the mean and standard deviation of complex visibilities is taken to calculate visibility amplitudes. . . . . 90
- 5.8 Representative example images of M87\* from the EHT observations taken on 2017 April 11 and 2018 April 21 (north is up and east is to the left). The 2017 image is generated with the average of fiducial parameter sets using `DIFMAP`, `eht-imaging`, and `SMILI` (Event Horizon Telescope Collaboration et al., 2019d). The 2018 image is created by taking the average of images generated and blurred from `DIFMAP`, `eht-imaging`, `SMILI`, `THEMIS`, and `Comrade`. Comparison of the images shows consistency in ring width and diameter across the observations. . . . . 91

6.1	Nitika, pictured in front of the two SPRITE antennas, at the end of a long and happy day of work at OVRO. . . . .	94
A.1	A screenshot of the COMAP control system used for controlling C1 and C2 . . . . .	119
A.2	The telnet command line interface used for power cycling the antenna computers . . . . .	121
A.3	LabVIEW program to interface with CAN modules that deal with monitor and control for C1 and C2 . . . . .	124
A.4	Diagram describing how the LO reference signal for the SIS mixers is generated. It begins with a 10 MHz reference signal, generated by the master clock in the Meyer Building basement. Following the bottom branch of this diagram, this signal serves as the reference for a low phase noise synthesizer, also located in the Meyer building basement. The signal from this synthesizer is multiplied and a specific harmonic is selected and locked with the phase lock loop (PLL). Once the oscillator is locked, its signal can be multiplied again and mixed with the 50 MHz reference signal from the lobe rotator to serve as the input signal to the phase locking loop responsible for locking the Gunn oscillator. This final output signal from the Gunn will be used as the LO for the SIS mixer. The fact that the PLLs in both antennas are referenced by a mutual master clock ensures that the LO reference signals being generated by the SIS mixer do not have a significant phase difference between them - this prevents decoherence of the correlated visibility signals later. (Diagram drawn by James Lamb) . . . . .	128
A.5	CAN Node API 184, showing the status of the LO reference signal . . . . .	130
A.6	CAN Node API 080, showing the status of the YIG oscillator . . . . .	130
A.7	CAN Node API 016, showing the status of the Gunn oscillator . . . . .	131



A.8	A diagram, reproduced from (Phillips and Woody, 1982), of SIS mixer behavior. The left panel (a) shows a diagram of electron density of states as a function of electron energy. As characteristic of superconducting materials, there is an energy gap where the density of states is zero. The right panel (b) shows the amount of currently across the junction as a function of the bias voltage. When the bias voltage is 0, the energy gaps completely overlap, so there are no empty states for electrons to tunnel to from one superconducting layer to the other. As the you increase the bias voltage, there is a shallow linear relationship between voltage and current. However, as the bias voltage reaches a value such that the energy gaps are completely offset from each other, the amount of current across the junction sharply increases and the linear slope steepens. The voltage that triggers this sharp increase is the ideal bias voltage for the mixer. To see a practical example, refer to the IV curve of antenna 1 in Figure A.9. . . . .	132
A.9	CAN Node API 209, showing the options for tuning the receiver and taking an IV curve of the receiver. . . . .	133
A.10	CAN Node APIs 070 and 224, showing the panels for controlling the telescope optics and the PAM. . . . .	134
A.11	An example output file from the <code>process_tilts.py</code> script . . . . .	135
A.12	Frame Grabber utility in COMAP control system . . . . .	138
A.13	Recorded power in the correlator vs time as each antenna sweeps through offsets in increments of 10 arcseconds between -1 and 1 arcminute across the disk of Jupiter. The black dotted lines demarcate the transition between stepping through offsets in x and offsets in y. The light blue dotted lines represent times where the telescope is passing through zero offsets. The top panel represents antenna 1 and the bottom panel represents antenna 2. . . . .	139
A.14	Message structure for CAN over IP communication . . . . .	143
A.15	Message structure for CAN ID bytes, using an example of controlling the ambient load of the antenna. . . . .	144

## LIST OF TABLES

<i>Number</i>	<i>Page</i>
4.1 Properties for AT2019wey, approximating the source structure as a 2D Gaussian. Though this geometry does not reflect the true source structure, more complex features cannot be extracted from these observations. . . . .	63
5.1 Parameters of three Gaussians used to simulate the presence of a large scale jet in EHT 2018 synthetic datasets. . . . .	78
5.2 Gain perturbation values for each station for the 2018 EHT M87* observations. . . . .	79
5.3 Parameters and their surveyed values for the eht-imaging pipeline for April 21 band 3 data. . . . .	88
5.4 Closure quantity $\chi^2$ values for the fiducial M87* images and $\chi^2$ statistics (mean and standard deviation) for Top Set images. $\chi^2$ values with systematic uncertainties of 0%, 1%, and 10% are shown.	89
5.5 Comparison of the image-domain extracted ring parameters for 2017 and 2018. . . . .	91

*Chapter 1*

## INTRODUCTION

Time-domain astronomy is flourishing in our era, with existing and future wide-field surveys across many wavelengths seeking to push the limits of survey depth and cadence. Caltech has been particularly fortunate to lead the efforts on many of these cutting edge telescopes. Atop Palomar Mountain, the long-running Palomar Transient Factory (Law et al., 2009) and the more modern Zwicky Transient Facility (Bellm et al., 2019) have transformed the field of optically discovered transients, paving the way for the success of large scale experiments such as the upcoming Vera Rubin Observatory. Also located at Palomar, novel wide-field infrared experiments Gattini-IR (De et al., 2020) and the Wide-field Infrared Transient Explorer (Lourie et al., 2020) are making strides in exploring the infrared sky.

Pushing further to longer wavelengths, the Owens Valley Radio Observatory (OVRO) has seen its own rise of transient resources cropping up in the past few years. With experiments such as STARE-2 (Bochenek et al., 2020) and the Deep Synoptic Array (Kocz et al., 2019) pushing forward the search for millisecond fast radio bursts and the low-frequency transient search with the Long Wavelength Array (LWA; Anderson et al., 2019), OVRO has already been proving its prowess in unveiling the transient radio sky. Future telescopes such as Galactic Radio Explorer (Connor et al., 2021) and DSA-2000 (Hallinan et al., 2019) are already in the works to push beyond these initial successes into the burgeoning era of radio transient discovery. This work in particular will focus on a closely related, but as yet underexplored regime of the electromagnetic spectrum: millimeter wavelengths.

**1.1 The High-Energy Millimeter Sky**

Astronomical millimeter emitting sources can vary on timescales ranging from seconds to years and have both galactic and extragalactic origins. The primary mechanism of millimeter emission from high energy sources is synchrotron emission generated by relativistic shocks interacting with a surrounding medium. Observations of synchrotron emission provide us with valuable insight into physical properties of sources, including energy, size, magnetic field strength, and electron energy distribution. These quantities all help us build a complete picture of the mechanisms behind and dynamics of explosive events, with millimeter observations

providing particularly compelling evidence. The peak frequency of the synchrotron spectrum for a source typically begins at higher frequencies and cascades down to lower ones as the shock wave expands and decelerates—thus, observations at millimeter wavelengths uniquely probe shock interactions at earlier times than lower frequency observations. In the following subsections, I give a variety of examples of sources of interest and briefly discuss what future millimeter observations stand to reveal about each one.

### **Long Duration Gamma Ray Bursts**

To begin with extragalactic sources, long duration gamma-ray bursts (LGRBs) are among the most energetic phenomena in our universe, observable out to moderate redshifts. Theorized to originate from the collapse of massive stars (Woosley and Bloom, 2006), these relativistic jetted explosions produce powerful millimeter-bright shocks. The explosion produces two types of shocks: a forward shock expanding outwards into the surrounding material and a reverse shock propagating back through the expanding ejecta. As theorized in (Sari and Piran, 1999), the reverse shocks of LGRBs contain information about the composition and speed of the ejecta material. As first observed by Laskar et al., 2013, bright millimeter synchrotron emission is produced by the reverse shock in the few days following the LGRB event. Reverse shock millimeter emission has been observed in a number of LGRBs since then and continues to be an active area of interest for broadening our understanding of extreme stellar death.

### **Interacting Supernovae**

While GRBs represent millimeter emission originating from reverse shocks, supernovae exploding in dense environments offer us the possibility of observing millimeter forward shock emission. As massive stars undergo mass-loss near the ends of their lives, they enrich their circumstellar media (CSM). Following the supernova explosion, a forward shock and reverse shock are produced—the mildly relativistic forward shock interacts with the dense CSM (Chugai, 1990), generating radio emission as described in Chevalier, 1998. Millimeter emission has only been detected from a handful of supernovae thus far (e.g., Cao et al., 2013; Horesh et al., 2013), but as discussed in greater detail in this thesis, the prevalence of late-time radio emission from interacting supernovae (see review in Chandra, 2018) suggest that more millimeter-bright events should exist (Yadlapalli, Ravi, and Ho, 2022).

Their detections would probe late-stage mass-loss from massive stars and better reveal early-time properties of supernova shocks.

### **Fast Blue Optical Transients**

An emerging class of extragalactic transients also thought to arise from stellar death (or related activity) are fast blue optical transients (FBOTS; Drout et al., 2014). In recent years, these transients have been discovered to exhibit luminous radio (Ho et al., 2020; Yao et al., 2022) and millimeter (Ho et al., 2019a; Ho et al., 2021) emission, with millimeter bands showing particularly rapid evolution. Synchrotron emission is known to be the origin, but given the marked difference of their light curves from those of typical interacting supernovae, further investigation is required to discern CSM shock interaction from other mechanisms, such as engine-driven explosions (Margutti et al., 2019).

### **Tidal Disruption Events**

Tidal disruption events (TDEs) are a class of transients arising from stars very near the centers of galaxies passing through the tidal radius of supermassive black holes (SMBH). These stars quickly overfill their Roche lobes and deposit material onto the black holes (Hills, 1975). The first evidence of radio-loud jets from TDEs was discovered through the event Swift J1644+57 (Zauderer et al., 2011). Since then, only a handful more have been discovered and millimeter emission has been detected from only a subset of those, including (but not limited to) Swift J1644+57, IGR J12580+0134 (Yuan et al., 2016), and AT2022cmc (Andreoni et al., 2022). As highlighted in Yuan et al., 2016, millimeter and sub-millimeter observations provide the best opportunity for early detection of jet activity and outflow interaction, which in turn enhances our ability to understand the environments around and kinematics of jetted TDEs.

### **Supermassive Black Holes**

Supermassive black holes may show variability in brightness and in structure on timescales as fast as the light-crossing times of their event horizons or as slow as months and years. Millimeter synchrotron emission from SMBHs originates from the hot plasma orbiting around the central regions or in some cases, also from relativistically moving jets. For example, in the case of the SMBH in nearby galaxy M87, observations with the Event Horizon Telescope have potentially revealed variability on dynamical timescales (Event Horizon Telescope Collaboration et al.,

2019d; Satapathy et al., 2022). Much faster variations have been observed for lower mass SMBH Sagittarius A\* at the center of the Milky Way (Event Horizon Telescope Collaboration et al., 2022). Lower frequency observations over many epochs with the Very Long Baseline Array have revealed evolution of the components of the M87 jet on timescales of weeks to months (Walker et al., 2018). The physics of the accretion flows (e.g., Rees et al., 1982; Narayan and Yi, 1994) as well as the jet dynamics of SMBHs (e.g., Blandford and Znajek, 1977; Blandford and Payne, 1982) remains an open question to astronomers and frequent millimeter monitoring on many angular scales for these sources has the power to elucidate these processes.

### **Black Hole X-Ray Binaries**

In comparison to SMBHs, the behaviors of galactic stellar mass black holes can be studied on much shorter timescales using observations of black hole x-ray binaries (BHXRBs). These are systems with low mass black holes accreting from companion high mass stars, as first discovered in system Cygnus X-1 (Tananbaum et al., 1972). Cyg X-1 laid the groundwork for understanding state transitions in the accretion disks of black holes (Ichimaru, 1977) and how the accretion correlated to radio jet activity (Falcke and Biermann, 1995; Gallo, Fender, and Pooley, 2003). Systems in active accretion states exhibit bright radio flares. High resolution radio observations have shown relativistically moving, synchrotron emitting ejecta during these states (e.g., Mirabel and Rodríguez, 1994; Miller-Jones et al., 2019) as well the presence of compact, steady jets (**Yadlapalli2021**; e.g., Dhawan, Mirabel, and Rodriguez, 2000; Russell et al., 2015). Until recently, however, very few millimeter measurements had been made of BHXRBs. New millimeter observations of temporally resolved flares on the timescales of minutes have both demonstrated the ability of millimeter bands over lower frequency radio to best study individual flares and enabled studies comparing radio and millimeter light curves to reveal jet properties (Tetarenko et al., 2017; Tetarenko et al., 2021). Upcoming programs on millimeter telescopes to study BHXRBs are likely to make significant strides in understanding stellar mass black hole dynamics in the coming years.

### **Stellar Flares**

Perhaps the newest class of millimeter transients to have piqued the interest of astronomers is stellar flares. Stellar flares are the result of magnetic field lines reorienting on the stellar surface and releasing bursts of energy. Electrons are then accelerated along those field lines, producing the radio and millimeter emission

seen from the flares. The properties of these flares such as the energy distributions of the particles, the strengths of the magnetic field lines along the flare, as well as particle trapping mechanisms all remain open questions. Depending on the electron energies, the primary mechanism of emission is either gyrosynchrotron (described for example in Dulk, 1985; White and Kundu, 1992) or synchrotron (theorized more recently upon polarized observations such as Phillips et al., 1996). While lower frequency radio emission had been observed from stars in the past, recent detections of millimeter flares with ALMA (MacGregor, Osten, and Hughes, 2020a; MacGregor et al., 2021; Burton, MacGregor, and Osten, 2022) as well as blind detections from wide-field surveys (Naess et al., 2020; Guns et al., 2021) have revealed that the rates of these events are much higher than was previously realized. Future studies will likely compile a population of such millimeter flares and coordinated simultaneous observations will aim to provide multi-wavelength perspectives on the question of emission mechanisms.

### **The Need for More Observations**

The classes of sources I mention above do not represent an exhaustive list of all sources of millimeter emission, but a common theme between them is a paucity of observations compared to other wavelengths. To best understand the millimeter sky, we need to push beyond small numbers and build up populations of these sources to uncover their occurrence rates and luminosity functions. Perhaps the reason this has not yet been accomplished, however, can be attributed to the challenges of millimeter instrumentation limiting the number of observing resources available to us. This stands to change with advancements in high frequency electronics and plans for several new millimeter facilities in the coming years.

### **1.2 Challenges Facing Millimeter Telescopes**

In 1952, Martin Ryle published resolved measurements of astronomical sources using the first ever implementation of a phase switching interferometer (Ryle, 1952). He stated then that this technology could be leveraged to measure the angular sizes and precise positions of faint radio sources, even in the presence of high receiver noise and bright, diffuse background emission. This discovery revolutionized radio astronomy and laid the groundwork for modern-day radio interferometry.

Since those early measurements, interferometry has pushed to higher and higher frequencies in hopes of achieving ever-better angular resolution,  $\theta$ , which scales with wavelength,  $\lambda$ , and baseline length,  $b$ , as follows

$$\theta \sim \frac{\lambda}{b} \quad (1.1)$$

However, compared to lower frequencies, advancements in millimeter interferometry were often limited by technologies available for constructing sensitive receiving systems. Development of electronic components capable of performing at high frequencies were pushed through needs for radar and communication purposes; these were then utilized and improved upon by astronomers. Improvements on low-noise millimeter wave mixers, especially the invention of the superconducting-insulating-superconducting (SIS) mixer (Tucker, 1979; Dolan, Phillips, and Woody, 1979; Richards et al., 1979), were key to bringing sensitive superheterodyne receiving systems to reality.

Another challenge for millimeter astronomy is the need for much more precisely manufactured antennas. According to the Ruze formula (Ruze, 1966), the aperture efficiency of an antenna exponentially declines with increasing root-mean-square (rms) deviations from a perfect surfaces. Reproduced below,  $A_0$  is the true surface area of the antenna,  $\lambda$  is the observing wavelength,  $\sigma$  represents the rms size of the surface imperfections, and  $A$  represents the effective aperture. This relation mandates that a sufficiently sensitive millimeter antenna must have a surface accuracy better than a few percent of a millimeter, a requirement that strains the effort to build very large apertures that observe at these wavelengths.

$$A = A_0 e^{-(4\pi\sigma/\lambda^2)} \quad (1.2)$$

A third major challenge facing millimeter telescopes is finding a site free of poor atmospheric conditions that degrade millimeter observations. Though millimeter observations can be conducting during the daytime, they must be conducted in conditions free of cloud cover, precipitation, and high humidity levels. Atmospheric absorption affects millimeter wavelengths much more than centimeter wavelengths, as shown in Figure 1.1. Atmospheric opacity then increases as the secant of zenith angle.

In considerations of interferometry, phase fluctuations along a baseline due to variations in the atmosphere increase exponentially with increasing baseline length and



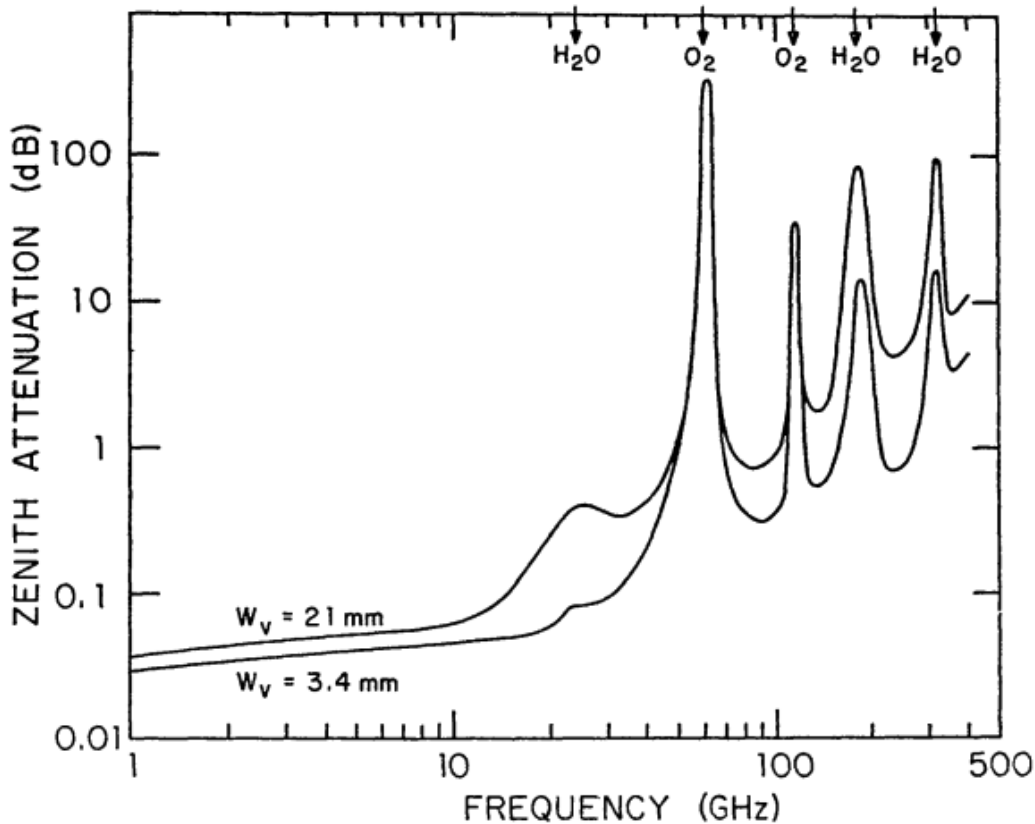


Figure 1.1: Atmospheric opacity at zenith as a function of observing wavelength.  $W_V$  represents total precipitable water vapor in units of millimeters. Reproduced from Findlay, 1971.

linearly with decreasing observing wavelength. This effect is lessened at higher altitude sites with thinner atmospheres. This is why highly sensitive, long baseline telescopes, such as the Atacama Large Millimeter Array (ALMA; Wootten and Thompson, 2009) and the Submillimeter Array (SMA; Ho, Moran, and Lo, 2004), are situated at high-altitude desert locations. Given these considerations, few ideal sites exist in the world (along with sufficient infrastructure) to conduct millimeter astronomy.

### 1.3 Millimeter Interferometry at the Owens Valley: A Historical Perspective

Millimeter astronomy at the Owens Valley Radio Observatory (OVRO) began in the 1970's, when Caltech professor Robert Leighton led the development of a set of three antennas to be used at OVRO for millimeter and submillimeter astronomy. These dishes were designed to have better than  $10 \mu\text{m}$  surface accuracy, pointing of better than 10 arcseconds, and housed SIS mixers with both 100 and 230 GHz



Figure 1.2: Two Leighton antennas that comprise the single baseline of SPRITE.

observing modes. Known as the Caltech Millimeter Array (MMA; Padin et al., 1991), this instrument represented one of the world's earliest forays into millimeter interferometry. First commissioning observations were taken in the late 1980s at 2.7 mm (Keene and Masson, 1986) and the early 1990s at 1.4 mm (Mundy et al., 1990). In the years following those initial observations, the array expanded from three to six antennas and produced some of the earliest examples of millimeter interferometric images.

Due to the resounding success of the MMA, a more ambitious millimeter project called the Combined Array for Research in Millimeter-wave Astronomy (CARMA; Woody et al., 2004) interferometer was proposed. CARMA would consist of all six Leighton antennas plus nine dishes from the Berkeley-Illinois-Maryland Association (BIMA) array as well as eight dishes from the Sunyaev-Zel'dovich Array (SZA). The antennas were all transported up to Cedar Flat, a high site in the White Mountains near OVRO. Equipped with a higher site and longer baselines, CARMA conducted cutting edge millimeter observations during the years between 2005 and 2015. Aspirations to achieve more in millimeter astronomy, however, led to the creation of

ALMA. With many more antennas and a superior site, ALMA could far outperform CARMA and thus, in 2015 operations ended at CARMA due to lack of funding. All of the antennas were brought back down to OVRO - the six Leighton antennas were restored to their original homes on the tracks of the 'T,' awaiting new projects.

Since then, one of the six Leighton antennas was revived for the Carbon Monoxide (CO) Line Intensity Mapping Pathfinder experiment (COMAP; Lamb et al., 2022). Recently, two more of the six antennas are being utilized for the Stokes Polarization Radio Interferometer for Time-domain Experiments (SPRITE, as shown in Figure 1.2). As will be discussed more in this thesis, SPRITE is a single baseline 90 GHz interferometer that aims to bring new resources to the field of transient millimeter astronomy and will carry on the legacy of millimeter observations at OVRO.

#### **1.4 Very Long Baseline Interferometry at Millimeter Wavelengths**

While SPRITE represents science with short, single baseline interferometry, there exists on the other end of the spectrum imaging at very high angular resolutions using very long baseline interferometry (VLBI). VLBI poses a number of additional challenges above connected-element interferometry. For traditional interferometers, the measurements and correlations are all done along the same signal path, and the correlated signal is the final product written to disk. For VLBI, however, as measurements are being taken at independent stations, data from each telescope is first stored and then correlated after the observation is complete. In this case, as reference signals cannot be shared across antennas, additional delay and delay rates differences will be present in VLBI signals that must be calibrated out before correlating the data.

Phase coherence is a major challenge for VLBI experiments as well, as each station is observing through uncorrelated atmospheric conditions and at high fringe rates. To combat this, some experiments may choose to emulate connected-element interferometers and use phase referencing, a technique that utilizes observations of a known point source to calibrate the visibility phases; however, as VLBI pushes to ever better resolutions, the number of available unresolved calibrator sources drops significantly. The technique of extracting phase and amplitude information from noisy data using closure quantities, as derived in Jennison, 1958, has been essential in making precise measurements and generating images with VLBI.

The first GHz VLBI measurements were taken at Jodrell Bank in 1967 to place constraints on the angular sizes of quasars and radio galaxies (Palmer et al., 1967). These measurements were done using a single 126 km baseline, with radio communication towers transmitting the data for correlation, and the analysis was done simply by observing variations of the fringe amplitude. Since then, arrays dedicated to conducting VLBI observations, such as the Very Long Baseline Array (VLBA; Napier et al., 1994), on much longer baselines have come online, paving the way for what is possible in high resolution imaging.

In a 1973 review on techniques in millimeter astronomy, the authors stated that "the use of very-long-baseline interferometric techniques at millimeter wavelengths would provide, in principle, a resolution unobtainable at longer wavelengths, since the maximum antenna spacing at any wavelength is limited only by the size of the Earth" (Penzias and Burrus, 1973). At the time, they likely did not realize how this concept would come to fruition. At the extremes of high-resolution imaging, the Event Horizon Telescope (EHT; Event Horizon Telescope Collaboration et al., 2019a) utilizes millimeter observing facilities all over the globe to image black holes at event horizon scales. The early stages of this project can actually be traced back to contributions from OVRO. Early VLBI measurements confirming small scale structure of Sagittarius A\* were taken using the MMA (Doeleman et al., 2001), while the first detection of event horizon scale structure contained observations with CARMA (Doeleman et al., 2008). Since then, as will be discussed further in this thesis, the EHT has pushed the bounds of both VLBI observations and image reconstruction techniques to reveal the first resolved images of the event horizon structure around black holes.

## 1.5 Thesis Outline

This thesis is outlined as follows. Chapter 2 discusses instrument details, commissioning procedures, and future directions of the Stokes Polarization Radio Interferometer for Time-domain Experiments (SPRITE). Chapter 3 discusses theoretical predictions for millimeter light curves for interacting supernovae, justifies the need for targeted millimeter observations of these events, and predicts feasibility of detections in next generation wide-field millimeter surveys. Chapter 4 discusses the discovery of a resolved compact radio source in BHXRB system AT2019wey; though this chapter focuses on lower frequency observations, it exemplifies opportunities for further unveiling source properties with millimeter observations. Chapter 5 describes the procedures for imaging the SMBH in M87 using the 2018 epoch of

observations from the EHT and touches upon the fruitfulness of multiple years of observations. Finally, in Chapter 6, I summarize and look ahead to future directions of millimeter astronomy.

*Chapter 2***COMMISSIONING THE STOKES POLARIZATION RADIO  
INTERFEROMETER FOR TIME-DOMAIN EXPERIMENTS  
(SPRITE)**

Nitika Yadlapalli and the SPRITE Team

**Abstract**

Though the time-domain millimeter sky is yet to be well characterized, the scarcity of millimeter observing resources in the world at present hampers progress towards it. In efforts to bolster the exploration of millimeter transients, we present the Stokes Polarization Radio Interferometer for Time-Domain Experiments (SPRITE). Located at the Owens Valley Radio Observatory, SPRITE is a two-element short-baseline 90 GHz interferometer uniquely focused on monitoring bright, nearby millimeter transients. We leverage two existing 10.4 m antennas and their SIS receiver systems to begin, but make significant upgrades to the backend system during the commissioning process. With the ability to achieve a few mJy rms noise, we plan to monitor known variable sources along with new nearby transients detected from optical surveys at high cadence, with the goal of producing well-sampled light curves. Interpreting these data in conjunction with multi-wavelength observations stands to provide insight into the physical properties of the sources that produce transient millimeter emission. We present commissioning and early-science observations that demonstrate the performance of the instrument, including observations of the flaring BL Lac object S2 0109+22 and a periastron passage of the binary T Tauri system DQ Tau.

**2.1 Introduction**

The recently discovered prevalence and frequency of millimeter transients has generated a need for observing resources dedicated to monitoring and follow-up of interesting sources. For example, transient search pipelines applied to observations from the more sensitive SPT-3G (Guns et al., 2021) and the Atacama Cosmology Telescope (ACT; Naess et al., 2021) yielded a sample of 18 events on timescales of days to weeks, surprisingly dominated by Galactic stars. These discoveries only

scratch the surface of what can be accomplished with wide-field millimeter surveys, described further in Eftekhari et al., 2022.

In addition to wide-field surveys, it is also important to conduct targeted studies that aim to constrain the rates and luminosities of millimeter transients from different classes of object. Common origins of extragalactic millimeter transient emission include synchrotron sources such as reverse shock emission from gamma ray bursts (GRBs; De Ugarte Postigo et al., 2012; Laskar et al., 2013), jet emission from some tidal disruption events (TDEs; Zauderer et al., 2011; Yuan et al., 2016; Andreoni et al., 2022), fast blue optical transients (FBOTs; Ho et al., 2019b; Ho et al., 2022), and interacting supernovae (Horesh et al., 2013; Cao et al., 2013). Galactic accreting compact-object sources, such as black hole X-ray binaries (Tetarenko et al., 2017), may also produce millimeter synchrotron emission. Recent detections of millimeter flares from nearby active stars have revealed yet another frequent source of transient millimeter emission needing deeper study (MacGregor et al., 2018; MacGregor, Osten, and Hughes, 2020b; Burton, MacGregor, and Osten, 2022). A few detections of giant millimeter flares from young stellar objects (e.g., Bower et al., 2003; Vargas-González et al., 2023) also await further systematic characterization. In general, transient millimeter emission probes the physical extremes of the sources: the earliest stages of the evolution of jets and outflows, environmental conditions closest to the central engines, and the limits of magnetization and particle acceleration.

Even as millimeter observing resources become more abundant, through both wide-field surveys and highly sensitive facilities such the Atacama Large Millimeter Array (ALMA) or the Submillimeter Array (SMA), there still remains a need for observing resources dedicated to conducting studies of transients. To fill this gap, we present the Stokes Polarization Radio Interferometer for Time-domain Experiments (SPRITE), located at the Owens Valley Radio Observatory (OVRO) that will solely focus on monitoring and following up sources of transient millimeter emission.

## 2.2 Instrument Overview

### Antennas

SPRITE utilizes two Leighton 10.4 m antennas (Leighton, 1977). Built in the late 1970's, these antennas were designed to perform some of the earliest millimeter aperture-synthesis observations. Surface accuracies better than  $50\ \mu\text{m}$  delivered excellent response down to wavelengths as small as 1 mm; SPRITE, however, will primarily utilize the 3 mm observing band. Each antenna was built with a sidecab,

in which the receivers and supporting electronics are contained. Observations of compact sources were used to derive an antenna aperture efficiency of  $\sim 0.5$  (Wright et al., 2009).

Most recently, the Leighton antennas used here were a key component of the Combined Array for Research in Millimeter-wave Astronomy (CARMA; Woody et al., 2004). In 2015, CARMA was decommissioned and the dishes were moved back to OVRO. Five antennas were available to choose from to make up SPRITE—the two we opted for comprised the shortest possible baseline of 24 m. This decision was motivated in part by minimizing atmospheric phase noise. As shown in Carilli and Holdaway, 1997 for tests done on the Very Large Array (VLA), baseline length correlates with the amount of RMS phase noise present in observations. As the effect of atmospheric turbulence scales inversely with wavelength and SPRITE will not make images that require high spatial resolution, the shortest baseline was the most prudent choice.

### **Monitor and Control**

All communications for monitor and control of the Leighton antennas are done using a controller-area-network bus (CANbus) message system originally developed for CARMA. Each antenna sidecab houses its own computer that manages all incoming and outgoing CAN messages. Most monitor points are sampled 0.1 s intervals, but read out in sets of five every 0.5 s. Encoder values, however, are an exception and are read out every 0.1 s. Communication with the CAN modules for SPRITE occurs in a few different ways.

The antennas are driven using a graphical control system developed at OVRO for the Carbon Monoxide (CO) Mapping Project Pathfinder (COMAP; Lamb et al., 2022). This control system communicates with the modules controlling the antenna drives and other basic mechanics of the antenna. It also allows the user to check current azimuths and elevations of all sources in the source catalog, monitor current weather conditions, and run observing schedules. An additional feature of this control system is its storage of monitor data to an archive. Information for specific monitor points can be retrieved for arbitrary durations of time to be used for downstream analysis of antenna behavior, such as for measuring coefficients of the pointing model as will be described in Section 2.2. The receiving system is largely controlled using a LabVIEW program, originally developed for use at CARMA, that interfaces with CAN modules communicating with receiver components. These monitor points



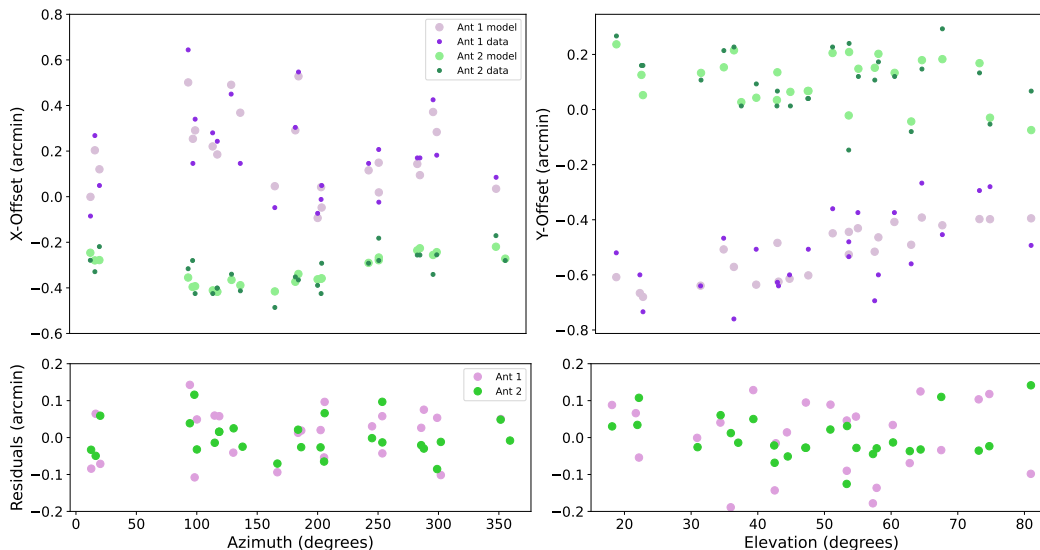


Figure 2.1: Example of data collected on 23 stars for calculation of the optical pointing model coefficients. *Top:* The smaller, darker markers shown are the true locations and offsets of the stars measured with each antenna. The larger, lighter markers show the pointing coefficients that best reproduce the observed offsets. *Bottom:* Residuals for the fit shown in the top panel, showing that there is no directional dependence to the fidelity of the model fitting.

include values such as a measure of the received power, attenuation levels at various stages, the receiver temperature, etc. Usage of this system for tuning and calibrating the receiver is described in Section 2.2.

## Pointing

The Leighton antennas slew in both elevation and azimuth and can be driven directly from the control system. The procedure for determining pointing for the antennas has been well established and consists of three unique measurements: the tilt of the antenna base, mount-dependent pointing coefficients using an optical camera, and aperture-dependent pointing coefficients using radio measurements. These values are all stored within the control system and are used to calculate the corrections applied to the drives that control the telescope's movement.

The first step of measuring the tilt of the antenna base involves slewing the telescope through eight discrete steps of azimuth and measuring the amount of tilt with two orthogonally oriented digital tiltmeters located inside the base. The amount of tilt with respect to azimuth will vary sinusoidally. Tilt values and azimuth values as a function of time are read from the control system archive and the values are mapped

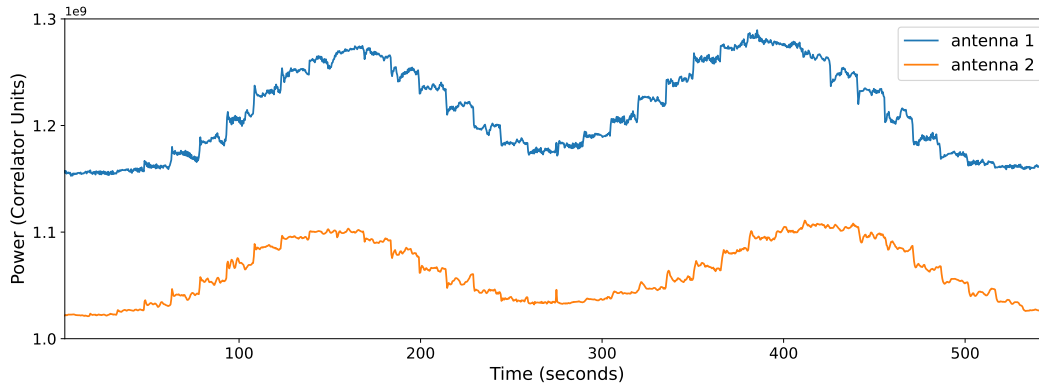


Figure 2.2: Example of data collected on Jupiter for single dish radio pointing measurements. Light curves are shown for both antennas from scans in both the x- and y-directions across the disk of the planet, which are represented by the first and second portion of the light curves, respectively. This scan measured offsets of  $\pm 90$  arcseconds at 10 arcsecond increments.

to each other and fit with a sinusoid. The constant offset term to the sinusoidal fit is known as the tilt-zero value and is the value of interest to the pointing model.

Following this, we need to calculate the coefficients of the seven term azimuth and elevation dependent pointing model. Three of these seven terms relate are dependent upon the antenna mount while the remaining four of the seven are dependent upon the position of the antenna aperture. They map to errors in azimuth,  $AZ$ , and elevation,  $EL$ , as follows, where  $M$  denotes mount coefficients and  $A$  denotes aperture coefficients.

$$\begin{aligned} \Delta AZ = & A_1 + M_1 \cos(EL) + M_3 \sin(EL) \\ & - M_4 \sin(AZ) \sin(EL) - M_5 \cos(AZ) \sin(EL) \end{aligned} \quad (2.1)$$

$$\begin{aligned} \Delta EL = & -M_4 \cos(AZ) + M_5 \sin(AZ) \\ & + A_2 + A_3 \cos(EL) \end{aligned} \quad (2.2)$$

To constrain these coefficients, we utilize an optical camera mounted to part of the truss structure. The camera looks through a machined hole in the antenna and is used to observe stars at a variety of elevations and azimuths. The pointing offsets for each star are determined by the observer with the aid of the camera frame-capture tool within the control system. The offset required to center each star is read

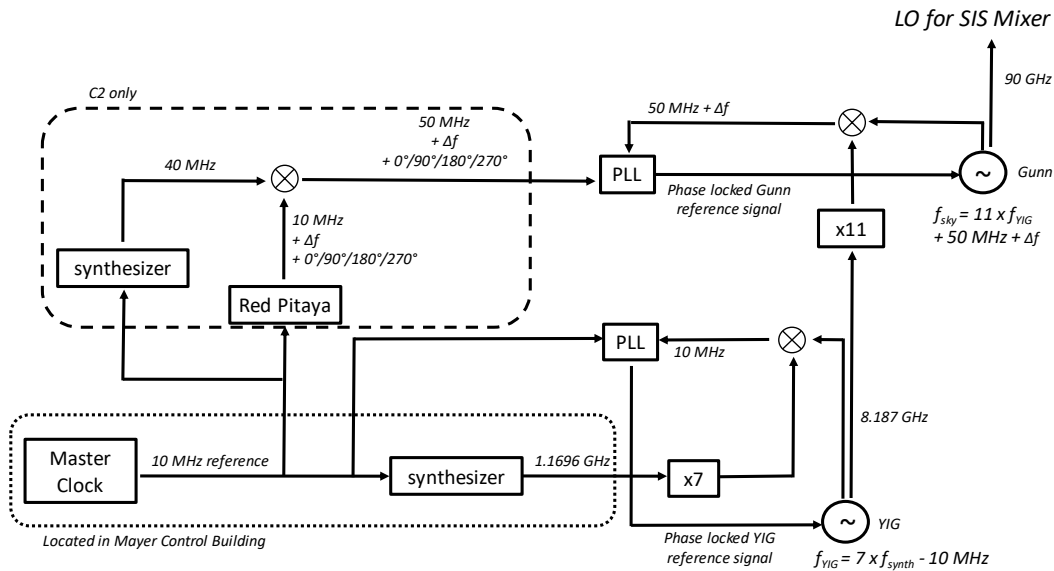


Figure 2.3: Diagram showing how the LO signal for the SIS mixer is generated. The components within the dotted box are located in the basement of the Mayer control building and are one set of components shared between both antennas. Signals leaving the Mayer control building are sent out over optical fiber and modulated back to RF within each of the antennas. The components within the dashed line represent the system in the sidecab of Antenna 2 only. In Antenna 1, the dashed box is replaced by a single synthesizer that generates a 50 MHz signal.

from the control-system archive, and offsets as a function of true location are used to calculate the mount coefficients and optical aperture coefficients using a least squares minimization. A visualization of this is shown in Figure 2.1. A minimum of ten stars is preferred to achieve a reasonable fit; however, the rms error for the fits to each of the coefficients decreases linearly with increasing numbers of stars. Thus, it is greatly preferred to use at least 20 or more.

To determine the radio aperture coefficients however, we must use radio observations. For this, we use the correlator (see Section 2.2 below) to record observations of resolved disk objects (such as Saturn, Jupiter, or the moon) conducted by stepping through different x- and y-offset values. An example light curve from this type of observation is shown in Figure 2.2. The offsets that maximize the observed brightness of the source are used to determine the radio aperture coefficients. Finer adjustments are then made to these coefficients by using a similar procedure with interferometric measurements. These measurements are repeated routinely to account for changes in weather and temperature that alter the relative distances between various components of the telescope.

The procedures described above have resulted in an empirical radio pointing accuracy that is better than  $\pm 10$  arcseconds (peak to peak), as determined through interferometric pointing measurements. Given a Gaussian primary half-power beamwidth at 90 GHz of 81 arcseconds, this corresponds to a maximum intensity loss of  $< 4\%$ . Finer correction can be achieved with regular interferometric-pointing scans.

### **Receiving System**

SPRITE mostly utilizes the original millimeter receiving system designed for use in CARMA. The receivers are located in the sidecabs of the antennas and are positioned at a Nasmyth focus. They can support both 3 mm and 1 mm observations and employ superconducting-insulating-superconducting (SIS) mixers. To maintain high sensitivity at our observing wavelengths, the receivers are cryogenically cooled with a radiation shield providing cooling to around 70 K and the second stage cooling down to around 4.5 K. While much of the local oscillator (LO) signal generation procedure remains the same, major modifications were made to the lobe rotation and phase switching system.

### **LO Signal Generation**

The multiple steps required to generate the LO signal are shown in Figure A.4. In short, the LO signal needs to be around 90 GHz and phase locked to a reference signal that contains necessary phase information regarding quadrature phase switching and lobe rotation corrections. The signal path for generating the LO signal requires two separate oscillators: a yttrium-iron-garnet (YIG) oscillator that generates a first stage phase-locked signal around 8 GHz and a Gunn oscillator that generates the final 90 GHz signal. The reference signal for the Gunn oscillator must be 50 MHz. All sources of signal generation are referenced to a common 10 MHz source derived from OVRO's master clock source.

In order to accurately control the phase of the output 90 GHz signal from the Gunn oscillator, a phase-locked loop (PLL) must be utilized along with the phase controlled 50 MHz reference signal. The comparison 50 MHz signal for the PLL is generated by mixing the output of the Gunn oscillator with a harmonic of a phase-locked signal generated by the YIG oscillator. The master clock signal and the synthesizer feeding the PLL (referred to as the LO reference signal) of the YIG oscillator are both located in the basement of OVRO's Meyer Control Building and the synthesizer signal is sent out to the antennas, where the oscillators are located, over optical fiber.

All of this hardware was pre-existing and required no modifications for SPRITE. The locked status of the oscillators as well as the power of the LO reference signal are controlled through the LabVIEW program.

### Lobe Rotation

Referring to equation 6.11 of Thompson, Moran, and Swenson, 2017, the phase difference across the upper sideband of a single baseline, comprising of antennas  $m$  and  $n$ , just following a single stage of downconversion is given as follows (assuming both visibility phase and gain phase are zero).

$$\phi_{mn} = 2\pi\nu_{LO}\tau_g + (\theta_m - \theta_n) \quad (2.3)$$

Here,  $\nu_{LO}$  is the LO frequency and  $\tau_g$  is the geometric delay between the two antennas, while  $\theta_m$  and  $\theta_n$  refer to the phase of the LOs in antennas  $m$  and  $n$ . To stop the fringes in the final visibility, we need to adjust the phase difference between the LOs at the same rate that the geometric delay is changing, as shown.

$$2\pi\nu_{LO}\frac{d\tau_g}{dt} + \frac{d}{dt}(\theta_m - \theta_n) = 0$$

$$2\pi\nu_{LO}\frac{b\sin\theta}{c}\frac{d\theta}{dt} = \frac{d}{dt}(\theta_m - \theta_n) \quad (2.4)$$

In Eq. 2.4,  $b$  is the baseline length and  $\theta$  is the angle between the baseline vector and the source position vector. For observations at 90 GHz with a 24 m baseline, the maximum speed of the fringes (known as the natural fringe frequency) will be  $\sim 0.5$  Hz. We control the phase difference between the LOs of the antennas by keeping the 50 MHz fixed in one antenna and modulating the 50 MHz of the other as shown in Figure A.4. To generate the 50 MHz reference signal for the Gunn's PLL, we mix a phase adjusted 10 MHz signal with a static 40 MHz signal. The phase adjustments to the 10 MHz signal include adjustments for lobe rotation and quadrature phase switching, required for sideband separation of the correlations.

Though a lobe rotation and phase switching system for the Leighton antennas already existed, it is optimized for use in a multi-baseline array and is more complicated than required for SPRITE. We implement a simpler and more modern solution using a small, inexpensive device produced by Red Pitaya (STEMLab 125-10; hereafter

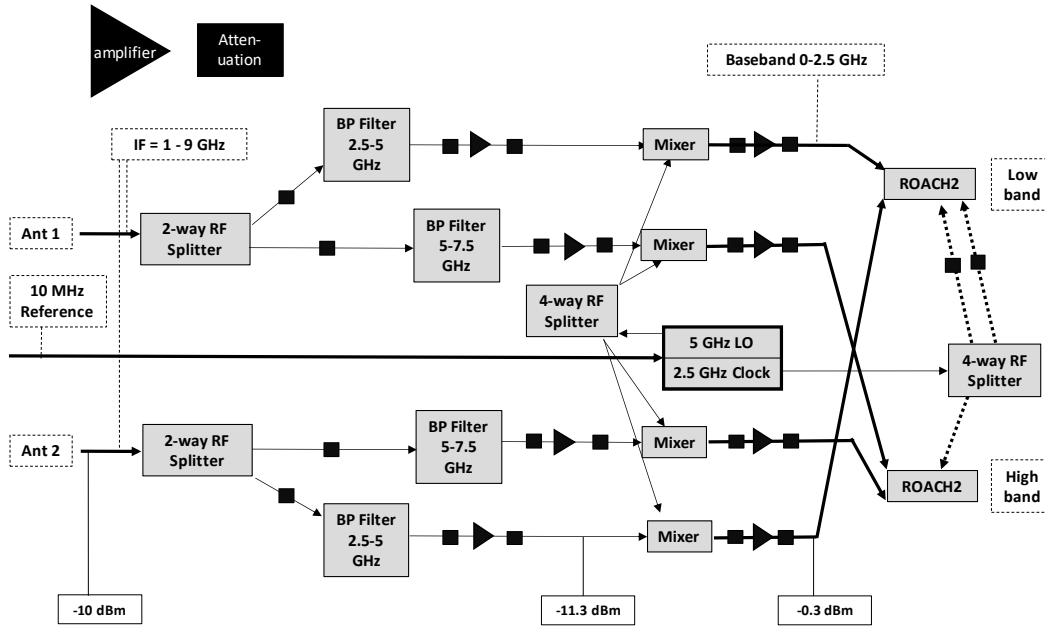


Figure 2.4: Diagram of the SPRITE 2nd stage downconversion system showing how IF signals from both antennas are split into high and low band components to be fed to their respective ROACH2 boards for correlation. The bold arrows represent input signals to the downconverter as well as output signals to the ROACH2. The thick dotted lines indicate clocking signals. One of our ROACH2 boards contains two inputs for two clock signals whereas the other ROACH2 board contains only one clock signal input and splits the signal internally.

“Red Pitaya”). It features a 32-bit field programmable gate array (FPGA) clocked at 125 MHz as well as two 10-bit analog to digital converters (ADC) and digital to analog converters (DAC), sufficient for a simple operation such as adjusting the phase of an input signal. The firmware described in this section was written using tools developed by the CASPER collaboration (Hickish et al., 2016). Both the Red Pitaya as well as the synthesizer generating the 40 MHz signal are located in an electronics rack within the antenna sidecab.

To start, we write the phase shifted signal as a linear combination of the cosine and sine components of the original signal, as below, where  $\phi$  is the phase shift required to keep up with the fringe rate of the source and  $\theta_{\text{switch}}$  is the phase switching term.

$$\cos(x - \phi + \theta_{\text{switch}}) = A\cos(x) + B\sin(x) \quad (2.5)$$

Let us assume that input 10 MHz signal on the ADC represents the cosine component,  $\cos(x)$ . To derive the sine component, we delay the incoming signal by one

clock cycle of FPGA, which translates to a  $\phi' = 0.5$  rad shift of 10 MHz signal. Then, we may program the firmware to use a linear combination of the original and delayed signal to retrieve the sine component.

$$\begin{aligned}\sin(x) &= \frac{-\cos(x + \phi') + \cos(x)\cos(\phi')}{\sin(\phi')} \\ &= -2.086\cos(x + \phi') + 1.830\cos(x)\end{aligned}\quad (2.6)$$

The coefficients  $A$  and  $B$  are defined as

$$A = \cos(\phi + \theta_{\text{switch}}) \quad (2.7)$$

$$B = \sin(\phi + \theta_{\text{switch}}) \quad (2.8)$$

where the value of  $\theta_{\text{switch}}$  will cycle between  $0^\circ/90^\circ/180^\circ/270^\circ$  at each data readout cycle. We define  $d\phi/dt$  through a software register and the firmware will increment  $\phi$  at each clock cycle and calculate the new values of  $A$  and  $B$  accordingly. Given the 32-bit resolution of values in the Red Pitaya's FPGA, we are limited to correcting the fringe rate at increments of 0.06 Hz. A diagram of the firmware implementation is shown in Figure 2.5.

### First Stage of Downconversion

The original CARMA intermediate frequency (IF) supports 8 GHz of bandwidth between 1-9 GHz. As the SIS mixer is not sideband separating, both the upper and lower sideband are mixed into the IF. The receiving system can be tuned to a specific frequency based on the signal generated from the Gunn along with the bias voltage applied to the SIS mixer. This bias voltage defines a point where the relationship between voltage and current across the superconducting junctions sharply steepens. This occurs when voltage difference across the two superconducting layers becomes high enough to cause the energies of the band gaps to be completely offset from each other. For more information, see review by Phillips and Woody, 1982. The tuning of the receiver is done autonomously by the LabVIEW program.

For low-loss transfer of the signal, the IF is modulated into an optical signal in the sidecab and sent out over optical fiber to the Meyer control building basement, where it is then demodulated back to radio frequency (RF). Upon reaching the Meyer building, the IF signal is fed to the second stage downconversion module.





## Second Stage of Downconversion

Though 8 GHz of IF bandwidth is available to us, the current correlator is limited to sampling a maximum of 5 GHz of bandwidth (4 GHz of bandwidth in practise; see Section 2.2). Given this, the downconversion system designed for SPRITE selects the central 5 GHz of the IF, 2.5-7.5 GHz, to convert to baseband, as shown in Figure 2.4. As will be discussed further in Section 2.2, our correlator handles the upper and lower halves of the selected IF frequencies frequency.

The input from each antenna is first split and fed into custom bandpass filters, one selecting 2.5-5 GHz, purchased from Reactel, and the other selecting 5-7.5 GHz, purchased from K&L Microwave. Using a Mini-Circuits ZX05-83-S+ mixer, these signals are both mixed with a 5 GHz LO signal generated using a Valon 5009 frequency synthesizer, referenced to a 10 MHz from the master clock. Baseband signals from the 2.5-5 GHz signal path of each antenna are directed towards two inputs of one half of the correlator while the signals from the 5-7.5 GHz path are directed towards the other half. Attenuators are placed throughout the system to mitigate reflection from ports of successive components and amplifiers are added to ensure the instrument signal entering the ROACH2 boards is close to 0 dBm.

## Correlator

The SPRITE correlator employs two ROACH2 boards (Parsons et al., 2008), one for each half of the utilized IF bandwidth, for sampling and cross-correlating incoming signals from each antenna. Each ROACH2 contains two interleaved 5 Gbps ADCs, and the clock signals for the ADCs are generated using a Valon 5009 synthesizer. For our FPGA firmware, we use the FX digital correlator design implemented in the Arcminute MicroKelvin Imager (Hickish et al., 2018). At present, a design that processes 2 GHz of bandwidth is implemented and commissioned, which outputs complex auto- and cross-spectra with 2048 channels.

We use Python code to initialize the ROACH2 boards and handle data collection from them. In the initialization script, we reset the software registers, calibrate the ADCS, and set up an integration time. We currently integrate at intervals of 0.4096 seconds, the fastest allowed time by the amount of overhead required to read from the board. The integration is sufficiently fast given that the maximum amount of residual fringe left from the lobe rotator is 0.06 Hz, requiring a Nyquist sampling period of only 8 seconds or better. We then synchronize the two ROACH2 boards using a 1 pulse per second (PPS) signal. By resetting the control registers on each

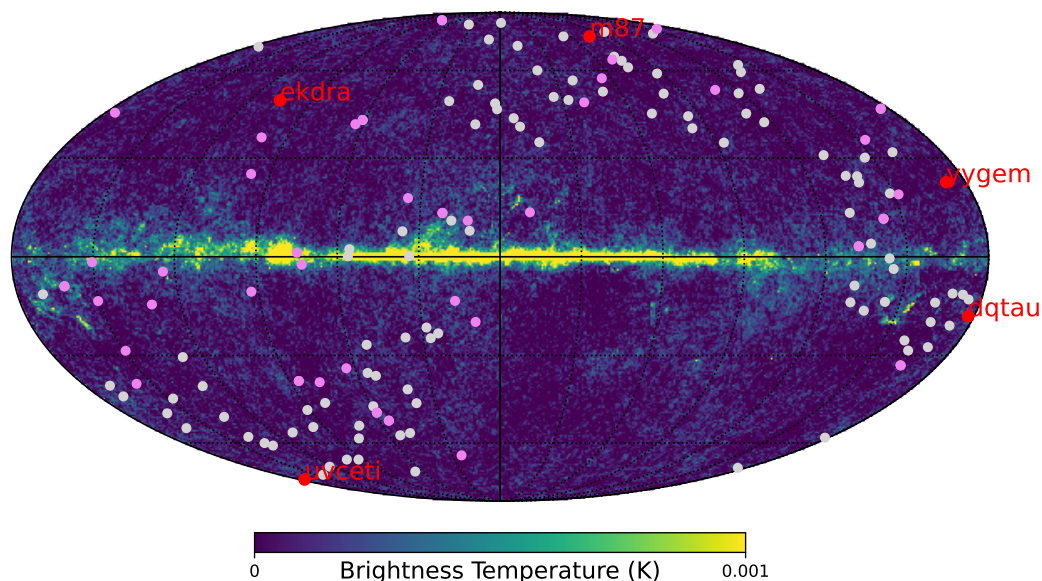


Figure 2.6: Locations of all sources allowed for use as gain calibrators for SPRITE science observations overlaid on a Mollweide projection of a 100 GHz all-sky map (with the CMB subtracted) created with observations from the *Planck* High Frequency Instrument (Planck Collaboration et al., 2020). The gray points represent sources taken from the ALMA calibrator list while blue points represent sources used as calibrators for CARMA. The red points represent a few science targets of interest located at a variety of coordinates to demonstrate the broad availability of calibrator sources.

board to the same pulse, we guarantee that the data is being collected at the same time on each board. This is required for accurately capturing data in sync with the phase switching.

The data collection script handles writing observation information and the output correlations to an output hdf5 data file. At the beginning of each observation, information regarding the name and coordinates of the source are written to the output file. Based on the coordinates of the source, the required lobe rotation rate is calculated and subsequently written to both the hdf5 file and the relevant Red Pitaya software register. When the observation begins, a counter in the ROACH2 firmware increments at the end of each integration length, and the Python code then writes out the complex correlations and timestamps are written out for each integration. At each integration cycle, the phase switching software register is switched to the next phase in the cycle. Data is captured until the elapsed time from the beginning of the observation reaches the specified observation length.

### 2.3 Observing Strategy

Observing schedules for SPRITE are constructed in blocks of 24 hour sequences and observed sources fall into one of four categories: flux calibration, bandpass calibration, gain calibration, and science. For all observations, we take measurements of the system temperature,  $T_{\text{sys}}$ , every five minutes by moving an ambient temperature calibrator load in front of the receiver. A Python script running in parallel to the correlator code communicates with the CAN module to control the movement of the load.

We use two observations of Uranus per sequence to serve as our flux calibration measurements. We calculate the brightness temperature of Uranus at 90 GHz using the frequency dependent model presented in Hasselfield et al., 2013 and the updated model coefficients presented in Louis et al., 2014. From there, we calculate the flux of Uranus at a given observation time using the radius measurements presented in Archinal et al., 2011 and the planet ephemeris calculations built into the `astropy` software package. For bandpass calibration, we use one scan per sequence of either 3C84 or 3C273.

For a specified science target, one minute of gain calibration scans are taken in between 10 minute intervals of science target scans. The set of gain calibrator sources is a combination of ALMA monitored calibrator sources with flux densities greater than 0.5 Jy and the list of bright calibrator sources used at CARMA. The sources and their locations are shown in Figure 2.6. For each science target, we assign the nearest source from this set to serve as the calibrator and allow a generous 90 seconds of slewing time between science and gain calibrator sources.

As the Leighton antennas only have 360 degrees of range to slew, we refrain from observing sources during times when their nearest calibrator source is on the opposite side of the  $0^\circ$  azimuth line. Additionally, though the minimum elevation the Leighton antennas can observe is  $15^\circ$ , we refrain from observing sources lower than  $30^\circ$  due to high atmospheric brightness at low elevations.

To carry out an observing sequence, a schedule file detailing at what time and for what duration to observe each source is written. This initial schedule need only contain bandpass and flux calibrator scans as well as science targets. A Python-based scheduling package written for SPRITE then automatically tags all observations of Uranus as flux calibration scans and all observations of 3C84 and 3C273 as bandpass calibrators. The nearest gain calibrator is identified for each science target and the scans are automatically added. This full schedule is then passed to the COMAP

control system, which schedules movement of the antenna drives, as well as to a wrapper script for the correlator, which parses the schedule and synchronizes times of data collection.

### Data Processing

All of the post-processing of the visibilities is done using custom Python 3.x routines. The first step in reducing data from a sequence is to perform scan by scan preprocessing. For each scan, we separate the sidebands, remove geometric delay effects, and then remove cable length delay effects.

As our SIS mixer is not sideband separating, we rely on the fact that each set of four visibilities read out from the correlator cycles through phases  $0^\circ$ ,  $90^\circ$ ,  $180^\circ$ , and  $270^\circ$  to separate the sidebands downstream from the receiver. In theory, one only needs one set of  $90^\circ$  switched visibilities to perform sideband separation. Referring to section 6.1.12 of Thompson, Moran, and Swenson, 2017, the complex response of a double sideband system is the sum of the upper sideband (USB) and lower sideband (LSB) responses. Referring to eq. 2.9, which assumes the gain amplitude is unity,  $\psi_u$  is the visibility phase of the USB and  $\psi_l$  is that of the LSB.

$$V_{\theta=0^\circ} = |V|[(\cos\psi_u + \cos\psi_l) + i(\sin\psi_u - \sin\psi_l)] \quad (2.9)$$

Delaying the output of antenna 2 by  $90^\circ$  using the Red Pitaya,  $\psi \rightarrow \psi - \pi/2$ , the output visibility becomes

$$V_{\theta=90^\circ} = |V|[(\sin\psi_u + \sin\psi_l) + i(-\cos\psi_u + \cos\psi_l)] \quad (2.10)$$

In our data processing code, we use the following relations to retrieve sideband separated signals:

$$\begin{aligned} V_{\text{LSB}} &= |V|(\sin\psi_l + i\cos\psi_l) \\ &= \frac{1}{2}[(\text{Re}\{V_{\theta=90^\circ}\} - \text{Im}\{V_{\theta=0^\circ}\}) \\ &\quad + i(\text{Im}\{V_{\theta=90^\circ}\} + \text{Re}\{V_{\theta=0^\circ}\})] \end{aligned} \quad (2.11)$$

$$\begin{aligned} V_{\text{USB}} &= |V|(\sin\psi_u + i\cos\psi_u) \\ &= \frac{1}{2}[(\text{Re}\{V_{\theta=90^\circ}\} + \text{Im}\{V_{\theta=0^\circ}\}) \\ &\quad - i(\text{Im}\{V_{\theta=90^\circ}\} - \text{Re}\{V_{\theta=0^\circ}\})] \end{aligned} \quad (2.12)$$

We can switch  $V_{\theta=0^\circ} \rightarrow V_{\theta=180^\circ}$  and  $V_{\theta=90^\circ} \rightarrow V_{\theta=270^\circ}$  in eqs. 2.11 and 2.12 to retrieve separated sideband responses,  $V'_{\text{LSB}}$  and  $V'_{\text{USB}}$ . The correlated signal component in both  $V$  and  $V'$  are identical; however, effects downstream of the receiving system will not be phase switched. As long as the downstream noise is changing very slowly, using the quantity  $V - V'$  allows us to retrieve sideband separated signals free of unwanted correlated noise and cross-talk.

As each ROACH2 board is handling one half of the IF, we essentially have four bands of interest. We refer to each half of the IF as either high band or low band and refer to the sidebands within those as upper bands and lower bands. The sky frequency ranges they span are as follows:

$$F_{HB,l} = 83 - 85 \text{ GHz}$$

$$F_{LB,l} = 85 - 87 \text{ GHz}$$

$$F_{LB,u} = 93 - 95 \text{ GHz}$$

$$F_{HB,u} = 95 - 97 \text{ GHz}$$

For each of these four bands, we calculate model visibilities using the coordinates of the source and the time stamps recorded from the data collection code. We use CASAtoolkit (CASA Team et al., 2022) to calculate the  $(u, v, w)$  terms at each time, deriving phase variations due to the time-varying geometric delay. We then add a correction to these visibilities to simulate the effect of removing a fringe rate with the Red Pitaya. As the last step, we remove the effect of a fixed cable length delay from the visibilities. This value is calculated using the delay spectrum of a bright calibrator source, and adjusted only on a monthly basis. Fixed delay changes also occur each time the ROACH2 boards are reinitialized, but these are absorbed into the bandpass solution, which stays fixed between scans and sequences. At this point, the visibility phase should be flat across all spectral channels and should be constant with time.

The final step of preprocessing the scans is applying antenna-dependent corrections to the bandpass based on measurements of the system temperature,  $T_{\text{sys}}$ . As mentioned in section 4.2, we take measurements of the system temperature every 5 minutes using the ambient load. Measurements of an ambient temperature load contain effects from atmospheric attenuation, so paired with measurements of the

cold sky yields a  $T_{\text{sys}}$  directly through the Y-factor method (Kutner and Ulich, 1981; Carilli, Carlstrom, and Holdaway, 1999) that is likely accurate to  $\sim 10\%$ . Using archived monitoring measurements of the ambient temperature and assuming  $T_{\text{sky}} = T_{\text{CMB}} = 2.73$  K, we calculate the system temperature referenced to the top of the atmosphere for each channel of each antenna using the following equations, where  $P$  denotes power measured in each state.

$$Y_v = \frac{P_{v,\text{load}}}{P_{v,\text{sky}}} \quad (2.13)$$

$$T_{\text{sys},v} = \frac{T_{\text{load}} - Y_v T_{\text{sky}}}{Y_v - 1} \quad (2.14)$$

We calculate the  $T_{\text{sys}}$  spectrum of the interferometer by combining the temperatures measured in each antenna,  $T_1$  and  $T_2$ :  $T_{\text{sys},v} = \sqrt{T_1 T_2}$ . We then divide the cross-correlation spectra from that scan by a correction factor that takes into account the mean autocorrelation value for each antenna,  $A_1$  and  $A_2$  to remove antenna dependent bandpass variations:  $c = \sqrt{T_1 T_2} / \sqrt{A_1 A_2}$ . We mask sections of data when the ambient temperature load was in the optical path, and also mask sections of the frequency band affected by correlator generated birdies and aliasing. The effective remaining double-sideband bandwidth is 3 GHz. At this point, the effects of different atmospheric columns for different pointings are removed from the data, and the scan is fully preprocessed.

After all scans in a sequence are preprocessed, we move on to calibration of the whole sequence. To derive the bandpass solution for the sequence, we compute the average bandpass across the bandpass calibrator scan. We smooth the bandpass solution for both the real and imaginary component separately using an implementation of a Savitzky–Golay filter within Python’s `scipy.signal` package and then apply it to all scans in the sequence. Flux density calibration values are then derived from scans on Uranus using an average value of the visibility across the scan, after de-trending a constant phase slope to account for any atmospheric or instrumental drifts.

Before applying the flux calibration solution, the complex gain variations within tracks of a single source must be calibrated. For each scan on a gain calibrator, a single value of complex gain is derived. The list of gains derived from the calibrator source are then normalized to unity, and the science scans are then corrected for the measured gain-phase variations and the flux density solution is then applied. At this point, fully calibrated scans may be integrated down to achieve higher sensitivity.

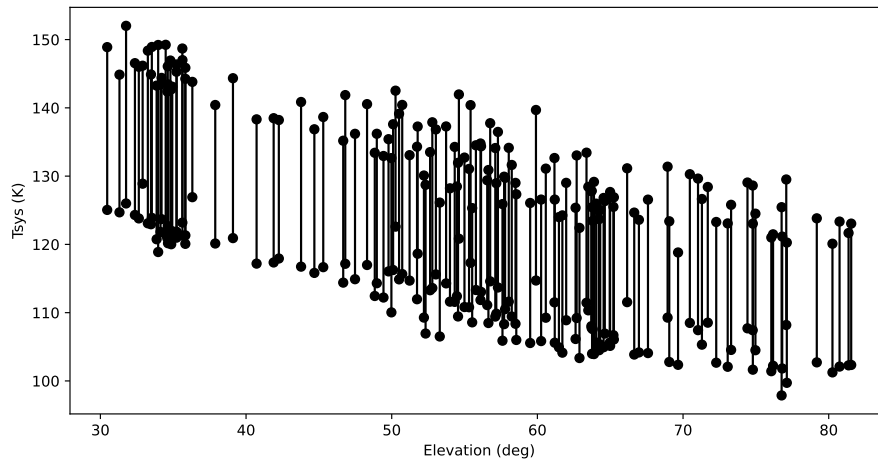


Figure 2.7: Measurements of elevation dependent double-sideband system temperature of the SPRITE baseline in reasonable weather conditions. Each measurement contains the  $T_{\text{sys}}$  of both the high band and low band, shown as dots connected by a line.

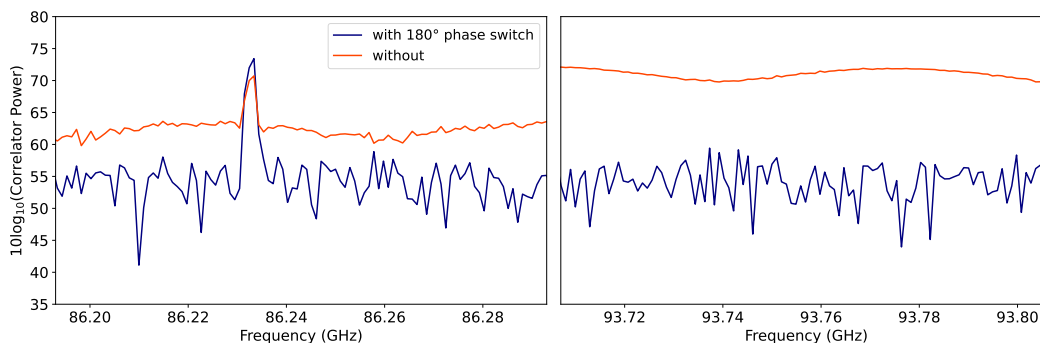


Figure 2.8: Time averaged spectrum of SiO maser emission in R Leo, zoomed in to corresponding frequencies in both the upper and lower sideband, after sideband separation, shown with and without cross-talk mitigation using  $180^\circ$  phase switching.

## 2.4 Commissioning observations

### $T_{\text{sys}}$ Measurement and Sensitivity Prediction

We first present measurements of  $T_{\text{sys}}$  obtained during each scan of a 24-hr sequence, and predict a limiting sensitivity of the current SPRITE deployment. Figure 2.7 shows band-averaged  $T_{\text{sys}}$  measurements from a sequence obtained under reasonable weather conditions as a function of elevation. These double-sideband  $T_{\text{sys}}$  measurements are approximately 50% lower than the effective  $T_{\text{sys}}$  in each sideband after separation. A more accurate treatment requires an analysis of the gain ratio between

the sidebands. Then, the predicted system equivalent flux density (SEFD) can be derived as follows, where  $\eta$  is the aperture efficiency, and  $A$  is the collecting area of a single dish, and  $k$  is Boltzmann's constant.

$$\text{SEFD} = \frac{4kT_{\text{sys}}}{\eta A \sqrt{2}} = 11000 \left( \frac{T_{\text{sys}}}{120 \text{ K}} \right) \text{ Jy} \quad (2.15)$$

Thus, given our utilization of 3 GHz of IF bandwidth, SPRITE should achieve  $\sigma_S = \text{SEFD}/\sqrt{\Delta\nu} = 200 \left( \frac{T_{\text{sys}}}{120 \text{ K}} \right) \text{ mJy s}^{-1/2}$  rms noise. In practise, complex gain calibration uncertainties will add tens of percent of noise for phase-referenced observations.

### Verification of Sideband Separation

To verify proper timing accuracy and performance of the phase-switching system, we conducted an observation of SiO maser emission from R Leo (Balister et al., 1977). The  $J = 2 - 1$  rotational transition of SiO occurs at 86.243 GHz, thus should occur only in the lower sideband of our observations. In addition, we should also see a significant improvement in signal to noise of the maser signal after incorporating  $180^\circ$  phase switching to remove the effects of bright cross-talk. These results are shown in Figure 2.8. We observe that the maser emission is not present in the upper sideband, but is seen in the lower sideband at the correct frequency accounting for a slight redshift due to R Leo's motion relative to the observing reference frame. We also observe an  $\sim 8$  dB improvement in signal to noise ratio after subtracting (rather than adding)  $180^\circ$  phase-switched integrations. This improvement will be frequency dependent owing to frequency structure in the cross-talk.

### Baseline and Bandpass Solutions

Accurate bandpass and complex-gain calibration of SPRITE observing sequences requires a robust solution for the baseline geometry. The antenna positions are first measured to sub-centimeter accuracy using measurements of antenna locations post-processed using Canadian Spatial Reference System Precise Point Positioning program and a local global navigation satellite system (GNSS) base station. Refinement at the sub-millimeter level, required for 3 mm observations, was then done by fitting for errors in four 2-hr tracks on bright compact sources. In the presence of baseline errors, the final data after performing all of the calibration steps outlined in Section 2.3 will show a residual fringe,  $e^{i\phi}$ , with time and spectral dependence as below. The terms  $\Delta b$  represent  $x, y, z$  components of the baseline error while  $s(t)$



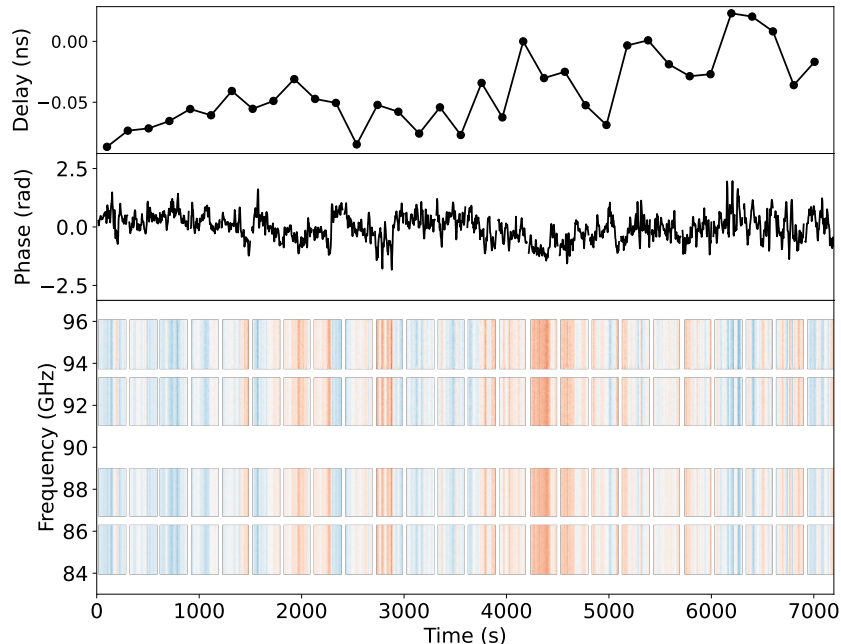


Figure 2.9: Behavior of phase as a function of time and frequency as seen on a 2 hour observation of bandpass calibrator source 3C84 after refinements to the baseline solution. In the bottom panel, red indicates negative phase, blue indicates positive phase, and white indicates zero phase. The top panel of this figure shows the small amount of delay variations over the whole observation. The middle panel shows a band-averaged measurement of phase as a function of time.

represents the time-dependent projected components of the unit source vector. The term  $\tau_i$  to account for any fixed instrumental delay errors.

$$\begin{aligned} \phi(t, \nu) = \frac{2\pi\nu}{c} [\Delta b_x s_x(t) + \Delta b_y s_y(t) \\ + \Delta b_z s_z(t) + c\tau_i] \end{aligned} \quad (2.16)$$

We use the residual fringe data to fit for the terms  $\Delta b_x, \Delta b_y, \Delta b_z, \tau_i$ . Figure 2.9 shows compelling evidence for a well-refined baseline as we see no rapid changes in phase both across the bandpass and in the time-series data over a 2 hour observation.

### Flux Calibration Solution

To verify our flux calibration procedure, as well as all other intra-sequence calibrations described above, we routinely observe ALMA calibrator sources.<sup>1</sup> Here we

<sup>1</sup><https://almascience.nrao.edu/sc/>

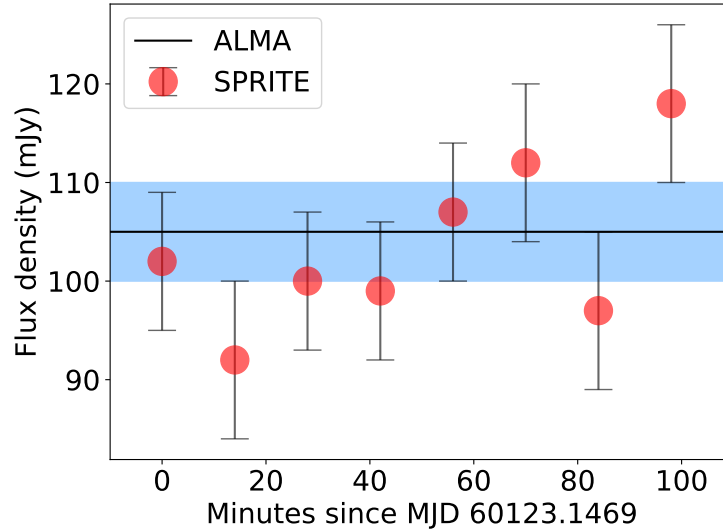


Figure 2.10: SPRITE measurements of the flux density of ALMA calibrator source J1342+2709 (red points). An ALMA measurement obtained 36 days earlier is indicated as a black line ( $1\sigma$  uncertainty shown as a blue shaded region).

present a 90 minute observation of J1342+2709, obtained on 2023 June 28, and last observed by ALMA on 2023 May 23 to be  $105 \pm 5$  mJy at 90.4 GHz. We reduced all scans on this source using the procedure outlined in Section 2.3. Bandpass calibration was performed using a 10 minute observation of 3C273. Flux calibration was performed by averaging two 10 minute observations of Uranus, obtained four hours apart. Individual 10 minute scans on J1342+2709 were interspersed with 1 minute scans on J1333+2725 for gain calibration. We show the results in Figure 2.10. Measurements in each scan are consistent with the ALMA result, and we measure a mean flux density over this observation of  $103 \pm 7$  mJy. The uncertainty includes statistical errors in the measurement, and in all calibrations; the dominant source of error is the flux calibration.

### End to end demonstration: S2 0109+22 and DQ Tau

We describe two examples of early science observations here that demonstrate the utility of an instrument like SPRITE. Results are shown in Figure 2.11.

SPRITE responded to an Astronomer’s Telegram report (Roesch et al., 2023) of unprecedentedly high cm-wavelength flux densities of the BL Lac object S2 0109+22 (e.g., Ciprini et al., 2004; MAGIC Collaboration et al., 2018). S2 0109+22 is detected from radio to VHE  $\gamma$ -ray wavelengths, and is a classical intermediate spectrum peak source at a redshift of  $\sim 0.36$ . The source is unlike other TeV

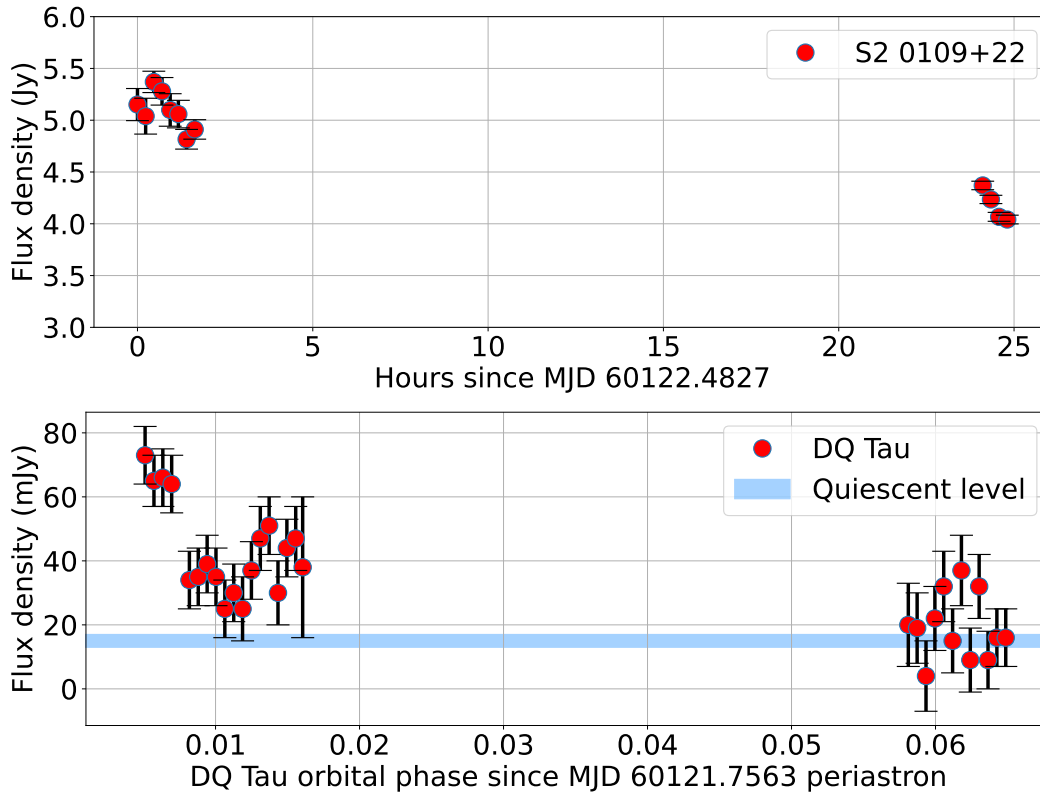


Figure 2.11: SPRITE measurements of the flux density of the flaring BL Lac object S20109+22 (top) and the binary classical T Tauri system DQ Tau (bottom). The blue shaded region in the bottom panel indicates an approximate quiescent level for the 90 GHz emission from DQ Tau (see text for details).

blazars in its high degree of optical polarization variability (7–30%), and its lack of correlation between the radio and optical lightcurves. The latter suggests that the radio and optical emission may not originate from the same zone of the jet. Roesch et al. (2023) measured flux densities of  $\sim 4$  Jy at 22 GHz and 40 GHz on 2023 June 15, in excess of the 0.3–3 Jy range observed over the past four decades at these frequencies. In agreement with previous estimates of the radio-mm spectral energy distribution (Ciprini et al., 2004), we observe brighter emission at 90 GHz on 2023 June 28–29, with detectable variability over 24 hr. The measured flux densities on these two days were  $5.1 \pm 0.3$  Jy and  $4.2 \pm 0.3$  Jy.

DQ Tau is an eccentric 15.8 day binary system of  $\sim 0.65M_{\odot}$  classical T Tauri stars (Mathieu et al., 1997). At periastron, the stars approach to within  $8R_{*}$ , suggesting that their magnetospheres briefly overlap. This appears to result in coincident millimeter (Salter, Hogerheijde, and Blake, 2008; Salter et al., 2010) and X-ray (Getman et al., 2011) flares. The millimeter flares are explained as synchrotron

emission from electrons accelerated in magnetic reconnection during periastron passage, and the observation of the Neupert effect in the relative timing of the millimeter and X-ray flares suggests that the same electrons are responsible for the non-thermal X-ray bremsstrahlung and the synchrotron emission. Despite the uniqueness of this system, only four millimeter observations of DQ Tau during periastron have been presented, with incomplete orbital-phase coverage. These observations indicate significant variations in the nature and timing of the periastron flares. We observed DQ Tau with SPRITE during a periastron passage on 2023 June 26 (ephemeris from Czekala et al., 2016), and detected significantly variable emission above the typical quiescent level of 13–17 mJy observed on the days surrounding periastron passage (Salter et al., 2010). The variability timescale and magnitude is consistent with previous observations of DQ Tau, with the exception of the initial extreme ( $\sim 0.6$  Jy) flare observed by Salter, Hogerheijde, and Blake (2008). Continued monitoring of periastron passages of DQ Tau by SPRITE will reveal the full phenomenology of these flares.

## 2.5 Future Observations

SPRITE will continue to observe every day with agreeable conditions. Our observations can currently be scheduled for blocks of up to 24 hours at once and include a mix of several classes of sources. We will spend several hours per day monitoring selections of nearby active stars in an experiment to measure the rate and luminosity function of millimeter flares (such as those reported in Guns et al., 2021). A few stars of interest include UV Ceti and YY Geminorum, which historically have been observed to have bright radio flares (Jackson, Kundu, and White, 1989). In light of new discoveries of millimeter emission from young stellar objects (e.g., Vargas-González et al., 2023), we also plan to monitor DQ Tau and similar systems. We also plan to continue monitoring nearby radio AGN of interest to millimeter VLBI observations, including M87 and Sgr A\*, along with samples of AGN selected for their interesting variability. In addition to routine monitoring, we also plan to schedule observations of any newly discovered and nearby transient sources, including supernovae (in particular those of Type II<sub>n</sub>; Yadlapalli, Ravi, and Ho, 2022), active x-ray binaries, and jetted tidal disruption events.

The instrument details described in this paper represent only a starting point for the full potential of SPRITE. In coming months and years, we plan to make a series of upgrades that will improve the sensitivity of the instrument. Adding a third antenna to SPRITE would provide a factor of  $\sqrt{3}$  improvement in sensitivity. The current

receiving system only supports total-intensity measurements presently, but introducing dual polarization capabilities would allow SPRITE to measure polarization fractions of sources and their variability, and would provide a sensitivity increase of  $\sqrt{2}$ . As mentioned in this work, SPRITE’s digital backend employs two stages of downconversion and the current correlator only supports utilization of 4 GHz out of the available 8 GHz of bandwidth. Development efforts for a future backend and correlator design to directly sample the full IF with more powerful ADCs are underway and offer both a  $\sqrt{2}$  improvement in sensitivity and mitigation of any additional losses in the system due to the signal passing through the second stage downconverter.

## 2.6 Conclusion

SPRITE represents a new resource to explore the growing field of millimeter transients. Taking a unique lower-sensitivity and non-imaging approach allows SPRITE to have a narrower focus purely on time-domain studies. Additionally, it demonstrates the capabilities of cost-effective and sustainable instrumentation to push forward ambitious science goals. This work outlines how we utilize a pre-existing antenna and receiver system with easily implemented backend and control-system upgrades to begin observations with SPRITE. Low-cost and scalable solutions, such as using the Red Pitaya device to handle lobe rotation and phase switching, may become more prevalent for future smaller-scale experiments. Another modern feature of SPRITE is its use of open-source software codebases, such as Astropy (Astropy Collaboration et al., 2022), to rapidly develop an integrated control and data-analysis software system.

Equipped with the flexibility to schedule observations without proposal-driven constraints, we aim to use SPRITE to monitor and follow-up bright and nearby transient sources. Systematic studies will fill in the rate and luminosity phase space of millimeter transient sources. High temporal resolution, especially at millimeter wavelengths, holds the power to unveil rapidly variable behavior and key physical properties of energetic synchrotron sources and their environments. As the era of wide-field synoptic surveys broadens in this coming decade, from new millimeter experiments such as CMB-S4 (Abazajian et al., 2019) to the nearly completed optical Vera Rubin Observatory, telescopes like SPRITE will become increasingly more important in the effort to characterize the plethora of interesting transients to be discovered.

## **2.7 Acknowledgements**

This research was partially supported by the National Science Foundation under grant AST-1935980, the Mt. Cuba Astronomical Foundation, and the OVRO Alan Moffet Funds. OVRO is located on the ancestral homelands of the Big Pine Paiute Tribe of the Owens Valley. We recognize and acknowledge the historical and cultural significance of these lands to members of the Tribe.

*Chapter 3***MODELS OF MILLIMETER AND RADIO EMISSION FROM INTERACTING SUPERNOVAE**

Nitika Yadlapalli<sup>1</sup>, Vikram Ravi<sup>1</sup>, Anna Y. Q. Ho<sup>2,3,4</sup>

**Abstract**

This work utilizes established models of synchrotron-powered light curves for core-collapse supernovae in dense circumstellar environments, namely type IIn and Ibn, to demonstrate the potential for detecting millimeter emission from these events. The progenitor types of these supernovae are still an open question, but using the synchrotron light curves as probes for the circumstellar environments could shed light on the mass-loss histories of the progenitors and discern between different theories. Observations in millimeter bands are particularly fruitful, as they probe regions at smaller radii and higher ambient densities, where centimeter emission tends to be self-absorbed. In our application of these light curves, we explore a diversity of progenitor types and mass-loss profiles to understand their effects on the light curve shapes. Additionally, we fit model parameters to the 8 GHz light curve of type IIn supernova 2006jd and then create millimeter light curves using these parameters to show the possibility of detecting an early millimeter peak from such an event. We predict that next generation millimeter surveys will possess the capability to detect nearby and extreme events. However, there is a pressing need for millimeter follow-up of optically discovered interacting supernovae to more completely sample the true population.

**3.1 Introduction****Millimeter Transients**

To date, the transient millimeter sky remains largely unexplored. In recent years though, millimeter transients have been discovered on timescales from minutes to months. The first blind survey for millimeter transients was conducted by Whitehorn

---

<sup>1</sup>Cahill Center for Astronomy and Astrophysics, MC 249-17 California Institute of Technology, Pasadena CA 91125, USA

<sup>2</sup>Miller Institute for Basic Research in Science, 468 Donner Lab, Berkeley, CA 94720, USA

<sup>3</sup>Department of Astronomy, University of California, Berkeley, Berkeley, CA, 94720, USA

<sup>4</sup>Lawrence Berkeley National Laboratory, 1 Cyclotron Road, MS 50B-4206, Berkeley, CA 94720, USA

et al., 2016 using the South Pole Telescope (SPT), which surveyed  $100 \text{ deg}^2$  of sky and discovered only one candidate transient at  $< 3\sigma$  significance. An improved transient search was conducted with the SPT-3G camera, covering a  $1500 \text{ deg}^2$  with deeper sensitivity (Guns et al., 2021). This search yielded 10 unique transient sources of which 8 were identified as flaring stars and 2 were identified as extragalactic events of unknown origin. Other blind detections of millimeter transients include 3 candidate stellar flares found serendipitously by the Atacama Cosmology Telescope (ACT; Naess et al., 2020). Though these works imply a higher event rate for millimeter stellar flares than previously known, the rates of extragalactic millimeter transients is still an open question.

Extragalactic transient millimeter emission arises from energetic synchrotron sources. Metzger, Williams, and Berger, 2015 and more recently Eftekhari et al., 2022 predict that wide-field millimeter surveys would be most sensitive to reverse shock emission from gamma-ray bursts (GRBs), such as those detected by De Ugarte Postigo et al., 2012 and Laskar et al., 2013. They also predict millimeter detections of tidal disruption events (TDEs), such as on-axis jetted sources like Swift J164449.3+573451 (Zauderer et al., 2011) or off-axis jetted sources like IGR J12580+0134 (Yuan et al., 2016). Optimistically, they additionally hope for a few detections of fast blue optical transients (FBOTs), such as nearby, luminous, millimeter transient AT2018cow (Ho et al., 2019a). However, detections of typical core-collapse supernovae (SNe) at millimeter wavelengths are scarce. Here we demonstrate the potential of early targeted observations of interacting SNe to dramatically increase the number of detections and probe the environments in which these explosions occur.

### **Millimeter Detectable Supernovae**

Core-collapse supernovae (CCSNe) result from the deaths of massive stars. There exists a broad diversity of flavors of CCSNe, usually arising from different progenitor types (see Smartt, 2009, and references within). The most commonly observed supernovae are type II-P, characterized by a plateau in the light curve following the initial decline from peak brightness. The plateaued light curve is powered by expansion of the photosphere due to recombination in the hydrogen envelope of a red supergiant (RSG) progenitor. Type II-L supernovae, characterized by a linearly declining light curve rather than a plateaued one, are similar to type II-P but arise from RSG progenitors that have stripped hydrogen envelopes. Type Ibc/Iib supernovae are also the products of stripped envelopes, but arise from massive Wolf-



Rayet (WR) stars rather than RSGs. Interacting supernovae, however, are unique because they have no distinctive progenitor type.

Interacting supernovae are identified by their bright, narrow spectral lines that arise from shock interaction with a very dense circumstellar medium (CSM; Chugai, 1990). Type IIn SNe spectra are dominated by hydrogen lines whereas type Ibn SNe show weak hydrogen but strong helium lines (see Smith, 2017, and references within for more detail). High velocity shocks, reaching up to a few percent of  $c$ , propagating through regions of density orders of magnitude greater than ISM ( $n_e \sim 10^6 \text{ cm}^{-3}$ ) are optimal conditions for producing bright radio and millimeter emission. Millimeter emission is especially important, as it peaks at early times when the shock radius is smaller and the CSM density is higher. Early time radio emission has been detected from type Ib/IIb SNe, such as the nearby SN 1993J (Pooley and Green, 1993), or from type Ibc events, such as SN1998bw (Kulkarni et al., 1998) or SN2009bb (Soderberg et al., 2010). A handful of Ib/IIb SNe have been detected in millimeter observations. The very nearby events SNe iPTF13bvn (Cao et al., 2013) and SN2011dh (Horesh et al., 2013), for example, were detected with the Combined Array for Research in Millimeter-wave Astronomy (CARMA), and were essential to constraining the early evolution of the shock radius and providing estimates of the pre-supernova mass loss rate. To date, only a handful of type IIn supernovae have been detected at radio wavelengths. Figure 7 in Chandra, 2018 summarizes detections of IIn supernovae at 8 GHz – we reproduce a few of these light curves here for reference in Figure 3.1. Notably, nearly all of the detections are made over a hundred days post-explosion. Bietenholz et al., 2021 show that the luminosity-risetime parameterization of radio emission from type IIn SNe is characterized by a significantly later time to peak than that of type Ib/c or other type II SNe. Thus observations at higher frequencies would prove useful in detecting the peak of the light curve at an earlier time. Type IIn and Ibn SNe have yet to be detected in the millimeter, but are likely to be millimeter-bright owing to their especially high CSM densities.

### **Diversity of Progenitor Models for Interacting Supernovae**

The nature of the progenitors for interacting supernovae is still unknown, owing to the spectacularly high observed mass-loss rates of up to  $0.1 M_{\odot}/\text{yr}$  and little understanding of the mechanisms driving this. Luminous blue variables (LBV), among the most luminous known stars, are commonly theorized to be IIn progenitors. Gal-Yam et al., 2007 provides the most direct evidence for this theory with

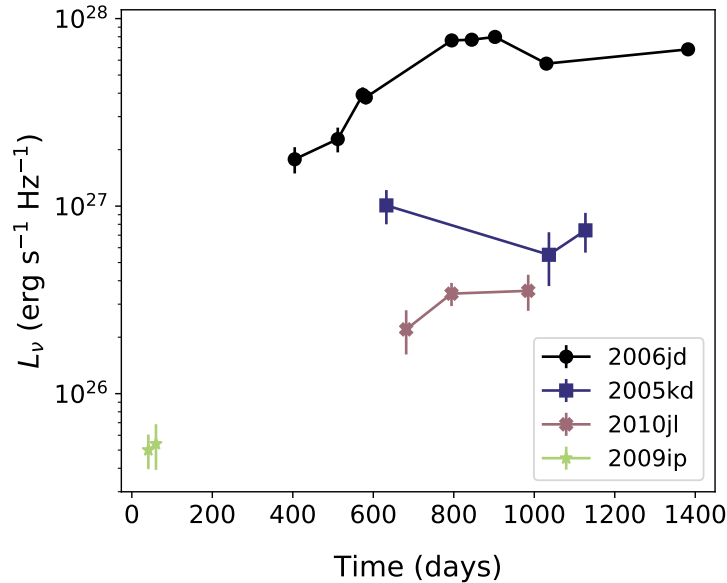


Figure 3.1: Reproduction of 8.5 GHz light curves of four type IIn SNe. This is meant to show the diversity of light curves that have been observed, highlighting the challenge in constraining a single progenitor model for these events. The data for these was taken from Chandra et al., 2012; Dwarkadas et al., 2016; Chandra et al., 2015; Margutti et al., 2014.

pre-explosion *Hubble Space Telescope* observations of IIn SN 2005gl that revealed a source coincident with the supernova position with a high luminosity that could only be explained by an LBV. Detections of pre-supernova outbursts also hint towards an LBV origin for IIn SN. Famously, SN 2009ip, originally thought to be a type II SN, was discovered to be a bright LBV-like outburst prior to a true IIn supernova explosion in 2012 (Mauerhan et al., 2013). The evolutionary pathway of LBVs, however, is still debated, casting doubt on their candidacy as IIn progenitors. Humphreys and Davidson, 1994 suggest that LBVs are O-type stars experiencing a period of high mass loss en route to becoming Wolf-Rayet (WR) stars; stars in this evolutionary stage would not be expected to explode as supernovae. Smith and Tombleson, 2015 offers a model of LBVs arising from binary evolution, which better fits a picture of LBVs as IIn progenitors. Blue supergiants (BSGs) have also been hypothesized to be IIn progenitors as models of BSG explosions are consistent with the types of precursor outbursts observed in events such as SN 2009ip and SN 2010mc (Smith, Mauerhan, and Prieto, 2014). Additionally, spatially resolved observations of the gas around VY CMa indicates that red supergiants (RSGs) may also have CSM structures that could give rise to IIn supernovae (Smith, Hinkle, and Ryde, 2009).

Thus, the ability to probe the CSM structure around observed supernovae has the power to shed light on the nature of their progenitors.

Observations of synchrotron powered light curves around the time of their peaks enable measurements of the radii and electron densities of the CSM the supernovae is interacting with at that time, using equations published in works such as Duran, Nakar, and Piran, 2013 and Ho et al., 2021. Constraining the shock velocity and the CSM density by these measurements allows constraints to be placed on the properties and mass-loss history of the progenitor, narrowing down viable progenitor models. As spherically expanding synchrotron sources will peak earlier in the millimeter than at lower frequencies, early millimeter observations are especially important in measuring the CSM density close to the surface of the progenitor, giving us a glimpse into the behavior of the progenitor in its final days to months.

In this paper, we model light curves of radio and millimeter emission from interacting supernovae. Section 3.2 goes through a summary of the emission and absorption models we use. Section 3.3 presents applications of this model to generate synthetic light curves of type II supernovae and Section 3.4 shows the potential for detecting these events with next generation cosmic microwave background (CMB) surveys. We conclude in Section 3.5.

### 3.2 Model Summary

Radio emission from supernovae originates in synchrotron radiation from free electrons in the CSM that are accelerated to relativistic energies by the forward supernova shock. The brightness and evolution of the emission is dependent on the density and structure of the CSM, as will be seen in the equations presented below as well as in the light curves presented in the following section. The aim of this section is not to present novel emission models, but to give an overview of well-established models that we utilize. We reproduce many relevant equations from the works cited in this section to highlight specific model parameters that we explore in the rest of this work.

For an interacting core-collapse supernova, the progenitor star undergoes pre-supernova mass loss in the decades leading up to the explosion (Smith, 2017, for example). The resulting CSM density can be modelled as power law described by  $\dot{M}$ , the mass loss rate, and  $v_w$ , the wind velocity, as shown in Equation 3.1.  $R_*$  is the radius of the progenitor star and  $s$  describes the steepness of the CSM density profile. A steady wind can be modelled with  $s = 2$ , but non-steady mass loss can

lead to deviations from this value. Equations 3.1 and 3.4 and much of the following formalism is introduced and explained in detail in Chevalier, 1982.

$$\rho_{CSM} = \frac{\dot{M}}{4\pi v_w R_*^2} \left( \frac{R_*}{R} \right)^s \quad (3.1)$$

Following the collapse of the core, a radiation dominated shock travels through the progenitor star until the shock reaches a radius that is optically thin to high energy photons. When the shock breaks out of the stellar surface, these high energy photons propagate through the CSM, giving rise to an ionization front. Works such as Nakar and Sari, 2010 and Kochanek, 2019 go into detail about models and observations of the shock breakout, but we consider a simplified case for this work.

The expansion of the ionization front is bounded by the speed of light and is given by Equation 3.2 where  $t$  is the elapsed time,  $Q$  is the number of ionizing photons per second, and  $m_p$  is the proton mass. The maximum radius of the ionization front, given in equation 3.3, is dictated by  $T$ , the duration of the breakout pulse. Assuming the shock breaks out at the stellar surface, the duration of the breakout pulse can be approximated by the light crossing time of the progenitor,  $T = R_*/c$ . For extreme CSM densities, the shock breakout may occur in the wind, but we ignore this possibility for now. We additionally ignore any recombination in the CSM.

$$R_{ion} = \frac{Q m_p v_w}{\dot{M}} t \leq ct \quad (3.2)$$

$$R_{ion,max} = \frac{Q m_p v_w}{\dot{M}} T \quad (3.3)$$

After the shock breakout, a forward shock continues to expand through the CSM. As the fastest moving unshocked ejecta reaches the decelerating shock front, a second shock known as the reverse shock forms. In the reference frame of the forward shock, the reverse shock propagates backwards and reheats the ejecta. It should be noted though that in the observer frame, the reverse shock is mostly moving radially outwards. The distinction between these two reference frames is important.

The boundary between the reverse shock and the forward shock is a contact discontinuity. We follow the discussion in Chevalier and Fransson, 1994 and Section 5.6 of Vink, 2020 for their derivations for shock radius and velocity. The shock behavior can be modelled by approximating the forward and reverse shocks as a

thin shell, meaning we assume that the radius of both the forward and reverse shock is approximately equal to the radius of the contact discontinuity. The radius and velocity of this shell is calculated by balancing the pressure difference across the contact discontinuity with the amount of deceleration. The reverse shock pressure near the contact discontinuity is dependent on the density profile of the supernova ejecta near the surface,  $\rho_{ej}$ , where  $n$  defines the power-law index of the density profile.

$$\rho_{ej} = \rho_o \left( \frac{t}{t_o} \right)^{-3} \left( \frac{v_{s,o} t}{r} \right)^n \quad (3.4)$$

The inner regions of the ejecta are assumed to have a flat density distribution. The initial density and velocity of this core are described by constants  $\rho_o t_o^3$  and  $v_{s,o}$ , which are derived using total ejecta mass,  $M_{ej}$ , and the kinetic energy of the ejecta,  $E_{kin}$ .

$$v_{s,o} = \sqrt{\frac{10 (n-5) E_{kin}}{3 (n-3) M_{ej}}} \quad (3.5)$$

$$\rho_o t_o^3 = \frac{M_{ej}^{5/2} E_{kin}^{-3/2}}{\frac{4\pi}{3} \left( \frac{n}{n-3} \right) \left( \frac{10}{3} \frac{n-5}{n-3} \right)^{3/2}} \quad (3.6)$$

The radius and velocity of the shell are then derived to be equations 3.7 and 3.8, respectively.

$$R_s(t) = \left[ \frac{4\pi(3-s)(4-s)\rho_o t_o^3 v_{s,o}^n v_w R_*^{2-s}}{(n-4)(n-3)\dot{M}} \right]^{1/(n-s)} \times t^{(n-3)/(n-s)} \quad (3.7)$$

$$V_s(t) = \frac{dR_s(t)}{dt} \propto t^{(3-s)/(2-n)} \quad (3.8)$$

As the shock expands through the ionized CSM, the free electrons are Fermi-accelerated through the shock to relativistic speeds with a power law distribution of energies as described by equation 3.9. The value of  $p$  is dependent on details of the shock acceleration process. Table 1 in Chevalier, 1998 compiles a list of SNe with observed indices. Many of these SNe have power law indices close to 3, though

some exhibit smaller values ranging as low as 2. In this work, we will consider the case of  $p = 3$ , but the results presented here do not change significantly based on the value of  $p$ .

$$N(E) \propto E^{-p} \quad (3.9)$$

We assume that all electrons are shocked to relativistic speeds and that the electrons always contribute a constant fraction,  $\epsilon_e$ , of the total energy density of the shocked gas. Applying the Rankine-Hugoniot jump conditions for the case of a fast shock (see Draine, 2011, for example), the post-shock energy density is

$$u_{tot} = \frac{9}{8} \rho_{CSM} V_s^2 \quad (3.10)$$

The strength of the emission also depends on the magnetic field behind the shock. We assume that the post-shock magnetic field energy density is a constant fraction,  $\epsilon_B$ , of the total energy density.

$$B = \sqrt{8\pi u_{tot} \epsilon_B} \quad (3.11)$$

For synchrotron sources, the frequency at which the source has an optical depth of unity is known as the synchrotron self-absorption (SSA) frequency,  $\nu_a$ . Above this frequency, the source will be optically thin and below this frequency the source will be optically thick. For a source of a given age, we can also define the cooling frequency,  $\nu_c$ . This is defined as the characteristic frequency of an electron that has radiated an amount of energy equivalent to its total energy. It is defined in equation 3.12, where  $m_e$  is the electron mass,  $q_e$  is the elementary charge, and  $\sigma_T$  is the Thomson cross section.

$$\nu_c = \frac{18\pi m_e c q_e}{\sigma_T^2 B^3 t^2} \quad (3.12)$$

The shape of the source spectrum depends on the ordering of  $\nu_a$  and  $\nu_c$ . The supernova shock will begin in the fast cooling regime, where  $\nu_c < \nu_a$ . Referencing equations in Appendix C of Ho et al., 2021, we can write expressions for  $\nu_a$  and the corresponding peak luminosity,  $L_a$ , for the fast cooling case.

$$\nu_a = R_s^{1/4} B^{3/4} t^{-1/4} \xi^{-1/8} \eta^{7/8} \quad (3.13)$$

$$L_a = 4\pi R_s^{21/8} B^{11/8} t^{-5/8} \xi^{-5/16} \eta^{35/16} \zeta \quad (3.14)$$

As the shock expands,  $v_a$  decreases with time while  $v_c$  increases. Eventually, the shock will enter the slow cooling regime where  $v_c > v_a$ . In this regime,  $v_a$  and  $L_a$  evolve as below.

$$v_a = R_s^{2/7} B^{9/7} \eta \quad (3.15)$$

$$L_a = 4\pi R_s^{19/7} B^{19/7} \eta^{5/2} \zeta \quad (3.16)$$

The constants  $\xi$ ,  $\eta$ , and  $\zeta$  are defined as follows.

$$\xi = \frac{\sigma_T^2}{18\pi m_e c q_e} \quad (3.17)$$

$$\eta = \left( \frac{\sigma_T}{12\pi^2 m_e^2 c} \right)^{2/7} \left( \frac{q_e}{2\pi m_e c} \right)^{1/7} \quad (3.18)$$

$$\zeta = \frac{1}{3} (2\pi m_e)^{3/2} \left( \frac{c}{q_e} \right)^{1/2} \quad (3.19)$$

In both the slow and fast cooling regime, the optically thick part of the spectrum goes as  $L_\nu \propto \nu^{5/2}$ . The optically thin part of spectrum goes as  $L_\nu \propto \nu^{-p/2}$  in the case of fast cooling. When the shock transitions to slow cooling, the optically thin part of the spectrum goes as  $L_\nu \propto \nu^{-(p-1)/2}$  for  $v_a < \nu < v_c$  and shifts to  $L_\nu \propto \nu^{-p/2}$  for  $\nu > v_c$ . See Spectra 2 and 3 within Figure 1 of Granot and Sari, 2002 for a visualization of this. The functional definition of these spectra is given in equation C17 of Ho et al., 2021.

The emission is additionally absorbed in the ionized CSM due to free-free absorption (FFA). A frequency dependent correction must be applied to the spectrum by multiplying by  $e^{-\tau_\nu^{\text{FFA}}}$ , where  $\tau_\nu^{\text{FFA}}$  is given in equation 3.20. In the calculation of the free-free opacity, the value of  $\kappa_\nu^{\text{FFA}}$  is derived in Panagia and Felli, 1975.

$$\tau_\nu^{\text{FFA}} = \int_{R_s}^{R_{\text{ion}}} \kappa_\nu^{\text{FFA}} n_e n_i ds \quad (3.20)$$

$$\kappa_v^{\text{FFA}} = 4.74 \times 10^{-27} \left( \frac{v}{1 \text{ GHz}} \right)^{-2.1} \left( \frac{T_e}{10^5 \text{ K}} \right)^{-1.35} \quad (3.21)$$

### 3.3 Application to Type IIn/Ibn Supernovae

#### Model Light Curves

In this section, we present radio light curves of forward shock emission arising from a variety of interacting supernovae conditions. Given the broad range of viable progenitor models for interacting supernovae, we consider three progenitor types: RSGs, BSGs, and WR stars. We expect the RSG and BSG progenitors to represent light curves for type IIn supernovae and WR progenitors to represent light curves for type Ibn supernovae. The synchrotron emission model we detail in Section 2 is applicable to both scenarios. Each progenitor model varies in its breakout radius, wind velocity, and shock breakout pulse luminosity. We adopt the same radii and breakout luminosities for the progenitor models as those used in Nakar and Sari, 2010. We chose a characteristic RSG wind velocity of 20 km/s based on data on nearby RSGs (Mauron and Josselin, 2011). OB type stars have wind velocities on the order of their escape velocities, so for our BSG and WR model we choose wind velocities of 250 and 1000 km/s, respectively. We assume an explosion energy of  $E = 10^{51}$  ergs and an ejecta mass of  $M_{ej} = 5 M_{\odot}$ . The fraction of energy in electrons and magnetic fields is fixed to  $\epsilon_e = \epsilon_b = 1/3$ .

Our choices in parameter exploration are in part informed by modelling work done by Moriya et al. (2014) to fit bolometric light curves of type IIn SNe. Figure 9 in this work shows a range of estimated mass-loss rates from various type IIn SNe – from this, we choose to explore three different mass loss rates in this work  $\dot{M} = 10^{-2}, 10^{-3}$ , and  $10^{-4} M_{\odot}/\text{year}$ . Moriya et al. (2014) also infers the CSM density slope,  $s$ , for each of these light curves. We explore parameters between  $1.6 < s < 2.2$ , but refer to Moriya and Tominaga (2012) for a more detailed discussion on the important effect of the density profile on the resultant optical light curves. We note too that we assume an infinite wind and a fixed CSM density slope. For piecewise varying CSM models, we refer readers to works such as Matsuoka et al. (2019), which present hydrodynamical simulations of radio light curves resulting from shock interaction with a confined CSM.

Figure 3.2 shows light curves for combinations of the three progenitors and three mass-loss rates at two frequencies, 10 GHz and 100 GHz, and two ionized CSM temperatures,  $T_e = 10^4$  and  $10^5$  K. Ejecta and CSM density profile indices are fixed to



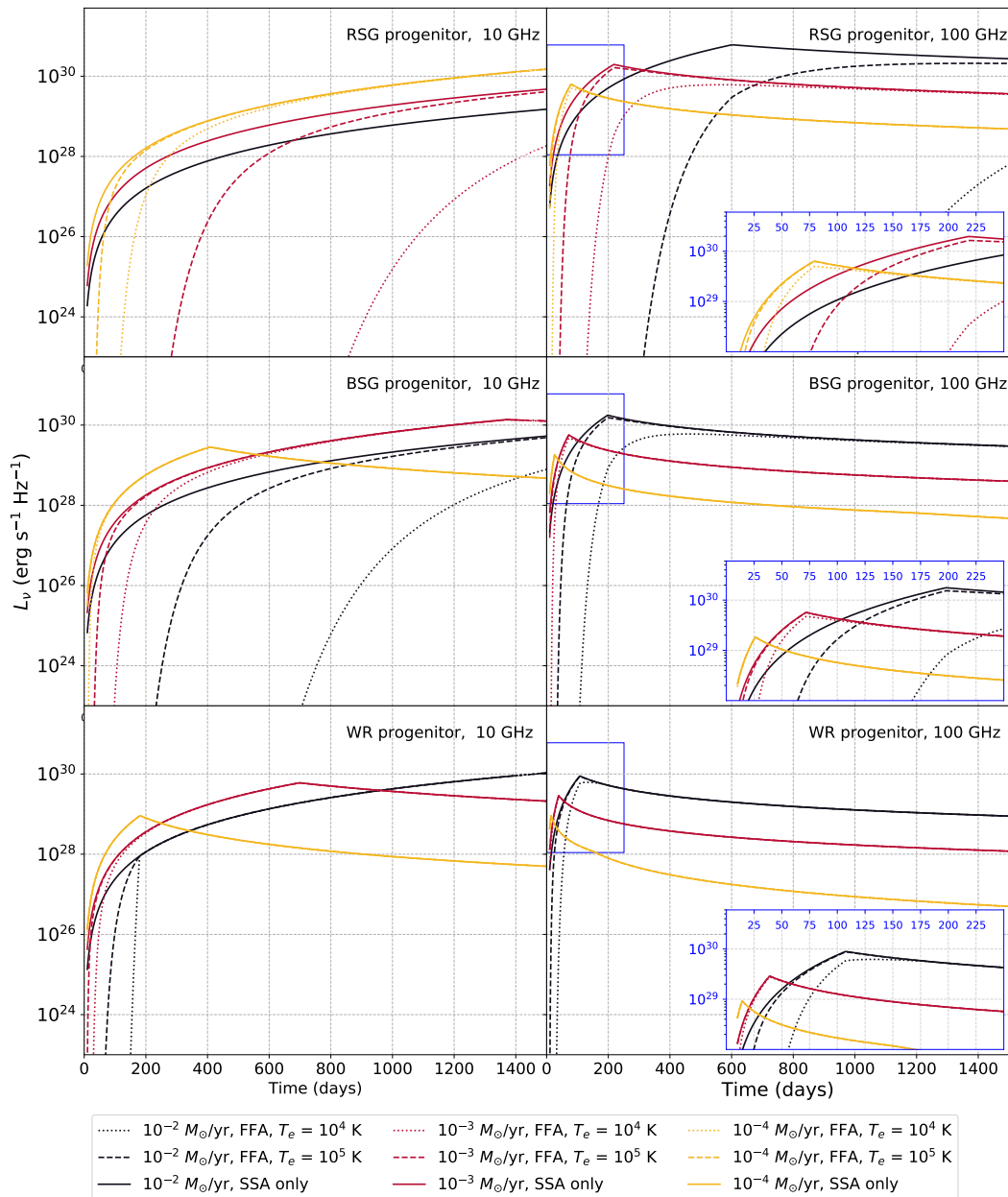


Figure 3.2: Light curves at 10 GHz and 100 GHz of synchrotron emission originating in the forward shock of an interacting supernova. Three absorption cases are shown here: SSA only, SSA + FFA assuming a  $10^5 \text{ K}$  CSM, and SSA + FFA assuming a  $10^4 \text{ K}$  CSM. The extent of the ionized region contributing to FFA is calculated given the shock breakout pulse properties. We use progenitor radii of  $500 R_\odot$  (RSG),  $70 R_\odot$  (BSG), and  $5 R_\odot$  (WR) and pulse luminosities as shown in Figure 5 of Nakar and Sari, 2010. We use steady wind velocities of  $20 \text{ km/s}$  (RSG),  $250 \text{ km/s}$  (BSG), and  $1000 \text{ km/s}$  (WR). The RSG and BSG scenarios represent type IIIn SNe while the WR scenario represents a type Ibn SNe. For the 100 GHz light curves, we show a zoomed in panel of the first 250 days to better visualize the time scale of the millimeter peaks. For scale,  $\sim 10^{28} \text{ erg s}^{-1} \text{ Hz}^{-1}$  is about 1 mJy at  $\sim 100 \text{ Mpc}$ .

$n = 10$  and  $s = 2$  in this example. The dotted and dashed lines in this figure represent emission that one may observe, taking into account free-free absorption. Models including only synchrotron self-absorption, shown by solid lines, are included for comparison. These light curves illustrate the limits on searching for lower frequency radio emission from interacting supernovae. For example, for a supernova exploding from an RSG progenitor with a mass-loss rate of  $10^{-4} M_{\odot}/\text{year}$ , akin to a star like VY CMa, the 10 GHz emission could not reasonably be detected until around 200 days for the coolest CSM temperature of  $10^4$  K. The 100 GHz emission from the same event, however, peaks sooner than 100 days, yielding information about the CSM structure much closer to the progenitor surface than the 10 GHz emission. Similarly, in the BSG case, 100 GHz observations are essential to observe any early time emission from progenitors with mass-loss rate with  $10^{-2} M_{\odot}/\text{year}$ . For WR progenitors, the high wind velocities and small progenitor radii decrease the CSM densities as well as limit the extent of the ionization front, making free-free absorption much less of an issue in observing type Ibn supernovae, compared to IIn. For all progenitor types however, the millimeter light curve peaks much earlier than the radio light curve. This is because as the source radius increases and the shock decelerates, the SSA frequency decreases. As we will show in the next section, applying a model fitting approach to gleaning information from the light curve provides the most discerning information when detections are made around the peak. Thus, even independent of the problem of absorption, studies of interacting supernovae would greatly benefit from early time millimeter observations.

We also explore the effect of different ejecta and CSM density profiles as well as the initial explosion energy on the 100 GHz and 10 GHz light curves. To do this, we start with an RSG model and fix  $\dot{M} = 10^{-3} M_{\odot}/\text{yr}$ ,  $T_e = 10^4$  K, and  $M_{ej} = 5 M_{\odot}$ . In the upper panel of Figure 3.3, we fix  $s = 2$  and  $E = 10^{51}$  ergs and vary the ejecta density power-law index in integer steps from 8 to 12. In the middle panel, we fix  $n = 10$  and  $E = 10^{51}$  ergs, and vary the CSM density power-law index  $s$  from 1.6 to 2.2 in steps of 0.2. In the bottom panel, we fix  $s = 2$  and  $n = 10$  and vary the initial explosion energy between  $5 \times 10^{49}$  ergs  $< E < 10^{51}$  ergs. The trends discussed below hold for both the BSG and WR models as well, varying only in the exact values of the peak time and luminosity. For brevity, we show only plots produced for the RSG model.

Figure 3.3 shows that the millimeter and radio light curves are most sensitive to changes in explosion energy and CSM density profile. The middle panel of

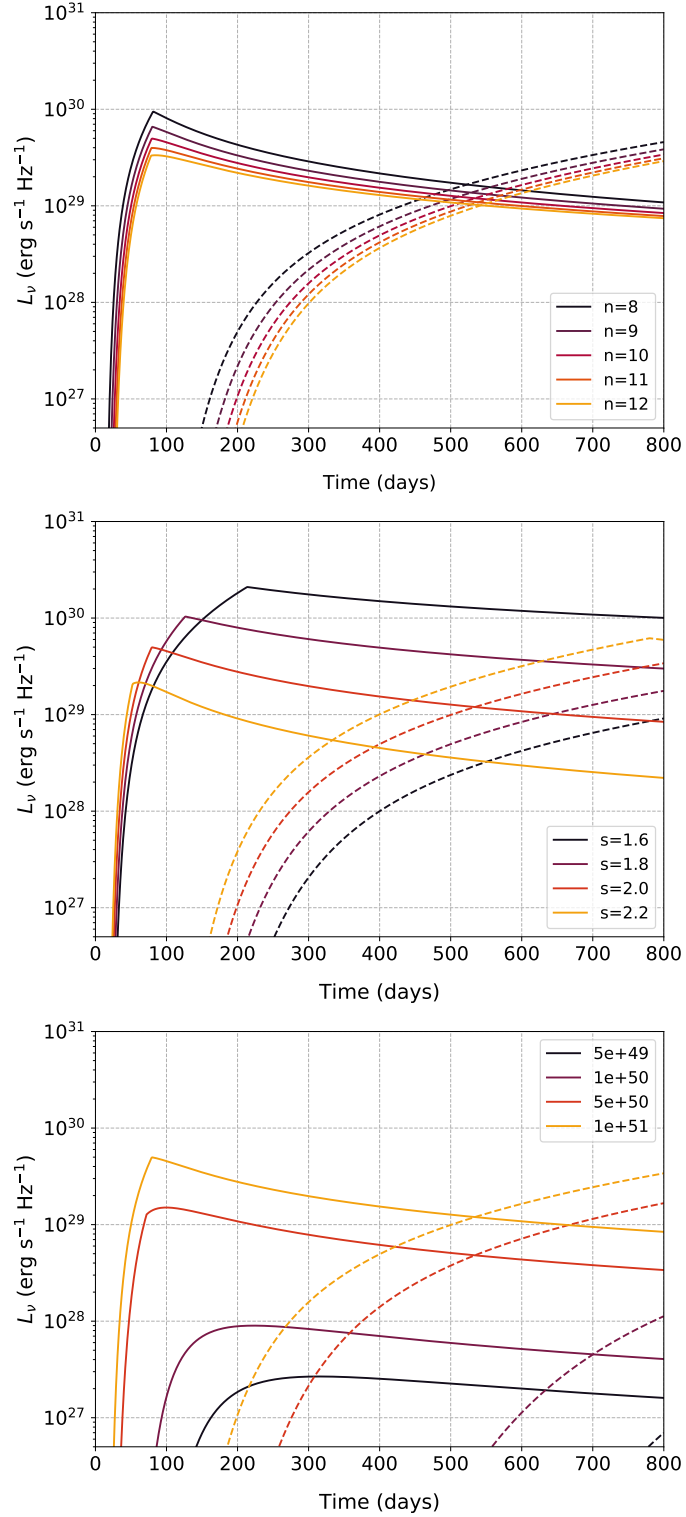


Figure 3.3: Light curves at 100 GHz (solid lines) and 10 GHz (dashed lines) showing the effects of different ejecta and CSM radial profiles. Adopting an RSG progenitor model and keeping constant  $\dot{M} = 10^{-3} M_\odot/\text{yr}$ ,  $T_e = 10^4 \text{ K}$ ,  $E = 10^{51} \text{ ergs}$ , and  $M_{ej} = 5 M_\odot$ , the upper panel assumes  $s = 2$  and varies the ejecta profile index,  $n$ , while the middle panel assumes  $n = 10$  and varies the CSM profile index,  $s$ . The bottom panel assumes  $s = 2$  and  $n = 10$  and varies the explosion energy.

Figure 3.3 shows that for a fixed mass-loss rate, decreasing  $s$  increases the peak luminosity of the millimeter light curve. This is because while a steady wind is modelled with  $s = 2$ , a value of  $s < 2$  represents that in the past, the progenitor had a mass-loss rate higher than  $\dot{M} = 10^{-3} M_{\odot}/\text{yr}$  but the mass-loss slowed leading up to the time of explosion. A value of  $s > 2$ , however, indicates that the mass-loss rate increased with time up to  $\dot{M} = 10^{-3} M_{\odot}/\text{yr}$  leading up to the time of explosion. Thus, the trends shown here reflect the fact that the  $s < 2$  CSM scenarios presented result in the supernova shock interacting with more total mass which powers a brighter light curve. As  $s$  decreases, the shape of the light curve post-peak flattens as well, resulting from the sustained higher CSM densities at larger radial distances.

Decreasing  $E$  also dramatically changes the light curve shape by flattening the peak and decreasing the peak luminosity. Comparing the curves at various energies to those light curves shown in Figure 3.1 already shows preliminarily that for type II<sub>n</sub>, relatively lower energy explosions can still be responsible for bright radio emission. The ejecta density profile, however, has minimal effect on either the radio or millimeter light curves, indicating that detections of these events will not discern between different models of  $n$  for the progenitor. Taking into the account all of these parameters is crucial to painting a more complete picture of the explosion and the progenitor's history.

### **Case Study: SN 2006jd**

To illustrate an application of the modelling described in the previous section, we fit model light curves to 8.5 GHz detections of SN 2006jd. SN 2006jd was discovered on 2006 October 12 (Blondin et al., 2006). It was originally classified as a type II<sub>b</sub> SN and noted for its spectral similarity to SN 1993J, though it was later reclassified as a type II<sub>n</sub>. Most type II<sub>n</sub> supernovae have very little, if any, monitoring with radio telescopes. For 2006jd, however, Chandra et al., 2012 reports on four years of follow-up observations of the event with the Very Large Array (VLA), ranging from 400 to 2000 days post-explosion. We convert the flux densities reported in Chandra et al., 2012 to luminosities using a distance of 79 Mpc to the event and utilize `emcee` (Foreman-Mackey et al., 2013) to explore combinations of model parameters that may fit the data. For a given progenitor model, we allow parameter exploration of mass loss rate, CSM temperature, explosion energy, ejecta mass, ejecta density profile index, and CSM density profile index. We use broad tophat priors for the parameters, but we note that when applying this modelling to newly discovered events, priors should be informed by interpretation of early detections in optical and

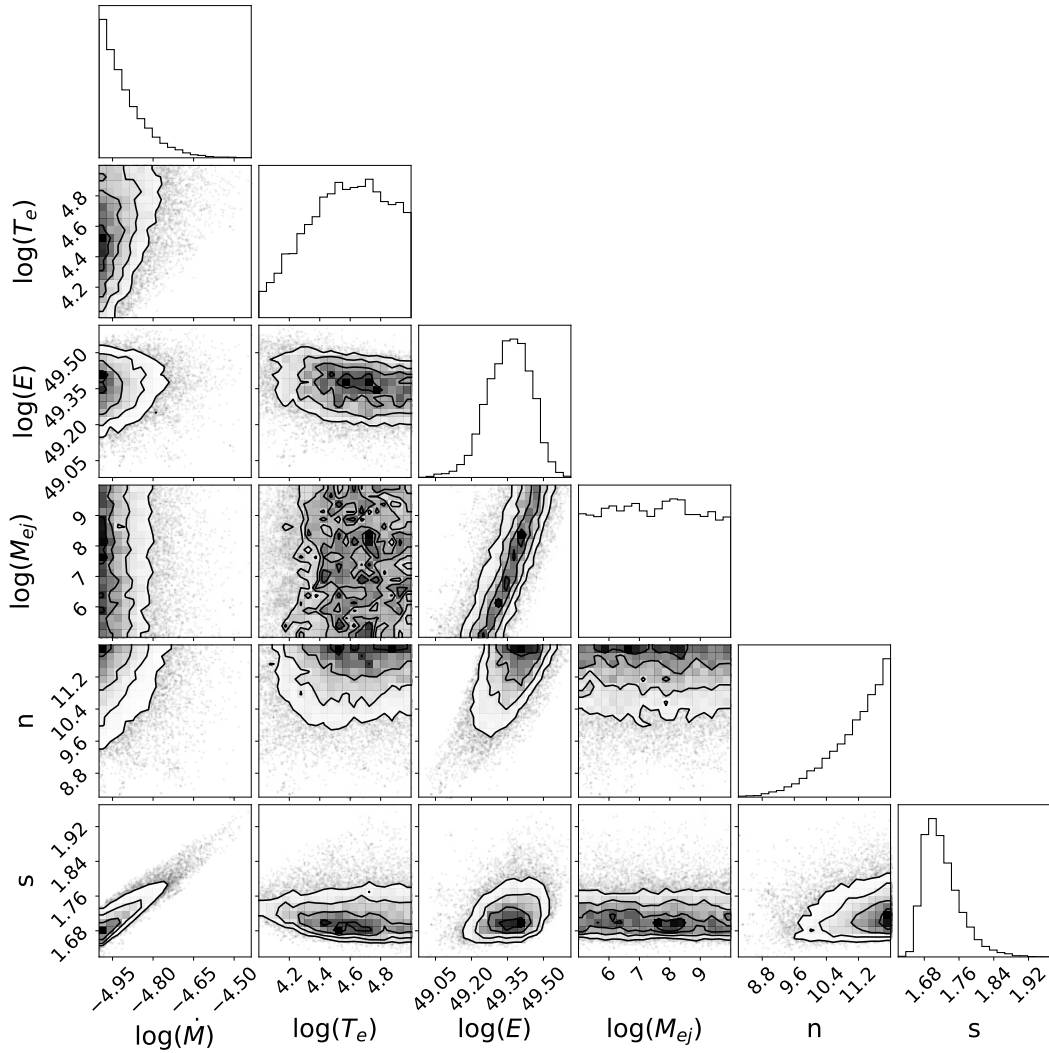


Figure 3.4: Corner plot showing posterior distributions of parameters used to generate a best fit model light curve for the 8.5 GHz data of SN 2006jd. Not all of the parameters are well constrained in this analysis, indicating that late time radio data alone is not sufficient to understand these events.

other wavelengths. The parameter posterior distributions for 2006jd assuming an RSG progenitor is shown in Figure 3.4.

We note a few interesting characteristics of the posteriors and compare them with Chandra et al., 2012 as well as Moriya et al., 2013. The latter work uses a similar shock evolution model as us and analytically models bolometric light curves for type II<sub>n</sub> SNe model using a power law declining luminosity. Our results are generally consistent with both of these works. We find that a CSM density profile around  $s = 1.7$  is preferred for 2006jd, which matches closely with the  $s = 1.77$  preferred

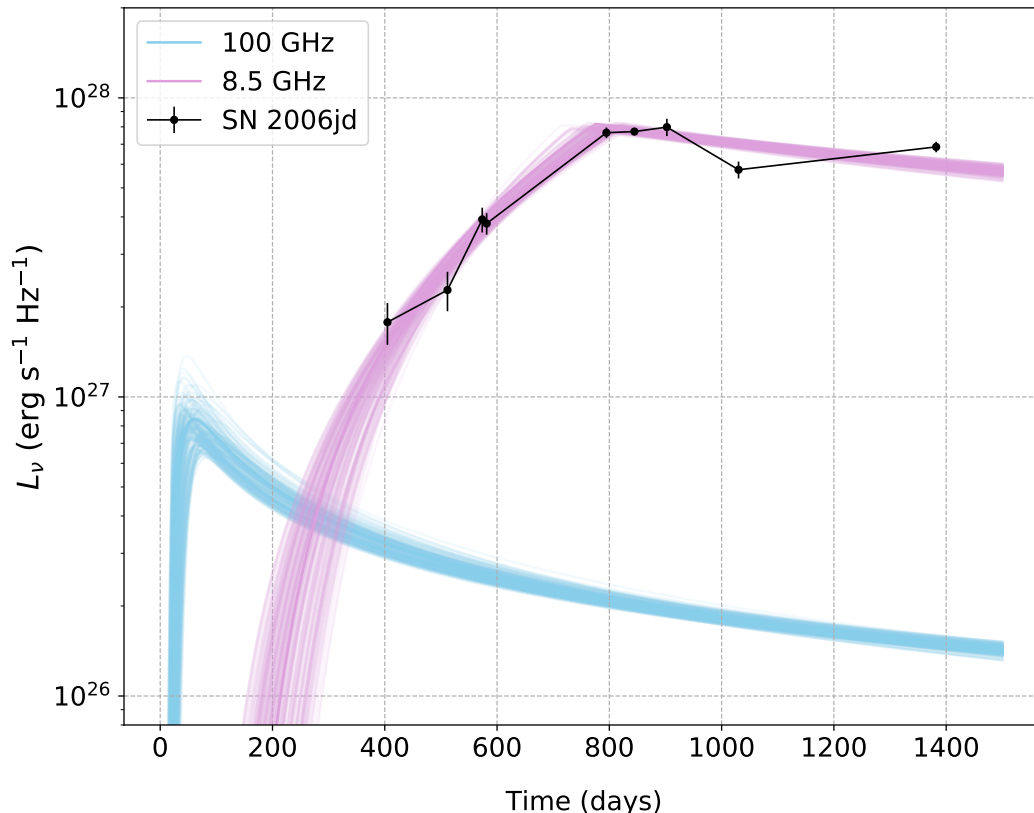


Figure 3.5: Light curves at 8.5 GHz generated from 200 random samples from the MCMC fit to the SN 2006jd data. Using the same random samples, light curves are also generated at 100 GHz. Using all 2000 samples generated in our MCMC analysis, the mean peak location of the 8.5 GHz light curves occurs around 794 days, with a  $1\sigma$  spread of 23 days. The mean peak location of all 100 GHz light curves occurs around 61 days with  $1\sigma = 15$  days. The potential for detecting the millimeter light curve peak demonstrated here highlights the need for sensitive and early-time follow up observations of sources such as SN 2006jd.

in Chandra et al., 2012 but deviates slightly from the  $s = 1.4$  preferred to Moriya et al., 2013. However, the fact that all of the values are significantly below 2 indicate a shared conclusion that episodic mass-loss may be responsible for the CSM enrichment in 2006jd. We also find that the light curve models are not very sensitive to  $M_{ej}$  or  $n$ , similar to Moriya et al., 2013 where changing these values alters the explosion energy and mass-loss rate by only around  $\sim 10\%$ .

Our results for the most likely explosion energy and mass-loss rate, however, deviate from those found in Moriya et al., 2013. We find an explosion energy requirement of only  $\sim \text{few} \times 10^{49}$  ergs and a small mass-loss rate of  $\dot{M} \sim 10^{-5} M_{\odot}/\text{yr}$ . In contrast, the fits to the bolometric light curves of 2006jd in Moriya et al., 2013 yielded an

energy requirement of  $\sim 10^{52}$  ergs and a higher mass-loss rate of  $\dot{M} \sim 10^{-3} M_{\odot}/\text{yr}$ . Moriya et al., 2014 estimates the mass-loss history of several type IIIn SNe and indicates a slowing in the already especially low amount of mass lost from the 2006jd progenitor in the final days before explosion. Thus, fitting one fixed value of  $\dot{M}$  will likely lead to an imprecise model over longer spans of time. Another source of discrepancy likely arises from the fact that these light curve models estimate the amount of energy needed to power just the synchrotron emission. As synchrotron emission traces only the fastest moving ejecta, it does not represent the full energy budget for the explosion. However, the true fraction of the total energy it represents is impossible to constrain. As a final note on the posteriors, the light curve model appears to weakly prefer a  $T_e \sim 4 \times 10^4$ , but we interpret this with caution as we do not expect late time data to constrain this parameter given that especially for a low mass-loss rate the shock would be in a regime that is optically thin to free-free by then.

These comparisons to Chandra et al., 2012 and Moriya et al., 2013 are meant only to confirm the validity of our posteriors, not to claim new insight on 2006jd. The aim of this section is to demonstrate the potential for observing millimeter flux from interacting supernova by inferring from previous radio detections. In Figure 3.5, we show model 8.5 GHz light curves generated using parameters from 200 random samples from the MCMC chains. For the sample parameters, we generate light curves at 100 GHz as well. These light curves demonstrate that for parameters that generate late time emission in a fairly narrow range of possible luminosities at 8.5 GHz, they generate early peaks at a diversity of possible luminosities for 100 GHz. A 100 GHz peak of  $\sim 10^{27} \text{ erg s}^{-1} \text{ Hz}^{-1}$  at the distance of 2006jd corresponds to a flux density of  $\sim 140 \mu\text{Jy}$ . A significant detection of this flux density can easily be made with facilities like the Atacama Large Millimeter/submillimeter Array (ALMA).

### 3.4 Rates of Detection in Blind Surveys

Serendipitous millimeter transient detections are expected to increase in the era of wide-field CMB surveys. We explore their potential to detect type IIIn supernovae in a blind search by comparing the areal densities of the supernovae with the surveys' areas and point source sensitivities. The areal density represents the number of sources we expect to detect in the sky per square degree at any given time. Thus, it is dependent on the volumetric event rate as well as the characteristic event timescale.

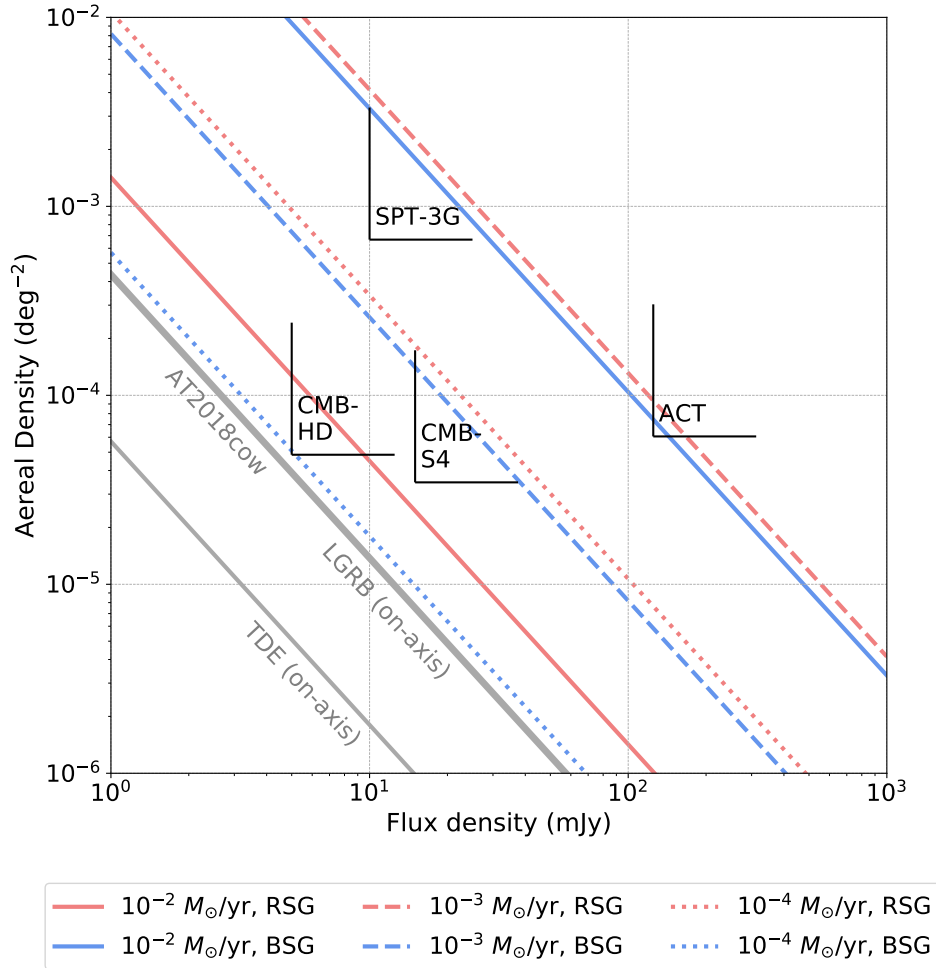


Figure 3.6: Areal densities of interacting SNe as a function of their flux densities for various progenitor models. Three mass loss rates are depicted,  $\dot{M} = 10^{-2} M_{\odot}/\text{yr}$ ,  $\dot{M} = 10^{-3} M_{\odot}/\text{yr}$ , and  $\dot{M} = 10^{-4} M_{\odot}/\text{yr}$ . All models have values of  $T_e = 10^4 \text{ K}$ ,  $E = 10^{51} \text{ ergs}$ ,  $M_{ej} = 5 M_{\odot}$ ,  $n=10$ , and  $s=2$ . Also shown are limiting areal densities for the  $5\sigma$  detection thresholds for four different CMB surveys. For comparison, areal densities of other millimeter-bright astrophysical events are also included. The line for AT2018cow is generated using values given in Ho et al., 2021, while the lines for on-axis long gamma-ray bursts (LGRB) and on-axis tidal disruption events (TDE) use values given in Eftekhari et al., 2022.

To derive a volumetric rate for type II<sub>n</sub> SNe, we rely on the Zwicky Transient Facility's (ZTF) Bright Transient Survey (BTS) which recently provided statistics for supernova demographics, including corrections for various sources of inefficiency (Perley et al., 2020). They conclude that the rate of core-collapse supernovae is  $1.01 \times 10^5 \text{ Gpc}^{-3} \text{ yr}^{-1}$  and that 10.2% of those are classified as type II<sub>n</sub>. Thus, we adopt a type II<sub>n</sub> supernova rate of  $1.03 \times 10^4 \text{ Gpc}^{-3} \text{ yr}^{-1}$ . We consider supernovae



with RSG and BSG progenitors and three different mass-loss rates, assuming fixed parameters of  $T_e = 10^4$  K,  $E = 10^{51}$  ergs,  $M_{ej} = 5 M_\odot$ ,  $n=10$ , and  $s=2$ .

For each model, we set the characteristic timescale of the light curve by computing the amount of time between the luminosity reaching half the peak luminosity. We can compute the flux densities we expect to observe for a range of distances. The distances we consider are within a few hundred Mpc, chosen to roughly correspond to the flux density sensitivity limits of relevant millimeter surveys. Using the IIn SNe event rate given above, we can compute the number of supernovae per year that exhibit a half-peak brightness above a given flux density. Multiplying by the light curve timescale and dividing by the total number of degrees in the full sky then yields areal density. Figure 3.6 shows these lines of supernova areal density as a function of half-peak flux density for the various models.

In Figure 3.6, we also show the limiting areal densities and flux densities of four CMB surveys of interest. Surveys are sensitive to sources with areal densities greater than  $1/\text{FOV deg}^{-2}$  at a  $5\sigma$  detection. The SPT observes a  $1500 \text{ deg}^2$  area of sky down to  $\sigma = 2$  mJy in their 95 GHz band (S. Gunns, 2021, personal communication) while the ACT observes 40% of the sky every week down to a  $\sigma = 25$  mJy in their 90 GHz band (K. Huffenberger and S. Naess, 2021, personal communication). The SPT is within the threshold of being to observe supernovae with progenitors undergoing amongst the most extreme mass-loss cases we consider in this work, while the ACT is unlikely to observe anything. This is consistent with the rate and types of extragalactic transients these surveys have already found. CMB-S4 is a next generation CMB survey with stations in both Chile and the South Pole. It is expected to conduct deep observations of 70% of the sky, covering frequencies between 30-280 GHz (Abazajian et al., 2019). The experiment also expects to deliver observations of transient sources using a difference imaging pipeline. At 95 GHz, CMB-S4 will achieve  $\sigma = 3$  mJy in a one week stack. Looking further to the future, CMB-HD is a new experiment proposed for the Astro2020 Decadal Survey. Projected to have more frequency bands and observe deeper, CMB-HD expects to observe 50% of the sky and achieve  $\sigma = 1$  mJy for detecting transients. We expect that these two next generation CMB experiments to have the potential to detect bright and local type IIn supernovae, as they lie within the requirements of sensitivity and areal density to observe a broader range of progenitor mass-loss rates.

We caution that the supernova areal densities we present are likely optimistic. Several progenitor scenarios may contribute to the population of type II<sub>n</sub> supernovae that have been observed to date, and we do not believe that any of these lines of areal density are representative of the true sample of events. Additionally, we have assumed that  $\epsilon_e = \epsilon_b = 1/3$ . Lower energy fractions could yield significantly lower light curve luminosities, decreasing the rates of detection we predict for these surveys. We also assume homogenous CSM structure when in reality, CSM interaction is often complicated by inhomogenous structure and asymmetry and may require more sophisticated modelling to properly describe it. Given this, blind surveys should be able to detect a sample of the most nearby and most extreme type II<sub>n</sub> SNe. Follow up millimeter observations of optically discovered SNe would supplement these detections, shedding light on the range of possible progenitors and mass-loss histories that produce these types of events.

### 3.5 Conclusion

The main goal of this work was to demonstrate the utility of early millimeter observations of supernovae interacting with dense circumstellar environments. A variety of progenitor models have been proposed for these events, but discerning between different theories requires knowledge of the progenitor's pre-explosion behavior. Probing the CSM into which a supernova explodes can give us insight into the final days of stellar evolution for massive stars and better constrain the viability of different progenitor models.

Here, we apply a synchrotron emission model that takes into account slow versus fast cooling regimes and free-free absorption to produce millimeter and radio light curves of interacting SNe. The light curves are generated by using the prescription of shock radius and velocity evolution outlined in Chevalier, 1982 and assuming that a constant fraction of the total shock energy goes into electrons and magnetic fields. The model light curves of the first 1500 days post-explosion reveal that millimeter emission peaks significantly sooner than lower frequency radio emission, making it an important probe of the CSM density close to the surface of the progenitor. The light curves are most sensitive to changes in explosion energy and CSM density profile but are fairly insensitive to changes in the ejecta density profile.

For a practical application, we utilize `emcee` to fit parameters of synchrotron-powered light curve models to an 8 GHz light curve of type II<sub>n</sub> SNe 2006jd. We find that the light curve was most likely generated by a low energy explosion and a

relatively low amount of mass-loss enriching the CSM but with a profile indicative of non-steady mass-loss. The model fitting was not very sensitive to the CSM temperature or the total ejecta mass. Millimeter light curves generated by random samples of parameters from the analysis show the possibility of an early and luminous peak with potential for detection by sensitive instruments such as ALMA.

In the upcoming era of wide-field CMB surveys, we believe there is potential for blind detections in the millimeter band of especially luminous and nearby interacting SNe. Combining these with millimeter followup observations of SNe discovered in optical surveys, a representative sample of interacting SNe can be built. Given millimeter light curves, fitting to the models described here presents a method to solve for first-order estimates of the viable progenitor and CSM parameters that describe the emission. Interpreting their millimeter light curves in conjunction with multi-wavelength observations will be key in broadening our understanding of the evolution and mass-loss histories of massive stars that lead to these events.

The code used to generate the figures shown in this paper can be found at <https://github.com/nitikayad96/mmbrightsupernovae>.

### **Acknowledgements**

We thank Sterl Phinney and Abigail Polin for useful discussions in formulating the model for this work. We also thanks Sam Guns for discussions regarding the SPT-3G as well as Sigurd Naess and Kevin Hufferberger for discussions regarding the ACT. This research has made use of NASA's Astrophysics Data System Bibliographic Services.

*Chapter 4*VLBA DISCOVERY OF A RESOLVED SOURCE IN THE  
CANDIDATE BLACK HOLE X-RAY BINARY AT2019WEYNitika Yadlapalli<sup>1</sup>, Vikram Ravi<sup>1</sup>, Yuhan Yao<sup>1</sup>, S. R. Kulkarni<sup>1</sup>, Walter Brisken<sup>2</sup>**Abstract**

AT2019wey is a Galactic low mass X-ray binary with a candidate black hole accretor first discovered as an optical transient by ATLAS in December 2019. It was then associated with an X-ray source discovered by SRG/eROSITA and SRG/ART-XC instruments in March 2020. After a brightening in X-rays in August 2020, VLA observations of the source revealed an optically thin spectrum that subsequently shifted to optically thick, as the source continued to brighten in the radio. This motivated us to observe AT2019wey with the VLBA. We found a resolved source that we interpret to be a steady compact jet, a feature associated with black hole X-ray binary systems in hard X-ray spectral states. The jet power is comparable to the accretion-disk X-ray luminosity. Here, we summarize the results from these observations.

**4.1 Introduction**

Black hole X-ray binaries are comprised of stellar mass black holes accreting from companion stars. Most of the electromagnetic emission from these systems arises from accretion disks and relativistic jets, and strong coupling is observed between properties of the disks and jets. The presence of a jet is dependent on which X-ray spectral state the black hole binary is observed to be in. This phenomenon was first observed in the correlated X-ray and radio intensities of Cyg X-1 (Tanaka et al., 1972), where the X-ray emission was interpreted as originating from the disk, and the radio emission from the jet. The two main X-ray spectral states of interest are the thermal state (formerly known as the high/soft state) and the hard state (formerly known as the low/hard state). In the thermal state,  $> 75\%$  of the observed flux is contributed by the accretion disk. The predominantly thermal spectrum is accompanied by a steep power law extending to energies higher than  $\sim 10$  keV. In

---

<sup>1</sup>Cahill Center for Astronomy and Astrophysics, MC 249-17 California Institute of Technology, Pasadena CA 91125, USA

<sup>2</sup>National Radio Astronomy Observatory, Socorro, NM 87801, USA

the hard state the disk appears cooler and contributes very weakly, and  $> 80\%$  of the flux is contributed by a non-thermal power law spectrum with a photon index of  $1.4 < \Gamma < 2.1$ . For detailed reviews, see Fender, 2003, McClintock and Remillard, 2009, and Remillard and McClintock, 2006.

The first observation of a resolved jet in an X-ray binary was conducted with the Very Large Array (VLA) on SS 433 (Hjellming and Johnston, 1981). Subsequent observations of the X-ray binary systems GRS 1915+105 (Mirabel and Rodríguez, 1994) and GRO 1655 – 40 (Tingay et al., 1995), with the VLA and the Southern Hemisphere VLBI Experiment (SHEVE), respectively, revealed the first Galactic examples of superluminal motion of relativistic jet components. The ejection of superluminal components was linked to X-ray outbursts. In its hard ‘plateau’ X-ray state, however, GRS 1915+105 was observed to host a compact steady radio jet with mildly relativistic component velocities (Dhawan, Mirabel, and Rodriguez, 2000). Compact steady jets have also been observed in two other sources, Cyg X-1 (Stirling et al., 2001) and MAXIJ1836–194 (Russell et al., 2015), in canonical hard states. The link between the ejection of highly relativistic jet components and X-ray outbursts in the thermal state, first observed in GRS 1915+105 (Dhawan, Mirabel, and Rodriguez, 2000), established a causal link between the accretion rate and jet properties (Vadawale et al., 2003; Fender, Belloni, and Gallo, 2004).

Radio observations of the hard-state compact steady jets of GRS 1915+105 and Cyg X-1 that comfortably resolve the emission region were used to derive the jet powers and speeds (Dhawan, Mirabel, and Rodriguez, 2000; Stirling et al., 2001). These measurements are consistent with the model of conical synchrotron jets to describe radio emission from black hole accretors (Blandford and Königl, 1979; Hjellming and Johnston, 1988), and motivated the derivation of scaling relations between jet power and accretion disk luminosity (Falcke and Biermann, 1995; Falcke and Biermann, 1999). Adding to the handful of spatially resolved black hole X-ray binary jets in the hard state is critical towards refining physical models for disk/jet coupling.

### **The candidate black hole X-ray binary AT2019wey**

AT2019wey was first discovered as an optical transient by the Asteroid Terrestrial-impact Last Alert System (ATLAS) on December 7, 2019 (Tonry et al., 2019). A few months later on March 18, 2020, Spektrum-Roentgen-Gamma (SRG) discovered an X-ray source consistent with the position of the ATLAS detection and classified it as

a hostless transient or potential supernova (Mereminskiy et al., 2020), while Lyapin et al. (2020) suggested it may be a BL Lac type object. However, the discovery of hydrogen absorption lines with a redshift  $z = 0$  led Yao et al. (2020a) to posit a Galactic accreting binary origin.

Several physical constraints on AT2019wey were derived by Yao et al. (2020c) through a multi-wavelength follow-up campaign. The distance to AT2019wey was constrained to be between 1–10 kpc. The lower limit of 1 kpc was derived from the amount of observed extinction,  $0.8 \lesssim E(B - V) \lesssim 1.2$  mag, calculated from Na I D absorption lines in the optical spectrum. The Galactic anticenter sightline of AT2019wey led to an upper distance limit of 10 kpc. A combination of extinction measurements and historical optical observations at the location of AT2019wey also constrain the mass of the companion star to be  $\lesssim 0.8M_{\odot}$ . On August 2, 2020, VLA observations of AT2019wey revealed an optically thin spectrum from 1–12 GHz, which stood in contrast with the previous measurements of an optically thick spectrum on May 27, 2020 (Yao, Dong, and Kulkarni, 2020; Cao et al., 2020). Subsequent radio spectra taken on August 14, 21, and 28 showed a return to an optically thick spectrum; however, the flux density continued to increase. The compact object was determined to be a candidate black hole by comparing the radio and optical luminosities of the system to other known binaries with comparable X-ray luminosities. The radio and optical luminosities were found to be well above that expected for a neutron star accretor across the entire estimated distance range.

Yao et al. (2020b) present a detailed X-ray observational investigation of AT2019wey. X-ray observations from five telescopes – the Neutron Star Interior Composition Explorer (NICER), Nuclear Spectroscopic Telescope ARray (NuSTAR), the Chandra X-ray Observatory, the Neil Gehrels Swift Observatory, and the Monitor of All-sky X-ray Image (MAXI) – were used to monitor the flux and spectrum of the source. These data show that AT2019wey is in a hard state throughout its entire period of activity, although the spectrum softens between August 21, 2020 and September 28, 2020. The X-ray photon index is observed to steepen from  $1.7 < \Gamma < 2.0$  to  $2.0 < \Gamma < 2.3$ ; however, it is never seen to transition into a fully soft state. Additionally, using a model fit to the reflection spectrum observed by NICER and NuSTAR and paying close attention to the residuals around the Fe line, Yao et al. (2020b) infer that the inclination angle of the system must be  $i \lesssim 30^{\circ}$ .

We present observations of AT2019wey with the Very Long Baseline Array (VLBA) to attempt to resolve the rapidly evolving radio source. In section 4.2, we provide

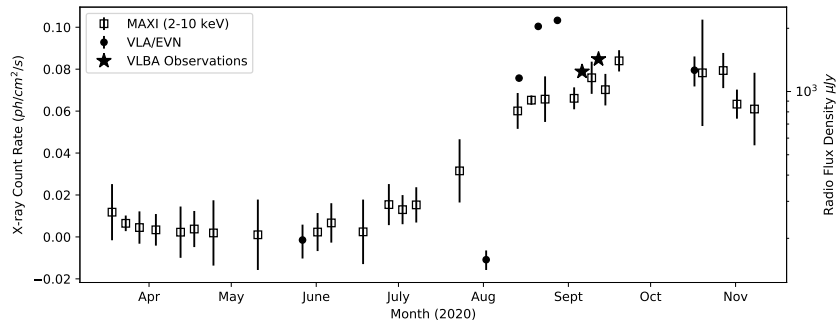


Figure 4.1: Lightcurves showing radio observations (scaled to 4.8 GHz) and X-ray observations from MAXI (2-10 keV). The stars on the plot show the observations discussed in this work.

details on our VLBA observation as well as our data analysis procedure and in section 4.3 we summarize the observed properties of AT2019wey. In section 4.4, we discuss parallels between AT2019wey and MAXIJ1836–194 and provides an analysis of the minimum energy and power of the system.

## 4.2 Observation and Analysis Procedures

Fig. 4.1 shows X-ray and radio light curves for AT2019wey. The X-ray data are taken by the Monitor of All-sky X-ray Image (MAXI) telescope in the 2-10 keV band (Matsuoka et al., 2009). The radio data point depicted on May 27 was taken with the VLA at 6.0 GHz while the observations between August 2 and August 28 were taken with the VLA at 3.5 GHz. These measurements were scaled to 4.8 GHz using the spectral indices published by Yao et al., 2020c. The radio data point shown on October 17 was taken by Giroletti et al., 2020 with the European VLBI Network (EVN) at 6.7 GHz; this point was scaled to 4.8 GHz on the light curve as well using the spectral index from Yao et al., 2020c on August 28.

The two epochs of observations of AT2019wey at 4.8 GHz were obtained with the VLBA on September 6 and September 12 and were processed with the DiFX correlator (Deller et al., 2011). Both three-hour epochs were phase referenced, with alternating scans of 3.5 minutes on AT2019wey and 40 seconds on the phase reference (J0418+5457). The phase reference is at an assumed location of  $RA = 04^h 18^m 19.3401920^s$  and  $Dec = 54^\circ 57' 15.334490''$ , an angular separation of  $2.47^\circ$  from the target, and was chosen because of its inclusion in the third realization of the International Celestial Reference Frame (ICRF3) (Charlot et al., 2020). Each epoch also contained 4-minute observations of a check source (J0427+5618), and 6-minute observations of a bandpass calibrator (J0555+3948).

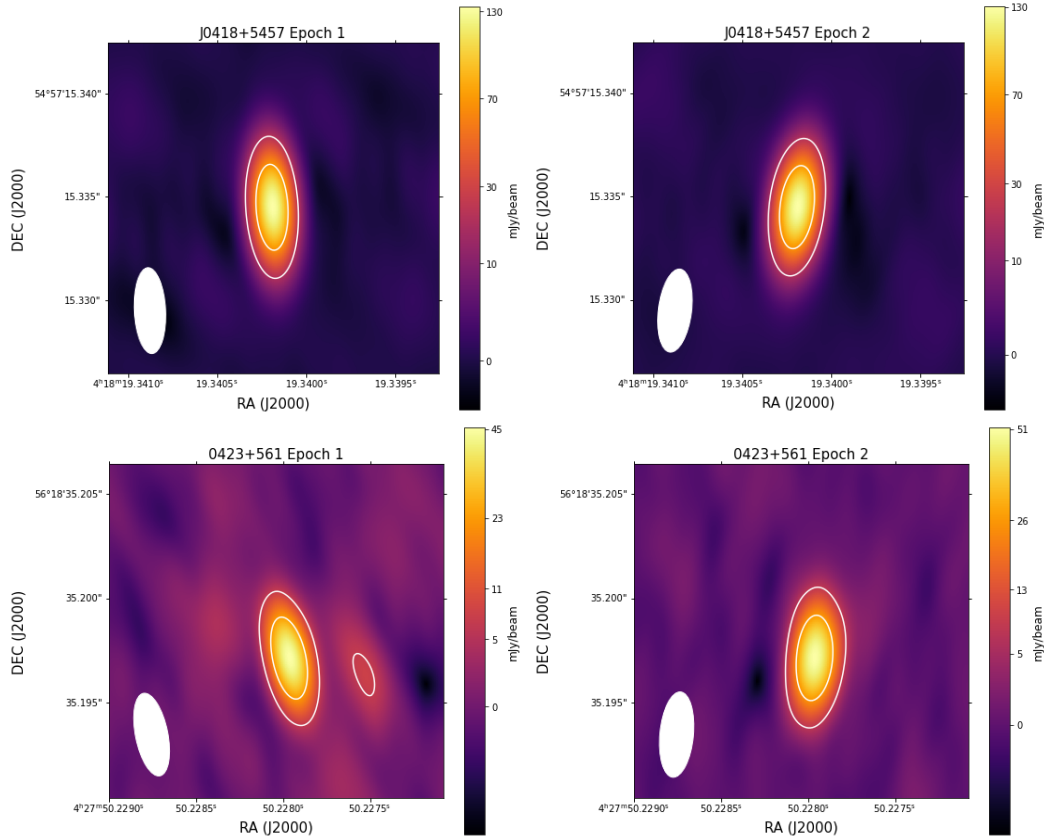


Figure 4.2: CLEAN images of the phase reference (top row), J0418+5457, and the check source (bottom row), 0423+561, for both epochs. The images are consistent with point sources. Also depicted on the images are 15% and 50% flux density contours.

Calibration and imaging for the observations were carried out in AIPS (Greisen, 2003) using standard procedures. To derive phase solutions, we performed global fringe fitting on the phase calibrator followed by two rounds of phase-only self-calibration and one round of amplitude+phase self-calibration. The self-calibration was done with two-minute solution intervals and assumed a point source model with the catalog flux density for the phase calibrator. Once phase variations of less than  $\pm 5^\circ$  were reached for all stations, the phase solutions were applied and no further self-calibration was performed on either the check source or AT2019wey. All images were created with natural weighting to maximize sensitivity. Images of the phase calibrator and check source are shown in Fig. 4.2 and images of AT2019wey are shown in Fig. 4.3. The full-width half maximum of the Gaussian model used to approximate the synthesized beam (shown in corners of the images) is approximately



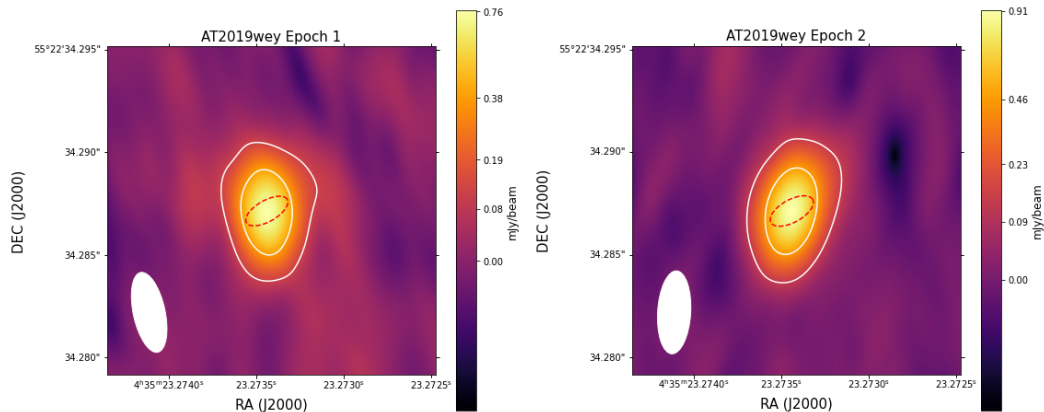


Figure 4.3: CLEAN images of AT2019wey for both epochs with 15% and 50% flux density contours. The red dotted line represents the single best fit deconvolved ellipse across both epochs for the source.

RA (J2000)	Dec (J2000)	Flux Density
$04^h 35^m 23.27345^s \pm 0.00028^s$	$55^\circ 22' 34.28715'' \pm 0.00017''$	$1.35 \pm 0.02$ mJy
Major Axis	Minor Axis	Position Angle
$2.13 \pm 0.10$ mas	$0.80 \pm 0.18$ mas	$122^\circ \pm 4^\circ$

Table 4.1: Properties for AT2019wey, approximating the source structure as a 2D Gaussian. Though this geometry does not reflect the true source structure, more complex features cannot be extracted from these observations.

a  $4 \text{ mas} \times 1.5 \text{ mas}$  ellipse in both epochs. The estimated deconvolved component for AT2019wey for each epoch is represented by the red dotted ellipse in Fig. 4.3.

### 4.3 Results

The images and uv-amplitudes of AT2019wey both show that the source is resolved. The images (Fig. 4.3) show a source that is clearly wider and oriented at a different position angle than the elliptical model of the synthesized beam. Plots of the uv-amplitudes, coherently averaged for 20 minute intervals, are shown in Fig. 4.4 along with uncertainties. The amplitudes are clearly not constant as a function of uv-distance, as would be expected for a point source.

We attempted to fit a 2-D Gaussian component to the visibilities using the `uvfit` task in AIPS; however, low signal to noise in individual visibility measurements yielded unreliable results for a 2-D Gaussian model fit to visibilities.

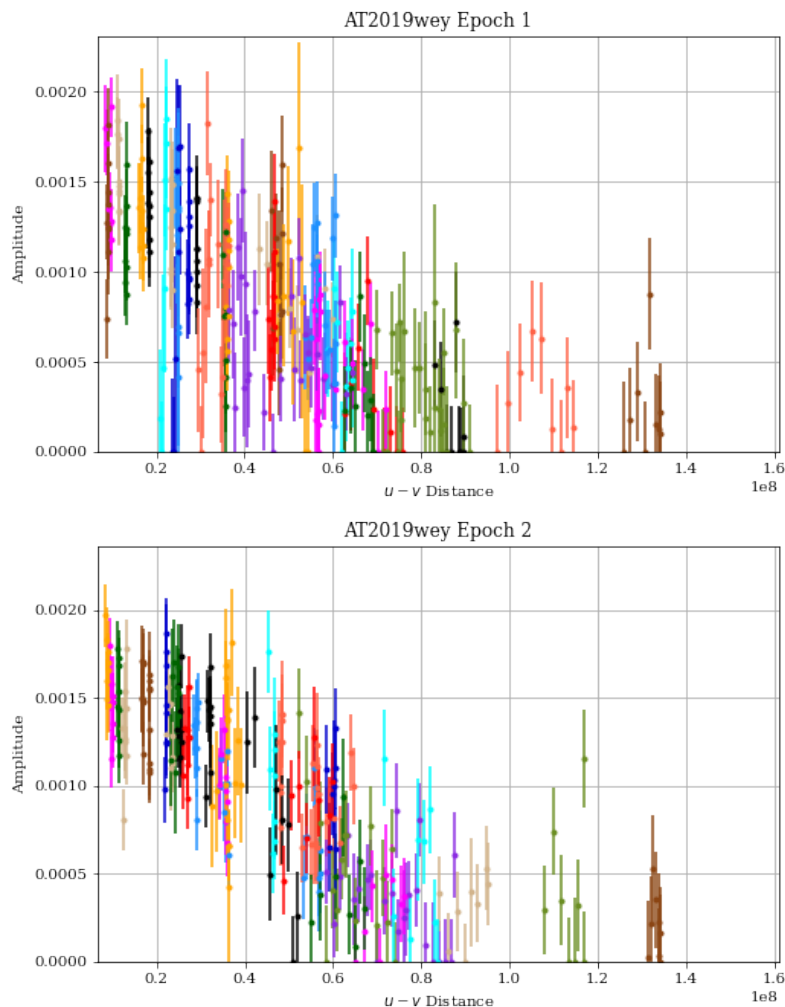


Figure 4.4: UV-amplitudes of AT2019wey for both epochs, with colored points representing different baseline pairs.

Instead, we performed an image plane fit using the AIPS task `jmfit`, which uses a least squares approach to fit a 2-D Gaussian component to the image and then deconvolves the CLEAN beam from the fitted component to estimate a 2-D Gaussian model for the true source geometry. The `jmfit` task also provides uncertainties for all of these parameters; however, the task will report the lower limits of the deconvolved major and minor axis as 0 mas if a reliable uncertainty cannot be derived. As we are confident that the source is resolved, in these cases we assume symmetric uncertainties based on the estimate of the upper limit for use in any calculations. To achieve convergence with the `jmfit` task, we fix the position of the 2-D Gaussian to the position of the phase center of the image. The errors on the RA

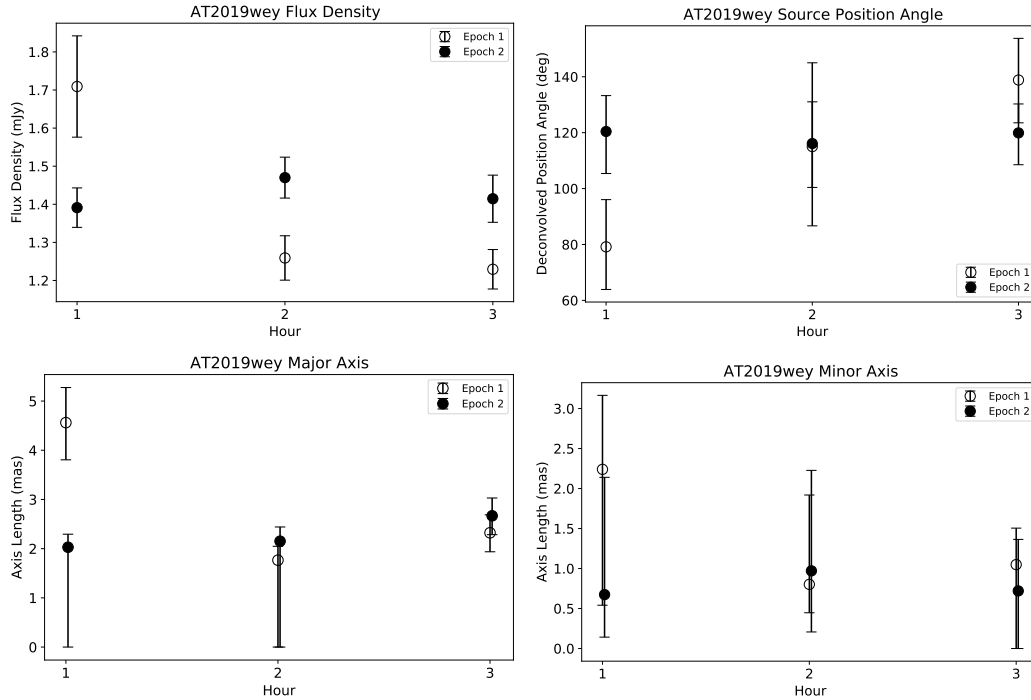


Figure 4.5: Model parameters derived for a Gaussian image plane fit to hour long observation blocks of AT2019wey. All of the geometric parameters are estimations of a deconvolved component. Top left: flux density, top right: position angle measured east of north, bottom left: major axis, bottom right: minor axis.

and Dec of the source position are then dominated by the cataloged position errors of the phase reference.

To investigate time variability in the phase calibrator and AT2019wey, we image and perform model fitting with `jmfit` for three hour-long blocks in each epoch. The fitted flux density, position angle reported east of north, the major axis, and the minor axis for each hour of both epoch are shown along with uncertainties in Fig. 4.5. The mean best fit values and uncertainties are summarized in Table 4.1. We see that AT2019wey has a flux density of  $1.35 \pm 0.02$  mJy and an approximated 2-D Gaussian geometry with a major and minor axis of  $2.13 \pm 0.10$  mas and  $0.80 \pm 0.18$  mas, respectively, at a position angle of  $122^\circ \pm 4^\circ$ . These values closely agree with those derived from performing a model fit on data combining the two epochs. Though the formal uncertainties on these parameters are small, this does not imply the true source geometry is well modeled by a Gaussian; however, subtracting this model from the visibilities and imaging the residuals reveals only noise, an indication that it would be difficult to extract more complex structure from this data. The model

does illustrate relatively stable source properties and facilitates a rough estimate of source power.

Although the source geometries of AT2019wey remain relatively consistent within the uncertainties across both epochs, there are some notable deviations. The best fit parameters are anomalous for the first hour of the first epoch. Inspection of the phase calibrator showed no significant phase or gain fluctuations during this time, indicating that the anomalous measurement is likely not caused by calibration error. As a light-crossing time of one hour is equivalent to a distance of several AU, a scale similar to the synthesized beam-width for low distance estimates, it cannot be ruled out that this measurement is due to true variability in the X-ray binary. The fitted flux density is also around 15% higher in the second epoch than the first. As the source is seen to be fading in the radio lightcurve presented in Yao et al., 2020c, we do not expect the second epoch to show significant increase in brightness. A similar level of variation is seen in the flux density of the check source, which was fitted to 45.6 mJy in epoch 1 compared to 54.9 mJy in epoch 2. This may indicate residual phase error in the first epoch leading to a lower flux density measurement, but intrinsic source variability on these small angular scales cannot be ruled out. The use of dynamical imaging and attempts to super-resolve the source, left to a later work, would provide a way to verify potential short timescale evolution.

#### 4.4 Discussion

A comparison of these VLBA observations of AT2019wey and observations taken of similar systems, specifically GRS 1915+105 and MAXIJ1836–194, provides compelling evidence that the radio source we observe is likely a steady compact jet. Compact radio sources were observed while both of these systems were in hard X-ray spectral states. Dhawan, Mirabel, and Rodriguez (2000) report a well-resolved, elongated radio source in GRS 1915+105 that exhibits a shallow radio spectral index,  $\alpha \lesssim 0.5$ , and a steady position angle over two years of observations. Although Russell et al. (2015) report only a marginally-resolved radio source in MAXIJ1836–194 with a steeper spectral index of  $\alpha \lesssim 0.8$ , the source also shows a stable position angle over two months of observations. The fact that AT2019wey was observed in the hard X-ray state with a nearly flat radio spectral index of  $\alpha \sim 0.2$  and the position angle of VLBA source remains stable between the two epochs of observation indicate the presence of compact steady jet.

The measurement of an angular size enables us to estimate the total energy in the source following standard synchrotron theory (following Pacholczyk, 1970). We assume an ellipsoidal structure for the source, with a projected shape corresponding to the 2-D Gaussian described above. At a fiducial distance of  $D = 3$  kpc, we adopt a source volume of  $V = 10^{42} \text{ cm}^{-3}$ . We assume a flat radio spectrum between 1–12 GHz only (spanning the VLA observations of AT2019wey), with a flux density of 1.35 mJy. The minimum energy required to power the synchrotron source (relativistic particles and magnetic fields) is then

$$E_{min} \approx 5 \times 10^{38} \left( \frac{D}{3 \text{ kpc}} \right)^{\frac{17}{7}} \left( \frac{V}{10^{42} \text{ cm}^3} \right)^{\frac{3}{7}} \text{ erg}. \quad (4.1)$$

The corresponding mean magnetic field strength is  $\sim 0.07$  G, implying a relativistic-lepton Lorentz factor of  $\gamma \approx 250$  for 12 GHz emission. Assuming a characteristic particle acceleration timescale corresponding to the light crossing time of the source of  $\sim 3 \times 10^3$  s at 3 kpc, the power dissipation in the source is approximately

$$P \gtrsim 2 \times 10^{35} \left( \frac{D}{3 \text{ kpc}} \right)^{\frac{10}{7}} \left( \frac{V}{10^{42} \text{ cm}^3} \right)^{\frac{3}{7}} \text{ erg s}^{-1}. \quad (4.2)$$

We emphasize that this is a lower limit given the limited band used to calculate the total radio luminosity, and the minimum-energy assumption.

The inferred power is remarkably close to the  $\sim 10^{36} \text{ erg s}^{-1}$  X-ray luminosity of AT2019wey found by Yao et al. (2020b) for a 3 kpc distance. The luminosity of the thermal emission from the disk is likely a few tens of percent of this total. This correspondance has been observed previously in the hard and plateau states of the GRS 1915+105 (e.g., Dhawan, Mirabel, and Rodriguez, 2000), and is a critical assumption of models for symbiotic disk-jet systems (Falcke and Biermann, 1999). Although we resolve the radio source in AT2019wey, we have no compelling morphological evidence for a jet. Nonetheless, the panchromatic properties of AT2019wey are closely similar to low-mass black hole X-ray binaries in which relativistic jets have been observed (Yao et al., 2020c). We therefore interpret the resolved source as a compact steady jet, with a power that is comparable to the accretion-disk X-ray luminosity.

## 4.5 Conclusion

We present here two epochs of 4.8 GHz VLBA observations of candidate black hole low-mass X-ray binary system AT2019wey following a period of X-ray and radio brightening. The observations revealed a resolved source with deconvolved

source geometries that are relatively constant across both epochs. Together with the observed X-ray spectrum, we interpret these results to indicate the presence of a compact, steady jet. Using the angular scale derived from image plane fits of a 2-D Gaussian component to the source, we show that the power dissipation from the jet is comparable to the X-ray luminosity, consistent with a standard assumption of models for disk/jet coupling.

Thus far, spatially resolved compact jets in X-ray binaries in the hard spectral state have only been observed for five systems, including AT2019wey. The next-generation Very Large Array (ngVLA) and the Square Kilometre Array (SKA) are ideal instruments to expand on this limited sample (Fender et al., 2015; Maccarone et al., 2018). With their combination of long baselines and extreme sensitivity, the ngVLA and SKA will enable high-cadence monitoring of the flux densities and multi-scale morphologies of an extended sample of X-ray binaries. The ngVLA may in fact prove to be a discovery engine for accretion Galactic black holes through astrometric surveys (Maccarone et al., 2019). Observations of these systems during a variety of states and state transitions are required to broaden our understanding of the connections between accretion states and jets.

### **Acknowledgements**

We thank Tim Pearson, Gregg Hallinan, and Katie Bouman for useful discussions on interpreting these results. These observations were conducted with the Very Long Baseline Array. The National Radio Astronomy Observatory is a facility of the National Science Foundation operated under cooperative agreement by Associated Universities, Inc. This research has made use of NASA's Astrophysics Data System.

## Chapter 5

### IMAGING THE SUPERMASSIVE BLACK HOLE IN M87 WITH 2018 EVENT HORIZON TELESCOPE OBSERVATIONS

*This chapter is adapted from a 2023 paper in preparation by the Event Horizon Telescope Collaboration, with greater emphasis placed on my role in generating synthetic data and developing an imaging pipeline using the software `eht-imaging`. Related material from other sections of the paper is added for necessary context.*

#### 5.1 Introduction

##### Fundamental Physics of Black Holes

Black holes were first theorized to exist through solutions to Einstein's theory of general relativity. They represent regions of spacetime where nothing can escape them, including light. This boundary of "no escape" from a black hole was first solved by Karl Schwarzschild in 1916 (Schwarzschild, 1916), and is now known as the Schwarzschild radius,  $R_s = 2r_g$  (where  $r_g = GM/c^2$ ). This later came to be updated by the Kerr metric, which describes black holes with angular momentum (Kerr, 1963). The last visible surface of a black hole is known as the innermost stable circular orbit (ISCO) or photon capture radius of the black hole. For a Schwarzschild black hole, this value is  $R_c = \sqrt{27}r_g$ . Photons passing within this radius will eventually spiral inwards towards the event horizon whereas photons passing at radii greater than  $R_c$  may escape (Hilbert, 1917). This creates a bright, thin circular feature known as a photon ring as well as a central, dark region known as the black hole shadow. Bardeen, 1973 further describes the noncircularity of the photon ring for spinning black holes and Luminet, 1979 details simulations of the appearance of black hole event horizons to viewers, including the effects of the presence of an accretion disk. The simulations showed that the photon ring is embedded within a thicker, non-uniform, asymmetric ring of emission from the accretion disk. The exact structure of the accretion disk emission is shown to be dependent upon the viewing angle of the observer relative to the disk. As imaging resolution in interferometry improves with increasing baseline length and observing frequency, global-scale millimeter very long baseline interferometry (VLBI) provides the best opportunity for imaging the shadow of a black hole (Falcke, Melia, and Agol, 2000). Comparing high resolution images of black holes with theoretical predictions can

be used to verify original theories of general relativity and unveil the mechanisms of accretion and jet launching in supermassive black holes.

Black hole accretion is divided into two models: Standard and Normal Evolution (known as SANE models; Narayan et al., 2012; Sądowski et al., 2013) or Magnetically Arrested Disk (known as MAD models; Igumenshchev, Narayan, and Abramowicz, 2003; Narayan, Igumenshchev, and Abramowicz, 2003). These models are differentiated by the amount of magnetic flux around the event horizons of black holes. The MAD model suggests that strong magnetic fields near the event horizon resist the infall of surrounding gas, leading to radiatively efficient blobs or streams of accretion rather than axisymmetric accretion. The SANE model on the other hand suggests weak magnetic fields near the event horizon and the transportation of accreting material is largely affected by turbulence invoked by magnetorotational instability throughout the disk. Both models can achieve similar total mass-accretion rates and the dominant mode of accretion into black holes remains an open question.

A similar dichotomy exists for jet formation in black holes. Several black holes are seen to launch relativistic jets, on scales from stellar masses (see review in Mirabel and Rodríguez, 1999) to supermassive black holes (see review in Blandford, Meier, and Readhead, 2019). These jets are believed to be launched along magnetic field, but whether the energy is extracted from the angular momentum of a spinning black hole (Blandford and Znajek, 1977) or from winds originating in the accretion disk (Blandford and Payne, 1982) is yet to be settled. Resolved imaging of the base of jet-launching regions has the power to discern between the two models.

As VLBI is bounded at present by a baseline distance of the earth's diameter, the two most promising sources for which the predicted event horizons could be resolved are the black hole at the center of the Milky Way, Sagittarius A\* (Sgr A\*) as well as the one at the center of the galaxy M87, M87\*. Early experiments such as Krichbaum et al., 1998 and Doeleman et al., 2001 use millimeter observations on three baselines to show resolved structure in Sgr A\*. Longer baseline experiments such as Doeleman et al., 2008 and Doeleman et al., 2012 proved the existence of event horizon scale structure in both Sgr A\* and the black hole at the center of the galaxy M87 (M87\*). However, moving beyond basic visibility domain analysis to imaging could only be achieved by increasing the number of available baselines.



### The SMBH in M87

A jet coming from the nearby galaxy M87 was first discovered with optical observations at Lick Observatory, accompanied by a description of an exceedingly bright "curious straight ray" originating from a central nucleus (Curtis, 1918). The first resolved radio detections of this jet were conducted many years later with the Very Large Array (Kassim et al., 1993). It was not until the 90s, however, that optical spectroscopy of the gas disk revealed that the center of M87 contained a supermassive black hole (SMBH) which served as the origin of the jet (Harms et al., 1994; Macchetto et al., 1997) with a mass of  $\sim 3.5 \times 10^9 M_{\odot}$ . Later measurements of stellar kinematics suggested a higher mass of  $\sim 6.7 \times 10^9 M_{\odot}$  (Gebhardt and Thomas, 2009; Gebhardt et al., 2011).

Estimates of M87\*'s mass and distance ( $\sim 16.8$  Mpc Blakeslee et al., 2009; Bird et al., 2010; Cantiello et al., 2018) give it a theoretical shadow radius of  $\sim 21 - 38 \mu\text{as}$ , making it a prime candidate for high resolution imaging. In addition to horizon scale imaging, several VLBI experiments have resolved and monitored the M87 jet and carried out measurements of its speed, inclination angle, and orientation (e.g., Reid et al., 1989; Walker et al., 2018), all of which can be used to more accurately predict the shape of the emission surrounding the black hole shadow. Astrometric measurements of the core of M87 as a function of frequency further revealed that observations at millimeter wavelengths would be key to measuring the region of jet launching. This strong potential for making fundamental measurements about black holes is what motivated observations of M87\* by the Event Horizon Telescope (EHT; Event Horizon Telescope Collaboration et al., 2019a).

## 5.2 Description of Observations

### Utility of Closure Quantities in VLBI

The EHT is a global millimeter VLBI experiment that aims to create images of the event horizons of SMBHs (full description of instrument in Event Horizon Telescope Collaboration et al., 2019b). Observations are taken at  $\sim 1.3$  mm or 230 GHz and are comprised of complex visibilities. These visibilities are correlated signals between baselines and contain information about both the amplitude and phase. Each baseline probes brightness at a different spatial scale across the sky and the distribution of measured spatial scales is known as the  $(u, v)$ -plane or the visibility domain. Idealized visibilities (ones barring any instrumental or atmospheric effects),  $V(u, v)$ , on the  $(u, v)$ -plane are related by Fourier transform to the true sky brightness,  $I(x, y)$ , according to the van Cittert-Zernike theorem.

$$V(u, v) = \int \int e^{-2\pi i(ux+vy)} I(x, y) dx dy \quad (5.1)$$

For a given baseline with antennas labelled  $i$  and  $j$ , the idealized measured visibility can be written as follows, where  $A_{i,j}$  is the true visibility amplitude and  $\varphi_{i,j}$  is the true visibility phase.

$$V_{i,j} = A_{i,j} e^{i\varphi_{i,j}} \quad (5.2)$$

In reality, however, this visibility measurement suffers from sensitivity loss due to systematic errors affecting both the amplitudes and phases. Taking into account antenna-dependent complex gain variations, the measured visibility across antennas labelled  $i$  and  $j$  is actually

$$V'_{i,j} = g_i g_j^* V_{i,j} = a_i e^{i\phi_i} a_j e^{-i\phi_j} A_{i,j} e^{i\varphi_{i,j}} \quad (5.3)$$

Combinations of visibility measurements across multiple baselines can yield quantities that are independent of systematic errors. Following the work of Jennison, 1958, measurements along three baselines can yield error-independent phase quantities, known as closure phases, as such

$$\begin{aligned} \arg(V'_{i,j} V'_{j,k} V'_{k,i}) \\ = (\phi_i - \phi_j + \varphi_{i,j}) + (\phi_j - \phi_k + \varphi_{j,k}) + (\phi_k - \phi_i + \varphi_{k,i}) \\ = \varphi_{i,j} + \varphi_{j,k} + \varphi_{k,i} \end{aligned} \quad (5.4)$$

Similarly, error-independent amplitude quantities, known as closure amplitudes, can be derived from sets of four visibilities as such

$$\frac{|V'_{i,j}| |V'_{k,l}|}{|V'_{i,k}| |V'_{j,l}|} = \frac{(a_i a_j A_{i,j})(a_k a_l A_{k,l})}{(a_i a_k A_{i,k})(a_j a_l A_{j,l})} = \frac{A_{i,j} A_{k,l}}{A_{i,k} A_{j,l}} \quad (5.5)$$

For an  $N$ -element interferometer,  $(N-1)(N-2)/2$  unique closure phase quantities can be constructed and  $N(N-3)/2$  unique closure amplitudes can be constructed. Closure quantities are useful in millimeter VLBI where phase stability can be challenging and especially useful for high resolution measurements where phase calibrator scans cannot be used to derive absolute phase information.

### Measurements from EHT 2017 Observing Campaign

In 2017, M87\* was observed on April 5, 6, 10, and 11 using seven stations: phased Atacama Large Millimeter/submillimeter Array (ALMA), phased Submillimeter Array (SMA), Atacama Pathfinder Experiment (APEX), IRAM 30-m telescope (PV), Large Millimeter Telescope Alfonso Serrano (LMT), Submillimeter Telescope (SMT), and the James Clerk Maxwell Telescope (JCMT). The longest baseline on the array achieved a diffraction-limited resolution of around  $25 \mu\text{as}$ . The backend supported recording two 2 GHz bands centered at 227.1 and 229.1 GHz, for which correlations were done independently at the MIT Haystack Observatory and the Max-Planck-Institut für Radioastronomie. Fringe fitting and other initial calibrations are handled with two independent custom pipelines, EHT-HOPS (Blackburn et al., 2019) and a CASA-based pipeline (Janssen et al., 2019), written for EHT data (Event Horizon Telescope Collaboration et al., 2019c).

Imaging of the data was performed with four independent methods, all of which showed significant detections of a shadow feature with a diameter of  $\sim 40 \mu\text{as}$  and an asymmetric thick ring of bright emission oriented towards the southern part of the image (Event Horizon Telescope Collaboration et al., 2019d). Marginally significant amounts of variability were detected between subsequent days of observation (discussed further in Satpathy et al., 2022). Utilizing 2017 observations as well as past observations with fewer baselines, Wielgus et al., 2020 assume consistent ring-like structure and employ visibility model-fitting to investigate the evolution of M87\*'s morphology over many years. Resolving questions around source evolution on short and long timescales motivated further observations of M87\* in subsequent years.

### Improvements with EHT 2018 Observing Campaign

The EHT conducted improved observations of M87\* in 2018 on April 21, 22, 25, and 28 with an expanded array due to the participation of the Greenland Telescope (GLT; Inoue et al., 2014), faster data recording compared to 2017, as well as two additional 2 GHz bands at 213.1 and 215.1 GHz for all sites except GLT. As shown in Figure 5.1, the addition of the GLT provides a significant improvement to the  $(u, v)$ -coverage over 2017. Importantly, the Chile-GLT baseline provides improved angular resolution in the north-south direction which stands to provide a better measurement of the brightness asymmetry of the ring. Additionally, it can be seen in Figure 5.2 that the PV-GLT baseline provides a useful probe of the first null in the visibility amplitudes of M87\*. Especially in conjunction with baselines at similar

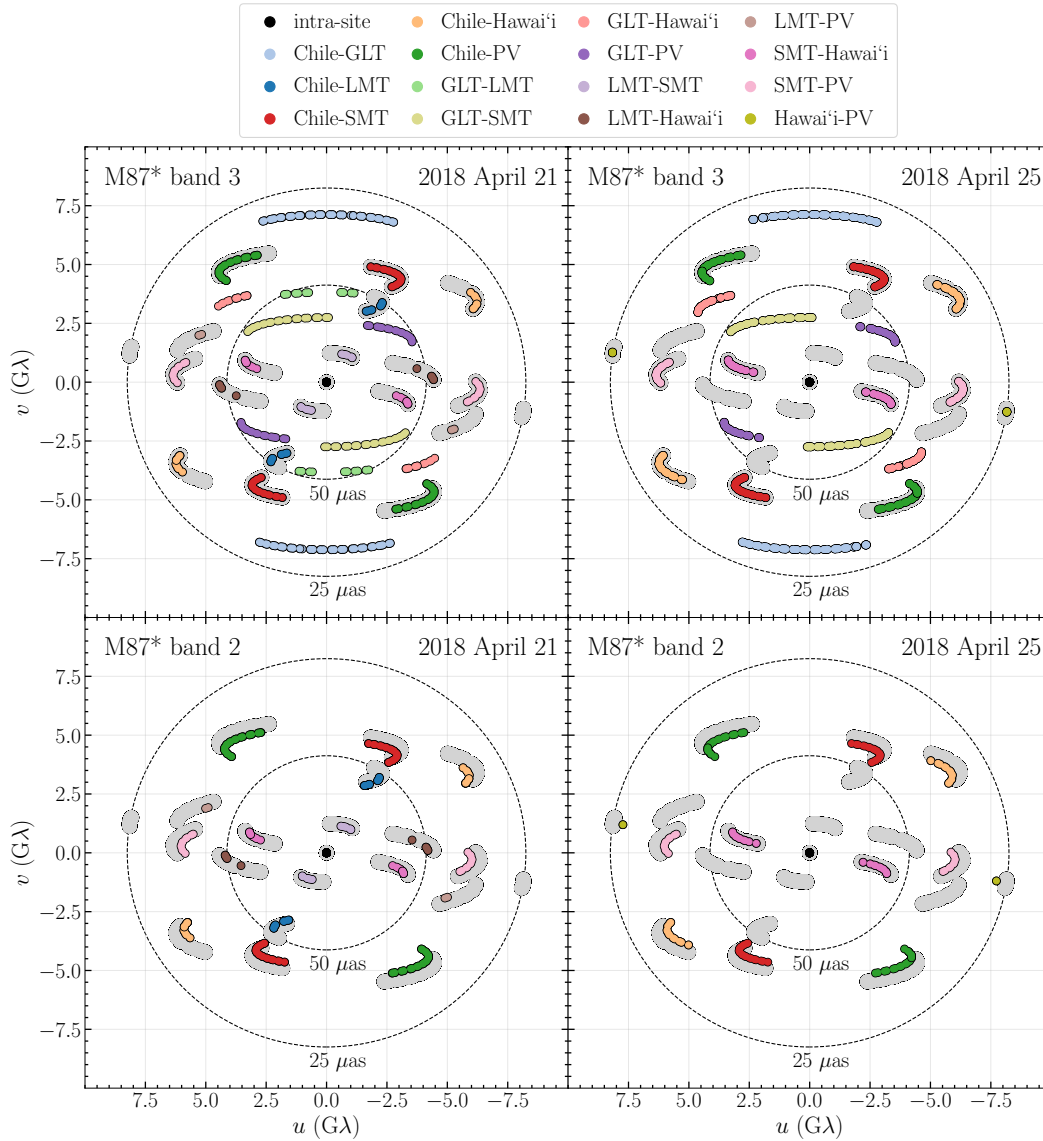


Figure 5.1: The  $(u, v)$ -coverage of the EHT observations of M87\* for days 2018 April 21 and 2018 April 25. The colored points represent 2018 observations while the light grey points represent  $(u, v)$ -coverage of the 2017 April 11 observations. Bands 3 and 2 are shown to visualize the impact of the GLT baselines.

$(u, v)$ -distances but orthogonal orientations, such as GLT-LMT and Chile-LMT, these data provide strong evidence in support of asymmetric source structure.

### 5.3 Pre-Imaging Analysis

#### Pre-Imaging Constraints

Before the application of any imaging techniques, constraints on the recovered image must first be derived from the data. The M87\* observations contain contributions

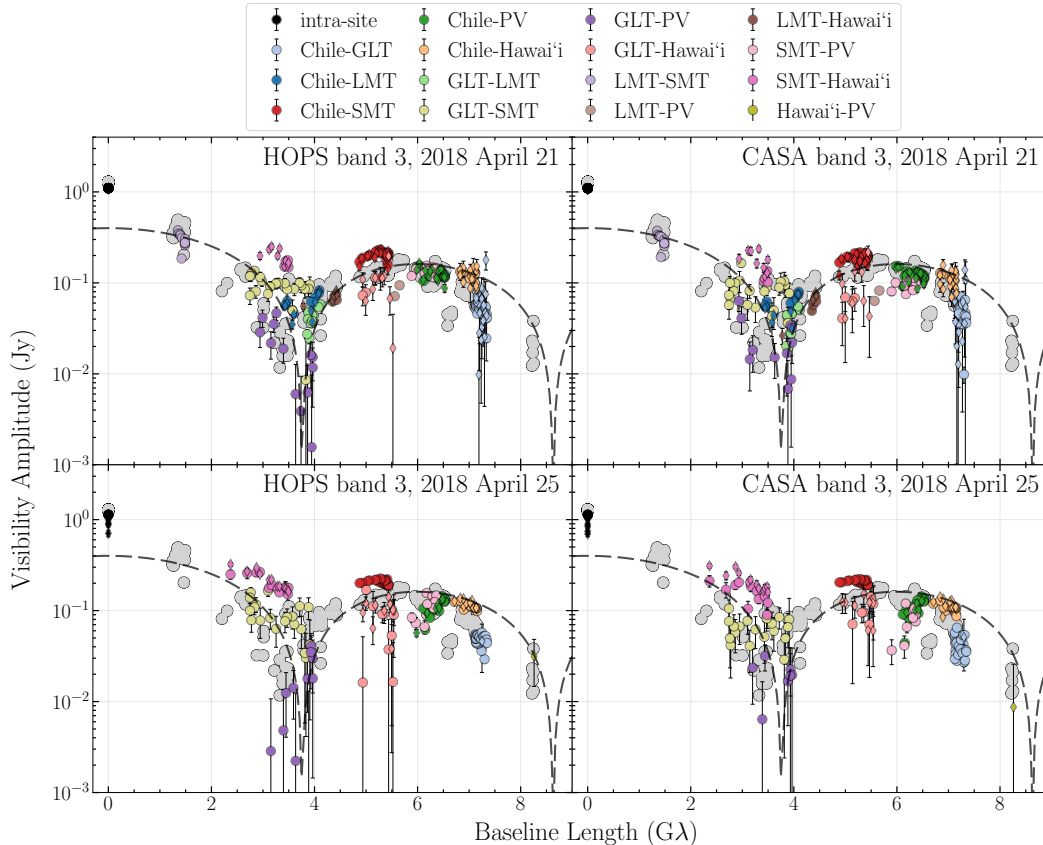


Figure 5.2: The visibility amplitudes of the M87\* observations as a function of  $(u, v)$ -distance. We show results from band 3 on both 2018 April 21 and 2018 April 25 using data from two calibration pipelines, with error bars to signify  $\pm 1\sigma$  uncertainty. The light grey points represent amplitudes measured on 2017 April 11 while the black dashed line represents model visibility amplitudes for a symmetric thin ring with diameter equal to  $42 \mu\text{as}$ .

of flux from two components: a compact component that encapsulates flux emitted near the black hole and a larger-scale, unresolved component contributed by the M87 jet. The imaging will only target source structure of the compact component, so estimates of its flux and size are necessary to inform priors on flux and field of view (FOV) choices.

A full description of this analysis is given in Appendix B of Event Horizon Telescope Collaboration et al., 2019d. In short, these constraints are derived from the assumption that the intra-site baselines (ALMA-APEX and JMCT-SMA) are sensitive to the large-scale flux while the inter-site baselines are sensitive to the compact flux. Thus, using the shortest inter-site baseline can provide limits on the source properties. By assuming that the visibility shape resembles a Gaussian for the shortest

baselines and that the gain errors at anchor stations ALMA and SMT are very small, we utilize the ratio  $|V_{SMT-LMT}|/|V_{ALMA-LMT}|$  to derive a lower limit of  $39 \mu\text{as}$  for compact source size and  $0.3 \text{ Jy}$  compact flux. Fitting the ratio between the intra-site baselines and the SMT-LMT baseline to a Gaussian model yields an upper limit of  $98 \mu\text{as}$  for the compact source and sets a maximum compact flux of  $1.13 \text{ Jy}$ . These properties are then considered when generating synthetic data to be used as training sets for the imaging procedure down the line.

### Synthetic Data Generation

As will be described further in upcoming sections, creating images from observations with sparse  $(u, v)$ -coverage requires making both assumptions about the source structure and assumptions about the required imaging parameters. To test the efficacy of imaging parameters used for each imaging method, we generate a set of four synthetic training data to select best performing sets of imaging parameters as well as a set of seven synthetic validation data. These data are created from geometrical models meant to emulate the properties of EHT M87\* visibility amplitudes, including prominent amplitude nulls, but also to reflect a diversity of both ring and non-ring source structures with the goal of not introducing bias into the selected imaging parameters.

The four geometric models used in the training set are very similar to those used in Event Horizon Telescope Collaboration et al., 2019d and are as follows. Ground-truth images of these models as well as their visibility amplitude structures are shown in the top two panels of Fig. 5.5.

1. **cres180**: An asymmetric ring model with  $r_0 = 23 \mu\text{as}$ , a brightness position angle oriented south, and blurred by a circular Gaussian beam of FWHM  $10 \mu\text{as}$ .
2. **ring**: A thin uniform ring of radius  $r_0 = 23 \mu\text{as}$  blurred by a circular Gaussian beam of FWHM  $10 \mu\text{as}$ .
3. **dbrsrc**: Two circular Gaussian components each with FWHM of  $20 \mu\text{as}$ . One is located at the origin with a flux density of  $0.27 \text{ Jy}$ , while the second is positioned at  $\Delta_{\text{R.A.}} = 30 \mu\text{as}$  and  $\Delta_{\text{decl.}} = -12 \mu\text{as}$  with a flux density of  $0.33 \text{ Jy}$ .
4. **disk**: A uniform disk of radius  $r_0 = 35 \mu\text{as}$  blurred by a circular Gaussian beam of FWHM  $10 \mu\text{as}$ .

The seven geometric models used as validation data are described below. Some of these models were created using direct fits to the EHT M87\* visibilities, making them more appropriate for use as validation rather than training data. Ground-truth images of these models as well as their visibility amplitude structures are shown in the top two panels of Fig. 5.6.

1. Three asymmetric ring models with  $r_0 = 23 \mu\text{as}$ , a brightness position angles oriented east, north, and west, blurred by a circular Gaussian beam of FWHM =  $10 \mu\text{as}$ .
2. A uniform elliptical disk model with a major axis of  $66 \mu\text{as}$ , a minor to major axis ratio of 0.65, a major axis position angle of 60 degree, and a blurring of  $10 \mu\text{as}$ .
3. A point source plus symmetric disk model containing a  $10 \mu\text{as}$  point source centered in  $100 \mu\text{as}$  diameter disk. The point source to disk flux ratio is chosen to be 0.192.
4. A point source plus elliptical disk model containing a  $10 \mu\text{as}$  point source centered in an ellipse of major axis of  $96 \mu\text{as}$ , a minor to major axis ratio of 0.8, a major axis position angle of 60deg, and a blurring of  $10 \mu\text{as}$ . The point source to disk flux ratio is 0.16.
5. A snapshot from a general relativistic magnetohydrodynamic (GRMHD) simulation of M87.

The ground truth images and synthetic visibilities were both generated using python package `eht-imaging` (Chael et al., 2018). All of the models described above contain 0.6 Jy in the compact source component and then an additional 0.5 Jy in a larger extended jet modelled by three Gaussians, parametrized in Table 5.1. This jet model was derived from images of the M87 jet taken at 3.5 mm (Kim et al., 2018). A depiction of this large scale jet model is shown in Figure 5.3. In order to accommodate the large scale jet, the full ground truth image is created with 2000 pixels and a  $3000 \mu\text{as}$  FOV. Following the procedure in Event Horizon Telescope Collaboration et al., 2019d, we add systematic polarization leakage terms to each component in the ground truth image. We add 40% fractional polarization with a coherence length of  $5 \mu\text{as}$  to the compact component and 20% fractional polarization with a coherence length of  $400 \mu\text{as}$ .

Flux Density (Jy)	$\theta_{\text{maj}}$ ( $\mu\text{as}$ )	$\theta_{\text{min}}$ ( $\mu\text{as}$ )	P.A. ( $^\circ$ )	$\Delta_{\text{R.A.}}$ ( $\mu\text{as}$ )	$\Delta_{\text{Dec}}$ ( $\mu\text{as}$ )
0.25	1000	600	104	-688.77	80.86
0.167	400	200	93	-295.44	-52.09
0.083	400	200	115	-215.80	-208.40

Table 5.1: Parameters of three Gaussians used to simulate the presence of a large scale jet in EHT 2018 synthetic datasets.

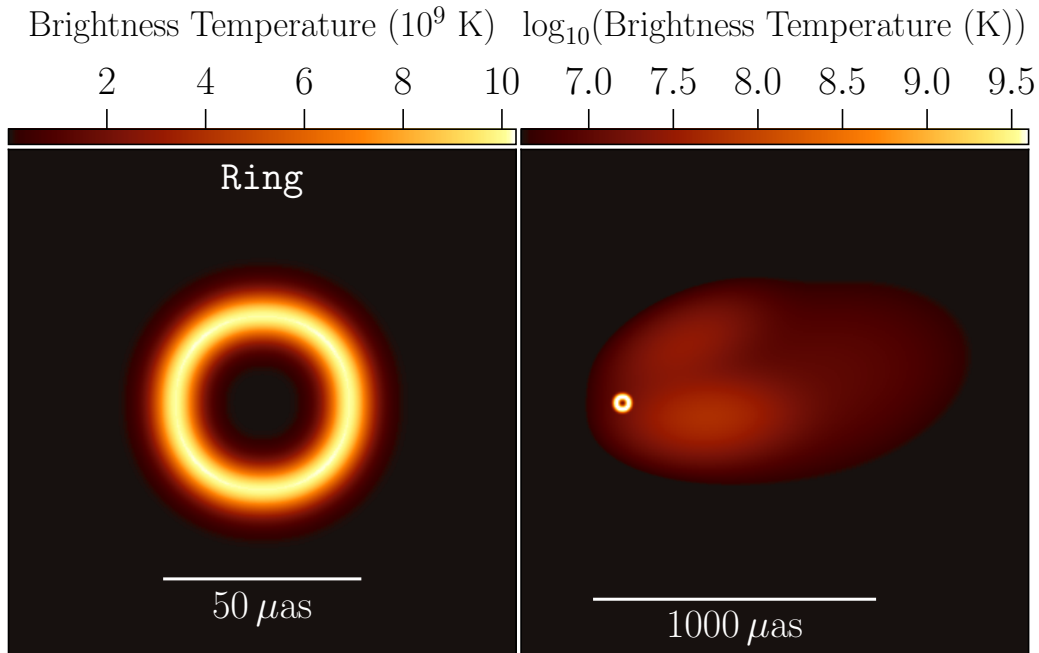


Figure 5.3: Ground truth image of geometric ring model utilized in synthetic training data. The left panel depicts a field of view (FOV) of  $130 \mu\text{as}$ , showing only the compact structure of the synthetic data. The right panel depicts a logarithmic-scale representation of the extended jet feature (FOV =  $2900 \mu\text{as}$ ) added to all of the synthetic data sets, visualizing the scale of the extended jet in relation to the compact source.

After making the ground truth image, we measure model visibilities using the same  $(u, v)$ -coverage as recorded in the 2018 M87\* observations and perturb them with thermal, gain, polarization, and field rotation errors. Random thermal errors are added per baseline based off of the system equivalent flux densities (SEFDs) of each station in the baseline. The rest of the errors are station dependent. Their values are combined to generate a station dependent error matrix, known as a Jones matrix, that is multiplied with the visibilities to simulate the necessary errors. Gain amplitude errors for each station contain both a fixed offset term,  $g_{\text{offset}}$ , and a scan by



Station Name	ALMA	APEX	GLT	LMT	SMT	JCMT	PV	SMA
$g_{\text{offset}}$	0.15	0.15	0.5	0.3	0.15	0.15	0.2	0.15
$g_{\text{p}}$	0.1	0.1	0.15	0.3	0.1	0.1	0.1	0.1

Table 5.2: Gain perturbation values for each station for the 2018 EHT M87\* observations.

scan varying term,  $g_{\text{p}}$ . The term  $g_{\text{offset}}$  is chosen once for each station by choosing a random number from a zero-mean Gaussian distribution with a standard deviation of  $\sigma_{g_{\text{offset}}}$ . The varying term  $g_{\text{p}}$  is similarly chosen once per scan by choosing a random number from a zero-mean Gaussian distribution with a standard deviation of  $\sigma_{g_{\text{p}}}$ . These values are shown in Table 5.2 and are calculated during the data calibration procedures using elevation-dependent gain measurements for each station. It should be noted that sub-optimal sensitivity of the LMT and incomplete characterization of the GLT have driven up the gain uncertainties relative to other stations. Gain phase errors are drawn from a uniform distribution once per scan. For polarization, we add 5% uncertainty for the D-terms, which quantify imperfections in the receiving feeds, and allow corrections for field rotation, which are based on the receiver mount type at each station. As a final step, we network calibrate the generated visibilities, as is done to the real M87\* visibilities. Network calibration is a procedure that uses baselines between co-located sites (for the EHT, these are SMT-JCMT and ALMA-APEX) and baselines between those and a third distant site to derive estimates of the station gains for the two co-located sites. This is described in detail in Section 6.2 of Event Horizon Telescope Collaboration et al., 2019c and assumes a zero-baseline flux density to fix the intrasite baseline visibility amplitude values to.

#### 5.4 Imaging Using Regularized Maximum Likelihood

Using measured visibilities to infer the true sky brightness that produced them is an example of an inverse problem. This problem is complicated by the EHT’s sparse  $(u, v)$ -coverage, which leaves us with incomplete information about certain spatial scales and directions of the true emission pattern. Thus, recovery of a single unique image from the measurements is impossible and sophisticated imaging algorithms that impose additional constraints and assumptions are required to reconstruct sets of well-fitting images. The EHT utilizes several imaging methods to verify the consistency of the reconstructed images.

Historically, radio interferometry has mainly utilized an imaging method known as CLEAN (Högbom, 1974), and the EHT uses an implementation of it in the program

DIFMAP (Shepherd, Pearson, and Taylor, 1994). The basic principle of CLEAN is to assume that the true sky brightness distribution can be modelled as a set of point sources. The algorithm starts with a 2-D Fourier transform of the visibilities and iteratively deconvolves the interferometer’s point source response function (known colloquially as the beam) from the image. The locations of the assumed point sources are convolved with a Gaussian approximation of the beam and added to a residual uncertainty map to produce a final image. This process is suboptimal for producing smoothly varying features, however, and is inherently limited by the width of the beam.

The EHT additionally utilizes forward modelling approaches for image reconstructions. Diverging from the deconvolution approach, these methods aim to create images that best match the measured visibilities by iteratively updating the brightness of individual image pixels. Different versions of forward modelling techniques exist for radio astronomy (see review in Narayan and Nityananda, 1986) but have never been used widely. The two types of forward modelling approaches used in the EHT are regularized maximum likelihood (RML), implemented in programs `eht-imaging` (Chael et al., 2018) and `SMILI` (Akiyama et al., 2017), and full posterior exploration with Bayesian sampling, implemented in `THEMIS` (Broderick et al., 2020) and `Comrade` (Tiede, 2022).

The rest of this chapter will mainly focus on work related to imaging with RML method `eht-imaging`, but will also show results from other methods for context.

### Imaging Strategy

The general approach to regularized maximum likelihood is to minimize an objective function that contains terms related to the data,  $\chi_D$ ; the weights placed on the data terms,  $\alpha_D$ ; terms related to assumptions about the data,  $S_R$ , known as regularizers; and the relative weights of those assumptions,  $\beta_R$  known as regularizer weights. The role of the regularizers is to prevent overfitting in the presence of sparse data. Increasing the regularizer weights more strongly enforces the conditions set by those particular regularizers.

$$J(I) = \sum_{\text{data terms}} \alpha_D \chi_D^2(I) - \sum_{\text{regularizers}} \beta_R S_R(I) \quad (5.6)$$

Though there exists a plethora of regularizer choices available, the five used with `eht-imaging` are:

1. *Total Flux Density*: favors images for which the sum of the pixels contains a flux density close to a specified value.
2. *Relative Entropy*: favors images that are similar to a prior image, measured by pixel-to-pixel similarity.
3.  *$l_1$  Norm*: favors image sparsity, meaning it prefers images where more of the pixels have a value of zero rather than a noisy mix of positive and negative values.
4. *Total Variation*: favors images with uniform regions of flux separated by sharp edges.
5. *Total Squared Variation*: favors smoothly varying images.

The data weight terms are present to reflect our relative confidence in different data products. The data products available to us are complex visibilities, visibility amplitudes, closure phases, and log closure amplitudes. As will be discussed shortly, we never place a high amount of confidence in complex visibilities, for example, due to the inability of millimeter VLBI to ever accurately measure true visibility phase. There does not exist a unique optimal set of data weights and regularizer weights, which we collectively refer to as "hyperparameters." Thus, to proceed, we conduct a grid search over a range of values for each hyperparameter to build a set of well-fitting images.

The goal of the parameter survey is to explore the impact of different imaging assumptions, including hyperparameters as well as optimization choices, on the resulting image morphology. We survey over each of the regularizer weights as well as over the amount of compact flux density, additional systematic noise, and the full width half maximum (FWHM) of the Gaussian used for the prior and initial image. The compact flux density value is also used to set the flux of the Gaussian and is used for enforcing the total flux density regularizer. The range of values surveyed for each hyperparameter is shown in Table 5.3. The range of surveyed compact flux density values was chosen based on the pre-imaging constraints outlined in Sect. 5.3, while the range of surveyed regularizer weights was chosen based on experience from values surveyed in Event Horizon Telescope Collaboration et al., 2019d.

From these surveys, we select a "Top Set" of parameter combinations for each imaging method, which represents the set of best-fit images to the data. For each parameter combination, we first generate images of each of the four training sets. For

each reconstructed training image, we calculate the normalized cross-correlation,  $\rho_{NX}$ , with the corresponding ground truth image. For each model, we also establish a  $\rho_{NX}$  cutoff, defined as the  $\rho_{NX}$  between the unblurred ground truth and the ground truth blurred with the nominal beam width of the array. For parameter combinations to be considered for the Top Set, they must reconstruct images for all four training sets that perform better than the respective  $\rho_{NX}$  cutoff for each model.

With the parameter combinations that remain after pruning the original set using the training data, we use reconstructions of the real M87\* data to select the final Top Set. For each recovered M87\* image, we derive closure quantities from the image and compute the reduced chi-squared with respect to the closure quantities measured from the M87\* visibility data. We take only the images that have a  $\chi^2 < 2$ . Note that the real closure quantities are averaged over some time interval (typically over the entire scan) before comparison to ensure sufficient  $S/N$  (Rogers, Doeleman, and Moran, 1995; Blackburn et al., 2020). The distribution of M87\* images in the resulting Top Set represents the uncertainties due to different imaging strategies and assumptions. Validation of the Top Set parameter combinations is then performed by imaging the remaining six geometric models as well as a GRMHD snapshot image and ensuring that the resulting images closely match their ground truths.

The SMILI imaging method performs a similar parameter survey as `eht-imaging`, though it uses slightly different definitions of the regularizers and utilizes a different optimizer. The DIFMAP imaging method also performs a parameter survey, though many of their free parameters are very different from those used in RML: the total assumed compact flux density, cleaning stopping condition, relative weight correction factor for ALMA in self-calibration, diameter of the CLEAN window, and the power-law scaling of the  $(u, v)$ -density weighting function. The Bayesian methods do not survey over any hyperparameters. Rather, they select an appropriate FOV and image pixel size and initialize with a uniform prior for the total flux density for all images. Their respective algorithms then use this single set of assumptions to perform the posterior mapping. This in turn produces an image space with uncertainties reflective of the limited visibility measurements and their errors.

### **Description of `eht-imaging` Pipeline**

The python package `eht-imaging` (Chael et al., 2018) is an RML-based VLBI imaging software capable of producing images by placing different relative weights on the fits to closure quantities and complex visibilities. The results in this paper

were produced by performing a parameter survey based on the 2017 M87\* imaging pipeline <sup>1</sup>. A streamlined and parallelized software package was written using `eht-imaging` tools to make current and future imaging surveys easier to run and is currently being integrated into the main `eht-imaging` codebase.

The `eht-imaging` pipeline presented here uses multiple rounds of imaging via minimizing the RML objective function interleaved with self-calibration of the visibilities to the output image. Self-calibration (see review in Pearson et al., 1984) is a technique that can utilize a science target as its own calibrator source to improve solutions on complex station gains. These gains must be consistent with measured closure quantities, thus the solution improves with increasing numbers of stations. As no unresolved sources exist of the extreme solutions of the EHT to act as gain calibrators, EHT imaging methods rely on self-calibration to achieve better gain solutions.

In our survey, all images are reconstructed with a  $128 \mu\text{as}$  FOV and a  $64 \times 64$  pixel grid. The imaging pipeline starts with loading and coherently scan-averaging the data. Then the correlated flux densities at intra-site baselines are re-scaled by the compact flux density from the chosen parameter combination to remove the contributions from unresolved extended emission outside the FOV. We add an additional fractional systematic error term to the visibilities' error budget to account for unknown amounts of non-closing errors in the data. As measurements taken by the LMT suffer from large gain uncertainties, we perform an initial amplitude-only self-calibration to the LMT data. This self-calibration is performed to a circular Gaussian geometric model with FWHM of  $60 \mu\text{as}$  and flux density of  $0.6 \text{ Jy}$ , chosen to fall in the center of the compact flux density limits derived in Section 5.3. Lastly, the visibility amplitudes are inverse tapered with a  $5 \mu\text{as}$  FWHM circular Gaussian to enforce an angular resolution limit on the final reconstructed image.

After these pre-imaging calibration steps, the pipeline proceeds with four iterations of imaging and self-calibration. The imaging is initialized with a circular Gaussian of FWHM and compact flux density specified by the given parameter combination. The details of the self-calibration and the relative weights placed on fits to the various data products are modified between each iteration to reflect progressing amounts of confidence in the gain and phase solutions. The first two rounds of self-calibration are performed only on the phases while the last two rounds are performed on

---

<sup>1</sup><https://github.com/eventhorizontelescope/2019-D01-02/tree/master/eht-imaging>

amplitudes and phases. For the relative data weights, we begin the first round of imaging by placing unity weight on the closure quantities, a fifth of that on the visibility amplitudes, and no weight on complex visibilities. As we progress through iterations, we remove weight on the visibility amplitudes and allow non-zero weight on complex visibilities. The ratio between weights placed on close quantities compared to complex visibilities decreases in later iterations as we converge on a phase solution. Each iteration involves several attempts at producing an image to prevent the imaging function from getting stuck in a local minimum. Each attempt utilizes the previous best-fit image blurred to the nominal array resolution as the initial image. At the end of all four iterations of imaging, we ensure consistency with the original data and limit the angular resolution of reconstructed features by convolving the final image with the same  $5 \mu\text{as}$  Gaussian used for inverse tapering in the pre-imaging calibration step.

## 5.5 Presentation and Analysis of Images

### Comparison Between Methods, Bands, and Days

Figure 5.4 shows representative images of M87\* produced with each of the five imaging methods using data from the HOPS pipeline. Though we do not show it here, the CASA pipeline data produces comparable images. Images are shown for all four bands on April 21 and April 25. For the DIFMAP and RML methods, we present fiducial images reconstructed using the Top Set parameter combination that maximizes the mean effective blurring kernel FWHM across all four training models. Each synthetic model’s effective blurring kernel FWHM values are derived from the  $\rho_{\text{NX}}$  values. For THEMIS and Comrade, we display a random sample from the posterior.

We first discuss images from the band 3 data on April 21, which represent (together with band 4) the best  $(u, v)$ -coverage and the most stable imaging results. On April 21, DIFMAP, `eht-imaging`, and SMILI could all produce a non-zero number of top set images for all bands. A visual inspection shows that all images display similar characteristics, including diameter, a central flux depression, and a brightness asymmetry in roughly similar positions. Apparent differences in detailed structure between methods can be attributed to differences in the effective resolutions of the imaging pipelines. For example, a  $20 \mu\text{as}$  deconvolution beam is used for DIFMAP imaging, so DIFMAP images tend to have a larger ring width and weaker central depression. In Table 5.3, we show the distribution of hyperparameters in the final Top Set. We note that exact choices of hyperparameters are not necessarily

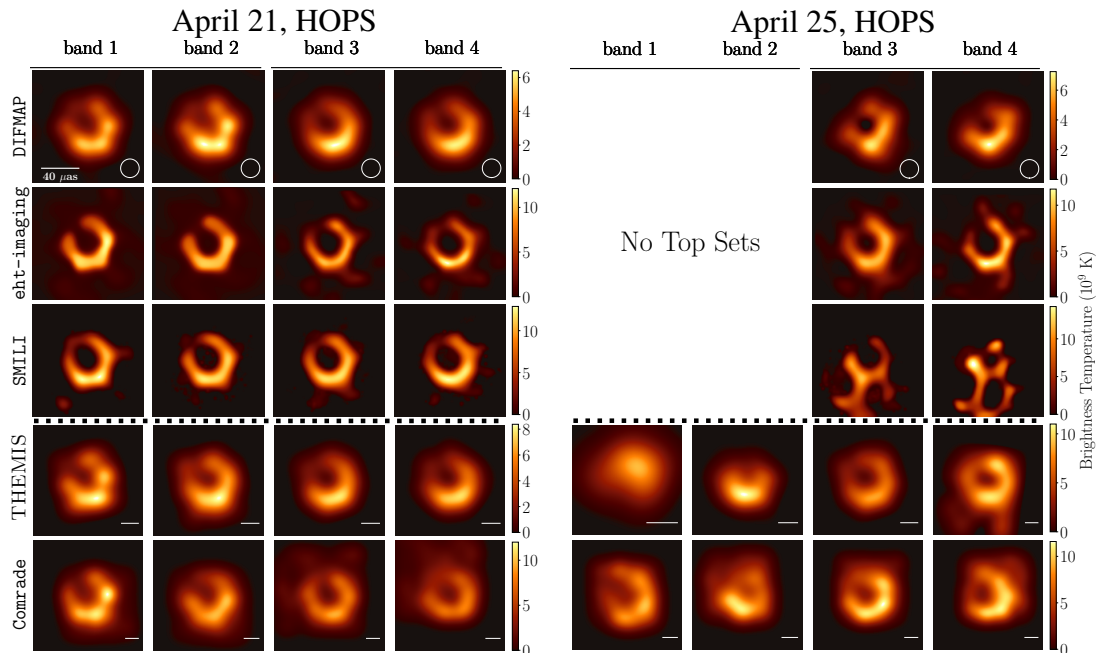


Figure 5.4: The representative images recovered from the HOPS data with all five imaging pipelines for two observing days (April 21 and 25). Each panel shows the fiducial image of the corresponding top set images for DIFMAP, eht-imaging, and SMILI pipelines, and a random sample from the respective posterior for THEMIS and Comrade pipeline. We do not have top sets for band 1 and band 2 from DIFMAP, eht-imaging, and SMILI pipelines on April 25.

correlated to specific changes in image morphology and do not directly relate to physical quantities. In Table 5.4, we show the  $\chi^2$  values for the fiducial images and  $\chi^2$  statistics across the top set for eht-imaging on April 21. The fiducial images are consistent with the data to roughly within the thermal noise, and the  $\chi^2$  values have little scatter across the top set. For the same fiducial parameter set as the images shown in Figure 5.4, we also show images of the training and validation data in Figures 5.5 and 5.6, respectively.

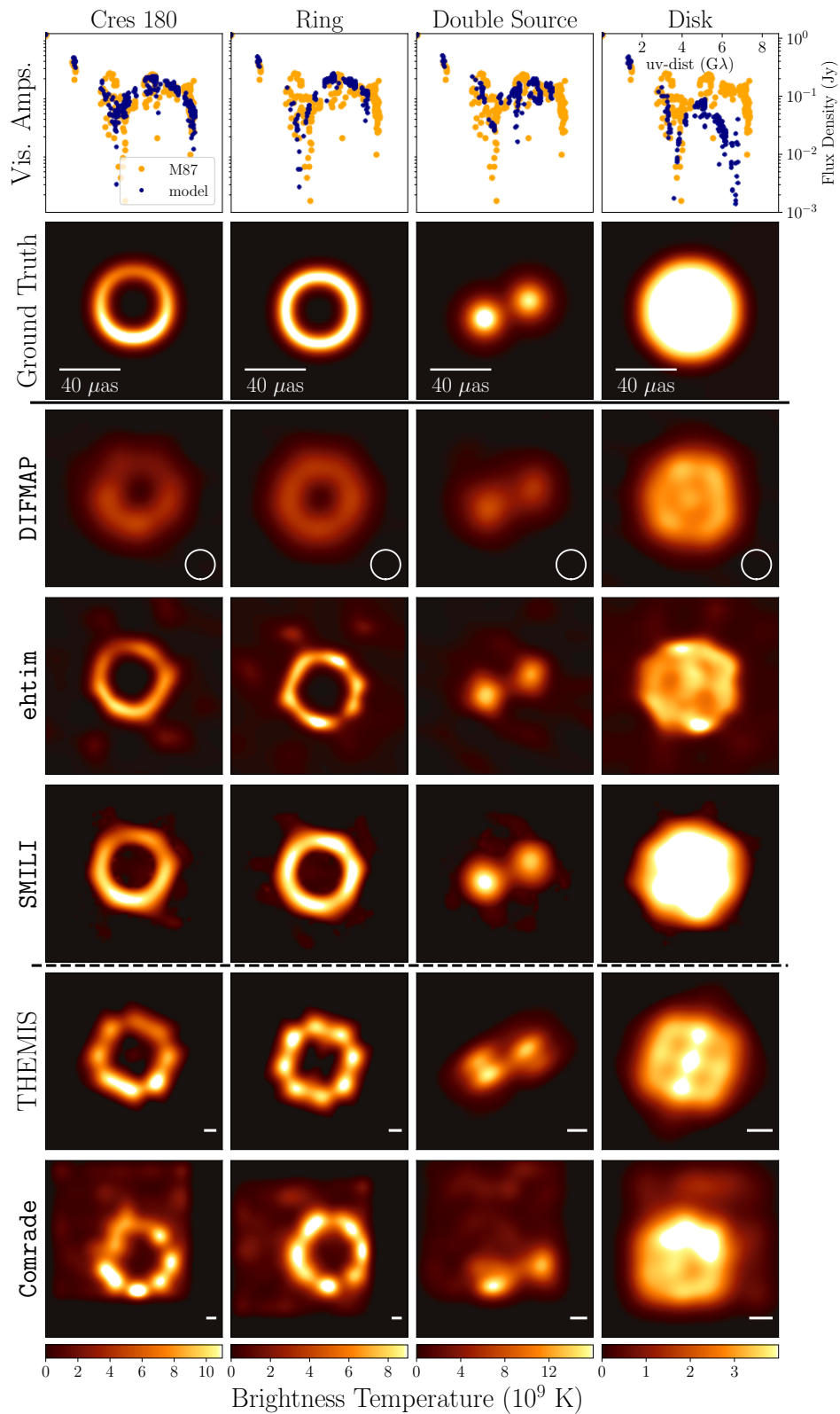


Figure 5.5: Four training geometric models as imaged by each method. The first row shows the visibility amplitudes of the model compared to the visibility amplitudes measured for M87. The second row shows the ground-truth images. The DIFMAP, eht-imaging, and SMILI rows show a fiducial image made from the same parameter sets as the images shown in Fig. 5.4. The THEMIS and Comrade rows show a random draw from the posterior.



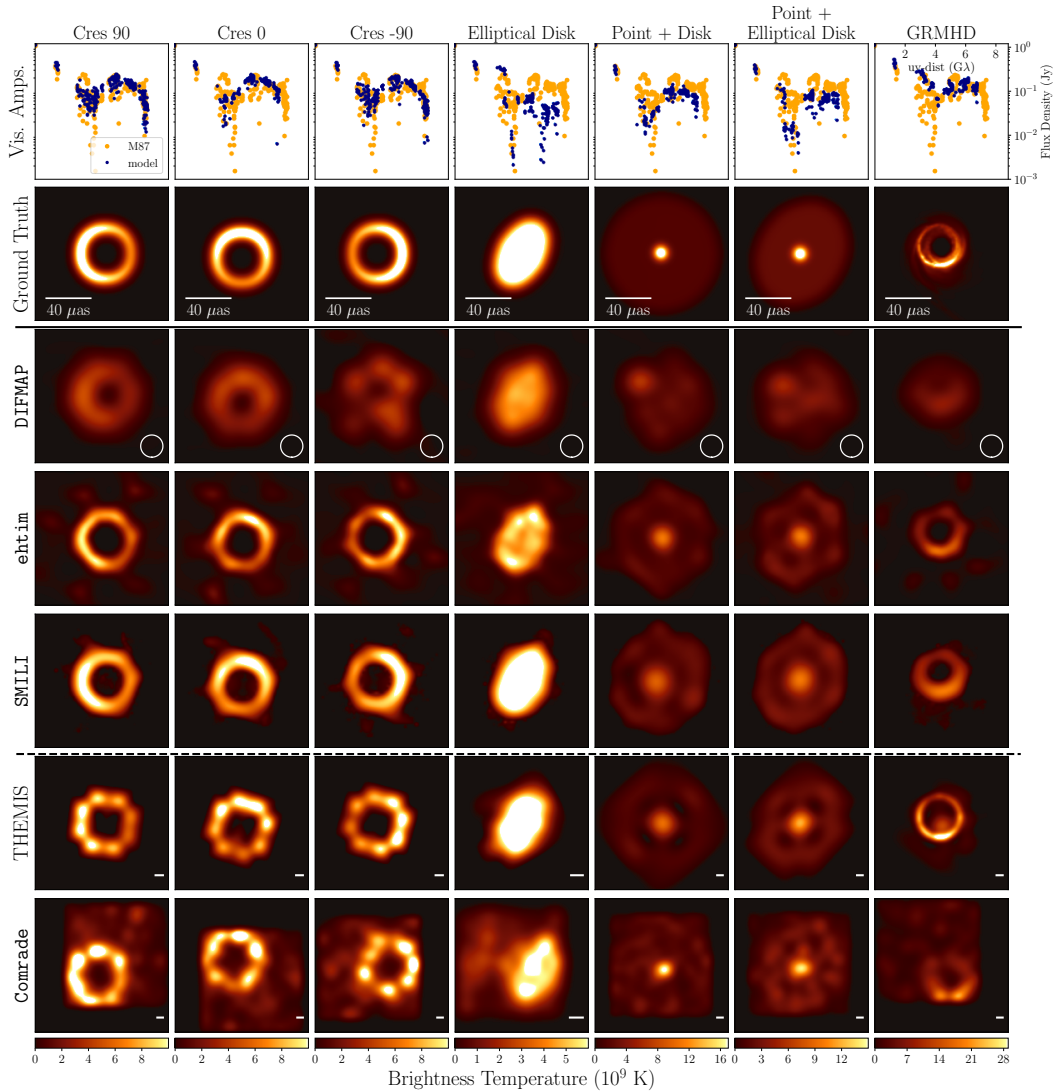


Figure 5.6: Seven geometric validation models plus one GRMHD snapshot as imaged by each method. The first row shows the visibility amplitudes of the model compared to the visibility amplitudes measured for M87. The second row shows the ground-truth images. The DIFMAP, eht-imaging, and SMILI rows show a fiducial image made from the same parameter sets as the images shown in Fig. 5.4. The THEMIS and Comrade rows show a random draw from the posterior.

Details of the observations contribute to the differences between images from different bands and days. The improved  $(u, v)$ -coverage in bands 3 and 4, given by the participation of the GLT, allows for improved reconstructions of M87\* images. The GLT is especially important in probing the null point near  $4 G\lambda$ . This is proven by the increased number of top set images for the trained methods and the cleaner reconstruction of the ring morphology compared to bands 1 and 2.

Table 5.3: Parameters and their surveyed values for the `eht-imaging` pipeline for April 21 band 3 data.

<code>eht-imaging</code> (12288 Param. combinations; 874 in top set)				
Compact	<b>0.4</b>	<b>0.5</b>	<b>0.6</b>	<b>0.7</b>
flux (Jy)	18%	<span style="border: 1px solid black;">27%</span>	29%	26%
Init./MEM	<b>40</b>	<b>50</b>	<b>60</b>	
FWHM ( $\mu\text{as}$ )	<span style="border: 1px solid black;">57%</span>	39%	4%	
Systematic	<b>0%</b>	<b>1%</b>	<b>2%</b>	<b>5%</b>
error	14%	<span style="border: 1px solid black;">22%</span>	30%	34%
Regularizer:	<b>0</b>	<b>1</b>	<b>10</b>	<b>100</b>
MEM	0%	0%	5%	<span style="border: 1px solid black;">95%</span>
TV	33%	<span style="border: 1px solid black;">36%</span>	30%	0%
TSV	31%	<span style="border: 1px solid black;">33%</span>	35%	1%
$\ell_1$	26%	<span style="border: 1px solid black;">25%</span>	25%	24%

**Note.** The `eht-imaging` survey produced  $4 \times 3 \times 4 \times 4 \times 4 \times 4 = 12288$  parameter combinations, and 874 of these passed the criteria for inclusion in the top set. Below each parameter value we specify the fraction of the top set parameter combinations that include that value. Boxed parameters are those corresponding to the fiducial images. Note that the fiducial parameters are determined by identifying the parameter combinations that jointly perform best on all the synthetic data sets; the fiducial parameters do not necessarily correspond with the parameters that have the largest share in the top set.

On April 25, DIFMAP, `eht-imaging`, and SMILI struggled to produce a significant number of top set images – none of the methods could produce Top Set images for bands 1 and 2. The Bayesian methods also struggle to produce a ring-like morphology for data taken on this day. This performance issue is mainly due to a lack of data from LMT on this day. The LMT-SMT baseline provides the only probe of the visibility structure around  $1\text{ G}\lambda$ ; the lack of this baseline hampers imaging.

### Image Statistics

The distribution of images in the Top Set helps us understand the image uncertainties associated with each method. Figure 5.7 shows the image- and visibility-domain uncertainties associated with the image sets for `eht-imaging`. The uncertainties shown for `eht-imaging` reflect the uncertainties in choosing the regularizer weights and hyperparameters. Similar to the corresponding figure in Event Horizon

Table 5.4: Closure quantity  $\chi^2$  values for the fiducial M87\* images and  $\chi^2$  statistics (mean and standard deviation) for Top Set images.  $\chi^2$  values with systematic uncertainties of 0 %, 1 %, and 10 % are shown.

		eht-imaging		
		0%	1%	10%
Apr 21				
Fiducial:	$\chi_{\text{CP}}^2$	1.09	0.94	0.37
	$\chi_{\log \text{CA}}^2$	1.01	0.96	0.34
top set:	$\chi_{\text{CP}}^2$	$1.24 \pm 0.29$	$0.97 \pm 0.14$	$0.34 \pm 0.05$
top set:	$\chi_{\log \text{CA}}^2$	$1.16 \pm 0.28$	$1.10 \pm 0.26$	$0.33 \pm 0.06$

Telescope Collaboration et al., 2019d, we find that the high image uncertainties correspond to locations of high brightness temperature and visibility-domain uncertainties primarily due to gaps in  $(u, v)$ -coverage. We see in the image domain figure of normalized standard deviation that small concentrations of uncertainties exist at various locations along the ring. However, they are less pronounced than the “knots” in 2017. The very small amount of uncertainty in the central flux depression indicates the robustness of the ring feature, as it occurs in nearly every Top Set image. The normalized standard deviation’s visibility-domain shows a similar concentration of uncertainty around  $2 \text{ G}\lambda$ . The fractional standard deviation image shows a sharp increase in uncertainty at the boundary between  $(u, v)$ -distances probed by the EHT versus those outside the maximum probed distance. This indicates that the RML methods are not assigning high confidence to image features smaller than the minimum scale probed by the observations.

### Comparison with 2017 Images

A major motivation for observing M87\* with EHT over multiple years is to verify the asymmetric ring image from the 2017 observations and to monitor any potential changes in morphology. A visual inspection of images from the two years shows remarkable consistency, as seen in Figure 5.8. For quantifying the consistency, we use two image domain feature extraction (IDFE) tools, REx (available as part of eht-imaging) and VIDA (Tiede, Broderick, and Palumbo, 2022) to derive ring diameter, ring width, and brightness position angle for comparison with IDFE results from the 2017 images. Most of the methods are consistent with each other for all bands on April 21 and bands 3+4 on April 25 across the three extracted features

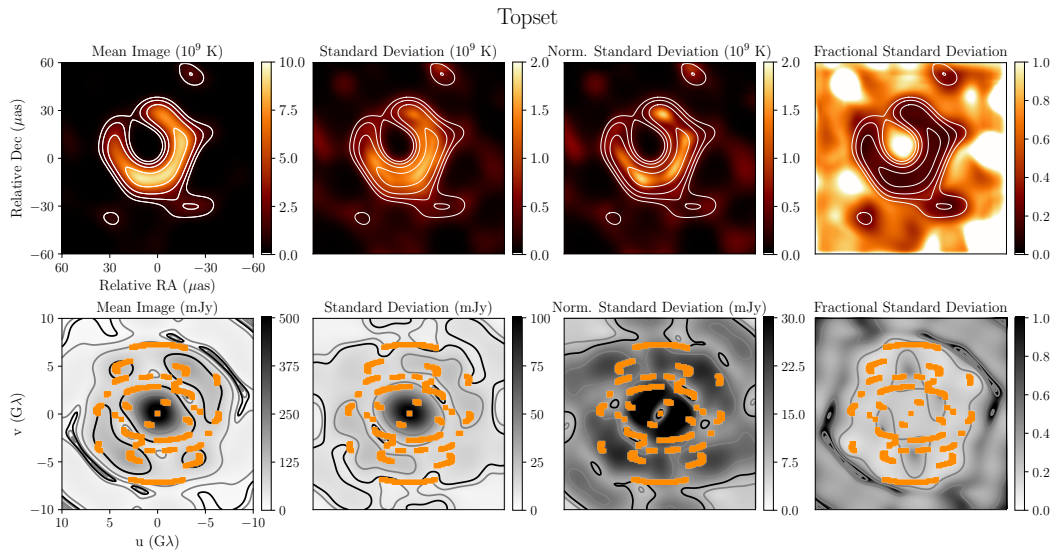


Figure 5.7: Visualization of image statistics calculated using the top set images from the `eht-imaging` pipeline for observations taken on April 21 band 3. We emphasize that these images do not represent the posterior probability space for the reconstructions. Each image reconstructed using `eht-imaging` is the maximum a posteriori (MAP) image for a given parameter set. Thus, the statistics shown represent uncertainties that arise from difference choices of regularizer weights, not from an exploration of posterior space. The top row shows top statistics in the image domain while the bottom row shows the visibility domain. Overlaid on the visibility domain panels is the  $(u, v)$ -coverage for the April 21 observation. From left to right, we present the mean image; the standard deviation; the normalized standard deviation, calculated by re-scaling each image to the flux of the mean image; and the fractional standard deviation, calculated by dividing the standard deviation by the mean. The fractional standard deviation panel has been clipped to a maximum value of 1. Portions of the image exhibit large fractional standard deviations due to pixel values very close to zero in the mean image. In the top row, image contours are drawn at 10%, 20%, 40%, and 80% of the peak values from the mean image. In the bottom row, the grey contours represent 0.1%, 1%, and 10% of the peak while the black contours represent 10 and 100 mJy (left three panels) and 0.1 (right most panel). The complex visibilities are calculated by taking a Fourier transform of the images and then we calculated the mean and standard deviation. The absolute value of the mean and standard deviation of complex visibilities is taken to calculate visibility amplitudes.

to within  $1\sigma$ . They are also consistent with the 2017 results for both the ring diameter and width. The position angle of the brightness asymmetry appears to have undergone a significant shift ( $\sim 30^\circ$ ). Though works such as Wielgus et al., 2020 have suggested large scale PA shifts over the years, this may represent the first image-domain evidence of the phenomena. Recent long-term monitoring studies of

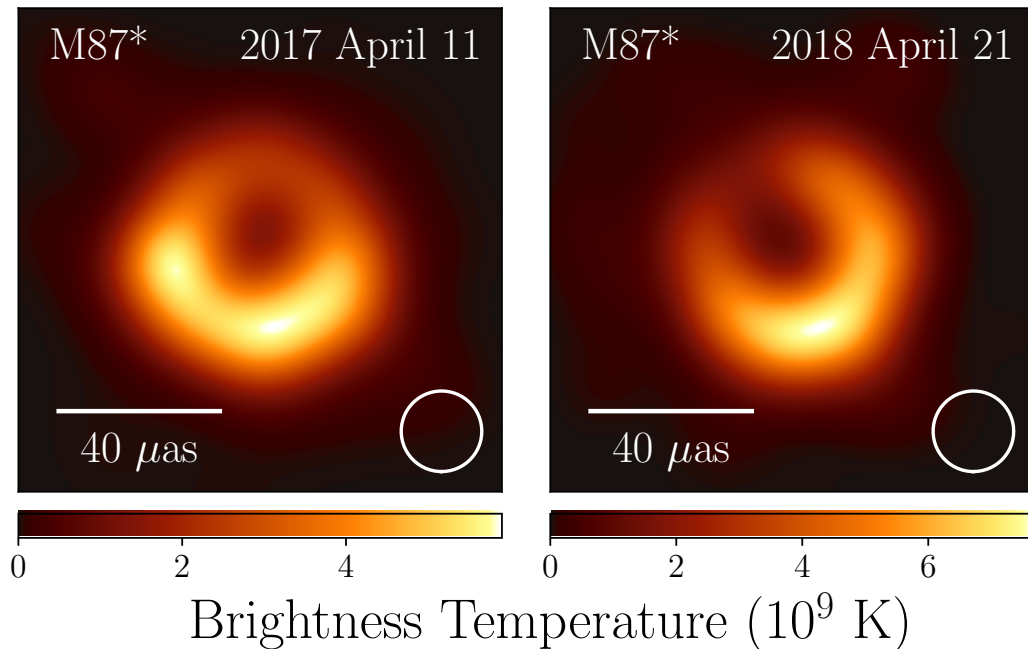


Figure 5.8: Representative example images of M87\* from the EHT observations taken on 2017 April 11 and 2018 April 21 (north is up and east is to the left). The 2017 image is generated with the average of fiducial parameter sets using DIFMAP, eht-imaging, and SMILI (Event Horizon Telescope Collaboration et al., 2019d). The 2018 image is created by taking the average of images generated and blurred from DIFMAP, eht-imaging, SMILI, THEMIS, and Comrade. Comparison of the images shows consistency in ring width and diameter across the observations.

Table 5.5: Comparison of the image-domain extracted ring parameters for 2017 and 2018.

	2017	2018
Ring Diameter	$42 \pm 3 \mu\text{as}$	$41 \pm 1 \mu\text{as}$
Orientation PA	$150^\circ - 200^\circ$ east of north	$208^\circ \pm 5^\circ$ east of north

M87\* using longer-wavelength VLBI have found a systematic PA oscillation of the parsec-scale jet, which could be caused by flow instabilities (Walker et al., 2018) or precession of the central compact source (Cui et al., 2023). However, the true significance of this PA variation and any correlation with physical effects can only be discerned using analysis of more epochs of data.

## 5.6 Conclusion

This work focused on the imaging and analysis of the 2018 EHT observations of M87\* using `eht-imaging`, a python regularized maximum likelihood based code designed for imaging VLBI datasets. The 2018 observations featured improved hardware and participation of a new station, the GLT. Using the precedent set by work done on the 2017 observations, we use multiple independent calibration, imaging, and analysis methods to recover images with consistent morphology across multiple days and bands. The images share an asymmetric ring morphology with consistent diameter and width to those recovered in 2017, but display a notable shift in brightness position angle. The physical significance of this shift, especially in correlation with evolution of the large scale jet morphology, remains to be revealed with future epochs of observations and further VLBI monitoring of M87.

*Chapter 6*

## THE ROAD AHEAD

This thesis describes contributions to the evolving field of time-domain millimeter astronomy. As outlined in Chapter 1, the millimeter sky is, quite literally, exploding with interesting phenomena waiting to be explored, but the challenge has been in the scarcity of millimeter observing resources. Though we have an idea of what is most likely to be discovered in the advent of wide-field millimeter surveys (Eftekhari et al., 2022), I believe that the importance of targeted, sensitive, well-sampled brightness evolution measurements cannot be overlooked and SPRITE will be a crucial resource in the coming years.

In the wise words of Arno Penzias, "the simplest, most reliable radio equipment capable of doing the job is likely to produce the greatest output of astronomical data. Intricate, hard-to operate equipment, even if inherently more sensitive, is itself apt to require so much attention that little time can be spent in observation and measurement" (Penzias and Burrus, 1973). This is the philosophy upon which SPRITE was built over the past few years. My work at OVRO, highlighted in Chapter 2, has constantly asked how can something be done as simply as possible, how can systems be as user friendly as possible? Though many frameworks for millimeter interferometry existed already for CARMA, I believe the steps we have taken to simplify the instrument are just the beginning for what SPRITE may evolve into in the years to come. The basic instrumentation and software mechanics for taking observations with SPRITE have just recently been completed, and this work unfortunately did not have the time to undertake the exciting science programs planned for the instrument. However, my hopes are to see future graduate students, equipped with a reliably built instrument, align their journeys to SPRITE.

As of this writing, to my knowledge, SPRITE is currently the only university operated millimeter telescope and the power to design its observing program gives Caltech the opportunity to define future directions in millimeter observations. I hope to see millimeter transients pushed beyond small-number statistics into the regime of population synthesis studies. SPRITE offers a resource to characterize the rates and luminosity functions of flares from specific stars. It offers the ability to constrain what fraction of supernovae exhibit extreme enough mass loss to produce



Figure 6.1: Nitika, pictured in front of the two SPRITE antennas, at the end of a long and happy day of work at OVRO.

bright millimeter emission, as described in Chapter 3, or to better understand jet evolution near the jet base from populations of X-ray binaries or TDEs, as alluded to in Chapter 4. These studies are only possible by prompt follow-up, unhindered by the delay in applying for telescope time at big observatories, which may be unwilling to sacrifice observing resources for potential non-detections. Additionally, I hope to see more coordinated observations with SPRITE and other Caltech instruments, either at OVRO or Palomar, to build more complete multi-wavelength pictures of the transient sky. For example, Palomar Observatory supports a small, targeted telescope called Flarescope (Davis, Hallinan, and Saini, 2023), which is dedicated to the study of extrasolar space weather. Coordinated LWA-SPRITE-Flarescope detections of stellar flares would yield spectral and timing information that could provide powerful constraints on the energies and mechanisms of flares.

Beyond SPRITE, OVRO will also see one of the 10.4 m Leighton antennas join the Event Horizon Telescope (Raymond et al., 2021). Though several new candidate sites are under consideration, a combination of OVRO's existing infrastructure and



the knowledge gained through commissioning SPRITE will likely position OVRO as the first new fully commissioned station in the next year. The expansion of the EHT is motivated by the desire to push beyond the imaging goals achieved in Chapter 5, such as resolving the black holes' photon rings (Tiede et al., 2022), making multifrequency images of black holes (Chael et al., 2023), and temporally resolving variable structure through movies of black holes (Johnson et al., 2023). The desire for ever-better angular resolution has initiated studies about pushing millimeter-VLBI to space, opening up the possibility for an exciting new era for the EHT.

In March 2023, I was at OVRO when fringes with SPRITE were detected for the first time and Mark Hodges said to me "these are the first millimeter measurements at OVRO since the dishes were moved up to the White Mountains." I hope this thesis inspires confidence that OVRO is entering a revitalized era of millimeter astrophysics and with any luck, SPRITE will live on as part of OVRO's legacy. I feel blessed to have spent my years as a graduate student working in the Owens Valley desert, turning screws and hauling around lab equipment. The fundamentals of radio astronomy can truly only be learned by doing and I hope those who follow in my footsteps derive the same joy and the same enlightenment from OVRO as I did.

## BIBLIOGRAPHY

- Abazajian, K. et al. (July 2019). “CMB-S4 Science Case, Reference Design, and Project Plan”. In: *arXiv e-prints*, arXiv:1907.04473, arXiv:1907.04473. doi: 10.48550/arXiv.1907.04473. arXiv: 1907.04473 [astro-ph.IM].
- Akiyama, K. et al. (Apr. 2017). “Superresolution Full-polarimetric Imaging for Radio Interferometry with Sparse Modeling”. In: *The Astronomical Journal* 153.4, 159, p. 159. doi: 10.3847/1538-3881/aa6302. arXiv: 1702.00424 [astro-ph.IM].
- Anderson, M. M. et al. (Dec. 2019). “New Limits on the Low-frequency Radio Transient Sky Using 31 hr of All-sky Data with the OVRO-LWA”. In: *The Astrophysical Journal* 886.2, 123, p. 123. doi: 10.3847/1538-4357/ab4f87. arXiv: 1911.04591 [astro-ph.HE].
- Andreoni, I. et al. (Dec. 2022). “A very luminous jet from the disruption of a star by a massive black hole”. In: *Nature* 612.7940, pp. 430–434. doi: 10.1038/s41586-022-05465-8. arXiv: 2211.16530 [astro-ph.HE].
- Archinal, B. A. et al. (Feb. 2011). “Report of the IAU Working Group on Cartographic Coordinates and Rotational Elements: 2009”. In: *Celestial Mechanics and Dynamical Astronomy* 109.2, pp. 101–135. doi: 10.1007/s10569-010-9320-4.
- Astropy Collaboration et al. (Aug. 2022). “The Astropy Project: Sustaining and Growing a Community-oriented Open-source Project and the Latest Major Release (v5.0) of the Core Package”. In: *The Astrophysical Journal* 935.2, 167, p. 167. doi: 10.3847/1538-4357/ac7c74.
- Balister, M. et al. (Aug. 1977). “Observations of SiO masers at 43 GHz with the Parkes radio telescope.” In: *Monthly Notices of the Royal Astronomical Society* 180, pp. 415–427. doi: 10.1093/mnras/180.3.415.
- Bardeen, J. M. (Jan. 1973). “Timelike and null geodesics in the Kerr metric.” In: *Black Holes (Les Astres Occlus)*, pp. 215–239.
- Bellm, E. C. et al. (Jan. 2019). “The Zwicky Transient Facility: System Overview, Performance, and First Results”. In: *Publications of the Astronomical Society of the Pacific* 131.995, p. 018002. doi: 10.1088/1538-3873/aaecbe. arXiv: 1902.01932 [astro-ph.IM].
- Bietenholz, M. F. et al. (2021). “The Radio Luminosity-risetime Function of Core-collapse Supernovae”. In: *The Astrophysical Journal* 908.1, p. 75. ISSN: 0004-637X. doi: 10.3847/1538-4357/abccd9. eprint: 2011.11737. URL: <https://doi.org/10.3847/1538-4357/abccd9>.

- Bird, S. et al. (Dec. 2010). “The inner halo of M 87: a first direct view of the red-giant population”. In: *Astronomy and Astrophysics* 524, A71, A71. DOI: 10.1051/0004-6361/201014876. arXiv: 1009.3202 [astro-ph.GA].
- Blackburn, L. et al. (Sept. 2019). “EHT-HOPS Pipeline for Millimeter VLBI Data Reduction”. In: *The Astrophysical Journal* 882.1, 23, p. 23. DOI: 10.3847/1538-4357/ab328d. arXiv: 1903.08832 [astro-ph.IM].
- Blackburn, L. et al. (May 2020). “Closure Statistics in Interferometric Data”. In: *The Astrophysical Journal* 894.1, 31, p. 31. DOI: 10.3847/1538-4357/ab8469. arXiv: 1910.02062 [astro-ph.IM].
- Blakeslee, J. P. et al. (Mar. 2009). “The ACS Fornax Cluster Survey. V. Measurement and Recalibration of Surface Brightness Fluctuations and a Precise Value of the Fornax-Virgo Relative Distance”. In: *The Astrophysical Journal* 694.1, pp. 556–572. DOI: 10.1088/0004-637X/694/1/556. arXiv: 0901.1138 [astro-ph.CO].
- Blandford, R. D. and A. Konigl (Aug. 1979). “Relativistic jets as compact radio sources”. In: *The Astrophysical Journal* 232, p. 34. ISSN: 0004-637X. DOI: 10.1086/157262. URL: <https://ui.adsabs.harvard.edu/abs/1979ApJ...232...34B/abstract>.
- Blandford, R. D. and D. G. Payne (June 1982). “Hydromagnetic flows from accretion disks and the production of radio jets.” In: *Monthly Notices of the Royal Astronomical Society* 199, pp. 883–903. DOI: 10.1093/mnras/199.4.883.
- Blandford, R. D. and R. L. Znajek (May 1977). “Electromagnetic extraction of energy from Kerr black holes.” In: *Monthly Notices of the Royal Astronomical Society* 179, pp. 433–456. DOI: 10.1093/mnras/179.3.433.
- Blandford, R., D. Meier, and A. Readhead (Aug. 2019). “Relativistic Jets from Active Galactic Nuclei”. In: 57, pp. 467–509. DOI: 10.1146/annurev-astro-081817-051948. arXiv: 1812.06025 [astro-ph.HE].
- Blondin, S. et al. (Oct. 2006). “Supernova 2006jd in UGC 4179”. In: *Central Bureau Electronic Telegrams* 679, p. 1.
- Bochenek, C. D. et al. (Mar. 2020). “STARE2: Detecting Fast Radio Bursts in the Milky Way”. In: *Publications of the Astronomical Society of the Pacific* 132.1009, 034202, p. 034202. DOI: 10.1088/1538-3873/ab63b3. arXiv: 2001.05077 [astro-ph.HE].
- Bower, G. C. et al. (Dec. 2003). “A Giant Outburst at Millimeter Wavelengths in the Orion Nebula”. In: *The Astrophysical Journal* 598.2, pp. 1140–1150. DOI: 10.1086/379101. arXiv: astro-ph/0308277 [astro-ph].
- Broderick, A. E. et al. (July 2020). “THEMIS: A Parameter Estimation Framework for the Event Horizon Telescope”. In: *The Astrophysical Journal* 897.2, 139, p. 139. DOI: 10.3847/1538-4357/ab91a4.

- Burton, K., M. A. MacGregor, and R. A. Osten (Nov. 2022). “First Millimeter Flares Detected from Eridani with the Atacama Large Millimeter/submillimeter Array”. In: *The Astrophysical Journal Letters* 939.1, L6, p. L6. DOI: 10.3847/2041-8213/ac9973. arXiv: 2210.10818 [astro-ph.SR].
- Cantiello, M. et al. (Apr. 2018). “The Next Generation Virgo Cluster Survey (NGVS). XVIII. Measurement and Calibration of Surface Brightness Fluctuation Distances for Bright Galaxies in Virgo (and Beyond)”. In: *The Astrophysical Journal* 856.2, 126, p. 126. DOI: 10.3847/1538-4357/aab043. arXiv: 1802.05526 [astro-ph.GA].
- Cao, H. et al. (Aug. 2020). “JVLA C-band observation on AT2019wey”. In: *The Astronomer’s Telegram* 13984, p. 1.
- Cao, Y. et al. (2013). “Discovery, progenitor and early evolution of a stripped envelope supernova iPTF13bvn”. In: *Astrophysical Journal Letters* 775.1, p. 7. ISSN: 20418205. DOI: 10.1088/2041-8205/775/1/L7. arXiv: 1307.1470.
- Carilli, C. L., J. E. Carlstrom, and M. A. Holdaway (Jan. 1999). “Millimeter Interferometry”. In: *Synthesis Imaging in Radio Astronomy II*. Ed. by G. B. Taylor, C. L. Carilli, and R. A. Perley. Vol. 180. Astronomical Society of the Pacific Conference Series, p. 565.
- Carilli, C. and M. Holdaway (1997). “Application of Fast Switching Phase Calibration at mm Wavelengths on 33 km Baselines<sup>1</sup>”. In: *VLA Scientific Memos* 173.
- CASA Team et al. (Nov. 2022). “CASA, the Common Astronomy Software Applications for Radio Astronomy”. In: *Publications of the Astronomical Society of the Pacific* 134.1041, 114501, p. 114501. DOI: 10.1088/1538-3873/ac9642. arXiv: 2210.02276 [astro-ph.IM].
- Chael, A. et al. (Mar. 2023). “Multifrequency Black Hole Imaging for the Next-generation Event Horizon Telescope”. In: *The Astrophysical Journal* 945.1, 40, p. 40. DOI: 10.3847/1538-4357/acb7e4. arXiv: 2210.12226 [astro-ph.HE].
- Chael, A. A. et al. (Apr. 2018). “Interferometric Imaging Directly with Closure Phases and Closure Amplitudes”. In: *The Astrophysical Journal* 857.1, 23, p. 23. DOI: 10.3847/1538-4357/aab6a8. arXiv: 1803.07088 [astro-ph.IM].
- Chandra, P. (2018). “Circumstellar Interaction in Supernovae in Dense Environments—An Observational Perspective”. In: *Space Science Reviews* 214.1. ISSN: 15729672. DOI: 10.1007/s11214-017-0461-6. arXiv: 1712.07405.
- Chandra, P. et al. (Aug. 2012). “Radio and X-Ray Observations of SN 2006jd: Another Strongly Interacting Type II In Supernova”. In: *The Astrophysical Journal* 755.2, 110, p. 110. DOI: 10.1088/0004-637X/755/2/110. arXiv: 1205.0250 [astro-ph.HE].

- Chandra, P. et al. (Sept. 2015). “X-Ray and Radio Emission from Type II<sub>n</sub> Supernova SN 2010jl”. In: *The Astrophysical Journal* 810.1, 32, p. 32. DOI: 10.1088/0004-637X/810/1/32. arXiv: 1507.06059 [astro-ph.HE].
- Charlot, P. et al. (Oct. 2020). “The third realization of the International Celestial Reference Frame by very long baseline interferometry”. In: *arXiv e-prints*, arXiv:2010.13625, arXiv:2010.13625. arXiv: 2010.13625 [astro-ph.GA].
- Chevalier, R. A. (1982). “The radio and X-ray emission from type II supernovae”. In: *The Astrophysical Journal* 259, p. 302. ISSN: 0004-637X. DOI: 10.1086/160167.
- Chevalier, R. A. (June 1998). “Synchrotron Self-Absorption in Radio Supernovae”. In: *The Astrophysical Journal* 499.2, pp. 810–819. ISSN: 0004-637X. DOI: 10.1086/305676. URL: <https://ui.adsabs.harvard.edu/abs/1998ApJ...499..810C/abstract>.
- Chevalier, R. A. and C. Fransson (Jan. 1994). “Emission from circumstellar interaction in normal Type II supernovae”. In: *The Astrophysical Journal* 420, p. 268. ISSN: 0004-637X. DOI: 10.1086/173557. URL: <https://ui.adsabs.harvard.edu/abs/1994ApJ...420..268C/abstract>.
- Chugai, N. N. (1990). “Late Stage Radiation Source in Type-II Supernovae - Radioactivity or Shock Heating”. In: *Soviet Astronomy Letters* 16.6/NOV, p. 457. URL: <https://ui.adsabs.harvard.edu/abs/1990SvAL...16..457C/abstract>.
- Ciprini, S. et al. (Mar. 2004). “Radio-optical flux behaviour and spectral energy distribution of the intermediate blazar GC 0109+224”. In: *Monthly Notices of the Royal Astronomical Society* 348.4, pp. 1379–1387. DOI: 10.1111/j.1365-2966.2004.07467.x. arXiv: astro-ph/0401271 [astro-ph].
- Connor, L. et al. (July 2021). “Galactic Radio Explorer: An All-sky Monitor for Bright Radio Bursts”. In: *Publications of the Astronomical Society of the Pacific* 133.1025, 075001, p. 075001. DOI: 10.1088/1538-3873/ac0bcc. arXiv: 2101.09905 [astro-ph.HE].
- Cui, Y.-Z. et al. (2023). “Precessing jet nozzle connecting to a spinning black hole in M87”. In: *Nature*. submitted. URL: <https://www.researchsquare.com/article/rs-2624984/v1>.
- Curtis, H. D. (Jan. 1918). “Descriptions of 762 Nebulae and Clusters Photographed with the Crossley Reflector”. In: *Publications of Lick Observatory* 13, pp. 9–42.
- Czekala, I. et al. (Feb. 2016). “A Disk-based Dynamical Constraint on the Mass of the Young Binary DQ Tau”. In: *The Astrophysical Journal* 818.2, 156, p. 156. DOI: 10.3847/0004-637X/818/2/156. arXiv: 1601.03806 [astro-ph.SR].
- Davis, I., G. Hallinan, and N. Saini (Jan. 2023). “Flarescope: Multi-wavelength Monitoring of Space Weather from Young, Sun-like Stars”. In: *American Astronomical Society Meeting Abstracts*. Vol. 55. American Astronomical Society Meeting Abstracts, 346.07, p. 346.07.

- De, K. et al. (Feb. 2020). “Palomar Gattini-IR: Survey Overview, Data Processing System, On-sky Performance and First Results”. In: *Publications of the Astronomical Society of the Pacific* 132.1008, 025001, p. 025001. DOI: 10.1088/1538-3873/ab6069. arXiv: 1910.13319 [astro-ph.IM].
- De Ugarte Postigo, A. et al. (Aug. 2012). “Pre-ALMA observations of GRBs in the mm/submm range”. In: *Astronomy and Astrophysics* 538, p. 44. ISSN: 00046361. DOI: 10.1051/0004-6361/201117848. arXiv: 1108.1797. URL: <http://arxiv.org/abs/1108.1797> <http://dx.doi.org/10.1051/0004-6361/201117848>.
- Deller, A. T. et al. (Mar. 2011). “DiFX-2: A More Flexible, Efficient, Robust, and Powerful Software Correlator”. In: *Publications of the Astronomical Society of the Pacific* 123.901, p. 275. DOI: 10.1086/658907. arXiv: 1101.0885 [astro-ph.IM].
- Dhawan, V., I. F. Mirabel, and L. F. Rodriguez (2000). “AU-Scale Synchrotron Jets and Superluminal Ejecta in GRS 1915+105”. In: *The Astrophysical Journal* 543.1, pp. 373–385. ISSN: 0004-637X. DOI: 10.1086/317088. arXiv: 0006086 [astro-ph].
- Doeleman, S. S. et al. (May 2001). “Structure of Sagittarius A\* at 86 GHz using VLBI Closure Quantities”. In: *The Astronomical Journal* 121.5, pp. 2610–2617. DOI: 10.1086/320376. arXiv: astro-ph/0102232 [astro-ph].
- Doeleman, S. S. et al. (Sept. 2008). “Event-horizon-scale structure in the supermassive black hole candidate at the Galactic Centre”. In: *Nature* 455.7209, pp. 78–80. DOI: 10.1038/nature07245. arXiv: 0809.2442 [astro-ph].
- Doeleman, S. S. et al. (Oct. 2012). “Jet-Launching Structure Resolved Near the Supermassive Black Hole in M87”. In: *Science* 338.6105, p. 355. DOI: 10.1126/science.1224768. arXiv: 1210.6132 [astro-ph.HE].
- Dolan, G. J., T. G. Phillips, and D. P. Woody (Mar. 1979). “Low-noise 115-GHz mixing in superconducting oxide-barrier tunnel junctions”. In: *Applied Physics Letters* 34.5, 347, p. 347. DOI: 10.1063/1.90783.
- Draine, B. T. (2011). *Physics of the Interstellar and Intergalactic Medium*.
- Drout, M. R. et al. (Oct. 2014). “Rapidly Evolving and Luminous Transients from Pan-STARRS1”. In: *The Astrophysical Journal* 794.1, 23, p. 23. DOI: 10.1088/0004-637X/794/1/23. arXiv: 1405.3668 [astro-ph.HE].
- Dulk, G. A. (Jan. 1985). “Radio emission from the sun and stars.” In: 23, pp. 169–224. DOI: 10.1146/annurev.aa.23.090185.001125.
- Duran, R. B., E. Nakar, and T. Piran (Jan. 2013). “Radius constraints and minimal equipartition energy of relativistically moving synchrotron sources”. In: *Astrophysical Journal* 772.1, p. 78. DOI: 10.1088/0004-637X/772/1/78. arXiv: 1301.6759. URL: <http://arxiv.org/abs/1301.6759> <http://dx.doi.org/10.1088/0004-637X/772/1/78>.

- Dwarkadas, V. V. et al. (2016). “X-ray and radio emission from the luminous supernova 2005kd”. In: *Monthly Notices of the Royal Astronomical Society* 462.1, pp. 1101–1110. ISSN: 13652966. DOI: 10.1093/mnras/stw1717. URL: <https://academic.oup.com/mnras/article/462/1/1101/2589973>.
- Eftekhari, T. et al. (Aug. 2022). “Extragalactic Millimeter Transients in the Era of Next-generation CMB Surveys”. In: *The Astrophysical Journal* 935.1, 16, p. 16. DOI: 10.3847/1538-4357/ac7ce8. arXiv: 2110.05494 [astro-ph.HE].
- Event Horizon Telescope Collaboration et al. (Apr. 2019a). “First M87 Event Horizon Telescope Results. I. The Shadow of the Supermassive Black Hole”. In: *The Astrophysical Journal Letters* 875.1, L1. (M87\* 2017 I), p. L1. DOI: 10.3847/2041-8213/ab0ec7.
- Event Horizon Telescope Collaboration et al. (Apr. 2019b). “First M87 Event Horizon Telescope Results. II. Array and Instrumentation”. In: *The Astrophysical Journal Letters* 875.1, L2. (M87\* 2017 II), p. L2. DOI: 10.3847/2041-8213/ab0c96.
- Event Horizon Telescope Collaboration et al. (Apr. 2019c). “First M87 Event Horizon Telescope Results. III. Data Processing and Calibration”. In: *The Astrophysical Journal Letters* 875.1, L3. (M87\* 2017 III), p. L3. DOI: 10.3847/2041-8213/ab0c57.
- Event Horizon Telescope Collaboration et al. (Apr. 2019d). “First M87 Event Horizon Telescope Results. IV. Imaging the Central Supermassive Black Hole”. In: *The Astrophysical Journal Letters* 875.1, L4. (M87\* 2017 IV), p. L4. DOI: 10.3847/2041-8213/ab0e85.
- Event Horizon Telescope Collaboration et al. (May 2022). “First Sagittarius A\* Event Horizon Telescope Results. I. The Shadow of the Supermassive Black Hole in the Center of the Milky Way”. In: *The Astrophysical Journal Letters* 930.2, L12, p. L12. DOI: 10.3847/2041-8213/ac6674.
- Falcke, H. and P. L. Biermann (Jan. 1995). “The jet-disk symbiosis. I. Radio to X-ray emission models for quasars.” In: *Astronomy and Astrophysics* 293, pp. 665–682. arXiv: astro-ph/9411096 [astro-ph].
- Falcke, H. and P. L. Biermann (Oct. 1999). “The jet/disk symbiosis: III. What the radio cores in GRS 1915+105, NGC 4258, M 81 and Sgr A\* tell us about accreting black holes”. In: *Astronomy and Astrophysics* 342.1, pp. 49–56. ISSN: 00046361. arXiv: 9810226 [astro-ph]. URL: <http://arxiv.org/abs/astro-ph/9810226>.
- Falcke, H., F. Melia, and E. Agol (Jan. 2000). “Viewing the Shadow of the Black Hole at the Galactic Center”. In: *The Astrophysical Journal Letters* 528.1, pp. L13–L16. DOI: 10.1086/312423. arXiv: astro-ph/9912263 [astro-ph].
- Fender, R. et al. (Apr. 2015). “The Transient Universe with the Square Kilometre Array”. In: *Advancing Astrophysics with the Square Kilometre Array (AASKA14)*, 51, p. 51. arXiv: 1507.00729 [astro-ph.HE].

- Fender, R. P., T. M. Belloni, and E. Gallo (Dec. 2004). “Towards a unified model for black hole X-ray binary jets”. In: *MNRAS* 355.4, pp. 1105–1118. DOI: 10.1111/j.1365-2966.2004.08384.x. arXiv: astro-ph/0409360 [astro-ph].
- Fender, R. (Dec. 2003). “Jets from X-ray binaries”. In: *Compact Stellar X-ray Sources*. Cambridge University Press, pp. 381–420. DOI: 10.1017/cbo9780511536281.010. arXiv: 0303339 [astro-ph].
- Findlay, J. W. (Jan. 1971). “Filled-Aperture Antennas for Radio Astronomy”. In: 9, p. 271. DOI: 10.1146/annurev.aa.09.090171.001415.
- Foreman-Mackey, D. et al. (Mar. 2013). “emcee: The MCMC Hammer”. In: *Publications of the Astronomical Society of the Pacific* 125.925, p. 306. DOI: 10.1086/670067. arXiv: 1202.3665 [astro-ph.IM].
- Gal-Yam, A. et al. (2007). “On the Progenitor of SN 2005gl and the Nature of Type II<sub>n</sub> Supernovae”. In: *The Astrophysical Journal* 656.1, pp. 372–381. ISSN: 0004-637X. DOI: 10.1086/510523. arXiv: 0608029 [astro-ph]. URL: <http://www.cfht.hawaii.edu>.
- Gallo, E., R. P. Fender, and G. G. Pooley (Sept. 2003). “A universal radio-X-ray correlation in low/hard state black hole binaries”. In: *Monthly Notices of the Royal Astronomical Society* 344.1, pp. 60–72. DOI: 10.1046/j.1365-8711.2003.06791.x. arXiv: astro-ph/0305231 [astro-ph].
- Gebhardt, K. and J. Thomas (Aug. 2009). “The Black Hole Mass, Stellar Mass-to-Light Ratio, and Dark Halo in M87”. In: *The Astrophysical Journal* 700.2, pp. 1690–1701. DOI: 10.1088/0004-637X/700/2/1690. arXiv: 0906.1492 [astro-ph.CO].
- Gebhardt, K. et al. (Mar. 2011). “The Black Hole Mass in M87 from Gemini/NIFS Adaptive Optics Observations”. In: *The Astrophysical Journal* 729.2, 119, p. 119. DOI: 10.1088/0004-637X/729/2/119. arXiv: 1101.1954 [astro-ph.CO].
- Getman, K. V. et al. (Mar. 2011). “The Young Binary DQ Tau: A Hunt for X-ray Emission from Colliding Magnetospheres”. In: *The Astrophysical Journal* 730.1, 6, p. 6. DOI: 10.1088/0004-637X/730/1/6. arXiv: 1101.4044 [astro-ph.SR].
- Giroletti, M. et al. (Nov. 2020). “EVN 6.7 GHz detection of AT2019wey on milliarcsecond scales”. In: *The Astronomer’s Telegram* 14168, p. 1.
- Granot, J. and R. Sari (2002). “The Shape of Spectral Breaks in Gamma-Ray Burst Afterglows”. In: *The Astrophysical Journal* 568.2, pp. 820–829. ISSN: 0004-637X. DOI: 10.1086/338966.
- Greisen, E. W. (2003). “AIPS, the VLA, and the VLBA”. In: *Information Handling in Astronomy - Historical Vistas*. Ed. by A. Heck. Vol. 285, p. 109. DOI: 10.1007/0-306-48080-8\_7.



- Guns, S. et al. (Aug. 2021). “Detection of Galactic and Extragalactic Millimeter-wavelength Transient Sources with SPT-3G”. In: *The Astrophysical Journal* 916.2, 98, p. 98. DOI: 10.3847/1538-4357/ac06a3. arXiv: 2103.06166 [astro-ph.HE].
- Hallinan, G. et al. (Sept. 2019). “The DSA-2000 — A Radio Survey Camera”. In: *Bulletin of the American Astronomical Society*. Vol. 51, 255, p. 255. DOI: 10.48550/arXiv.1907.07648. arXiv: 1907.07648 [astro-ph.IM].
- Harms, R. J. et al. (Nov. 1994). “HST FOS Spectroscopy of M87: Evidence for a Disk of Ionized Gas around a Massive Black Hole”. In: *The Astrophysical Journal Letters* 435, p. L35. DOI: 10.1086/187588.
- Hasselfield, M. et al. (Nov. 2013). “The Atacama Cosmology Telescope: Beam Measurements and the Microwave Brightness Temperatures of Uranus and Saturn”. In: *The Astrophysical Journal Supplement Series* 209.1, 17, p. 17. DOI: 10.1088/0067-0049/209/1/17. arXiv: 1303.4714 [astro-ph.IM].
- Hickish, J. et al. (Dec. 2016). “A Decade of Developing Radio-Astronomy Instrumentation using CASPER Open-Source Technology”. In: *Journal of Astronomical Instrumentation* 5.4, 1641001-12, pp. 1641001–12. DOI: 10.1142/S2251171716410014. arXiv: 1611.01826 [astro-ph.IM].
- Hickish, J. et al. (Apr. 2018). “A digital correlator upgrade for the Arcminute MicroKelvin Imager”. In: *Monthly Notices of the Royal Astronomical Society* 475.4, pp. 5677–5687. DOI: 10.1093/mnras/sty074. arXiv: 1707.04237 [astro-ph.IM].
- Hilbert, D. (1917). “Nachrichten von der Königlichen Gesellschaft der Wissenschaften zu Göttingen - Mathematisch-physikalische Klasse”. In: Berlin: Weidmannsche Buchhandlung. Chap. Die Grundlagen der Physik - Zweite Mitteilung, pp. 53–76.
- Hills, J. G. (Mar. 1975). “Possible power source of Seyfert galaxies and QSOs”. In: *Nature* 254.5498, pp. 295–298. DOI: 10.1038/254295a0.
- Hjellming, R. M. and K. J. Johnston (June 1981). “An analysis of the proper motions of SS 433 radio jets”. In: *The Astrophysical Journal* 246, p. L141. ISSN: 0004-637X. DOI: 10.1086/183571. URL: <https://ui.adsabs.harvard.edu/abs/1981ApJ...246L.141H/abstract>.
- Hjellming, R. M. and K. J. Johnston (May 1988). “Radio emission from conical jets associated with X-ray binaries”. In: *The Astrophysical Journal* 328, p. 600. ISSN: 0004-637X. DOI: 10.1086/166318. URL: <https://ui.adsabs.harvard.edu/abs/1988ApJ...328..600H/abstract>.
- Ho, A. Y. Q. et al. (Jan. 2019a). “AT2018cow: A Luminous Millimeter Transient”. In: *The Astrophysical Journal* 871.1, 73, p. 73. DOI: 10.3847/1538-4357/aaf473. arXiv: 1810.10880 [astro-ph.HE].

- Ho, A. Y. Q. et al. (Jan. 2019b). “AT2018cow: A Luminous Millimeter Transient”. In: *The Astrophysical Journal* 871.1, 73, p. 73. DOI: 10.3847/1538-4357/aaf473. arXiv: 1810.10880 [astro-ph.HE].
- Ho, A. Y. Q. et al. (May 2020). “The Koala: A Fast Blue Optical Transient with Luminous Radio Emission from a Starburst Dwarf Galaxy at  $z = 0.27$ ”. In: *The Astrophysical Journal* 895.1, 49, p. 49. DOI: 10.3847/1538-4357/ab8bcf. arXiv: 2003.01222 [astro-ph.HE].
- Ho, A. Y. Q. et al. (Oct. 2021). “Luminous Millimeter, Radio, and X-ray Emission from ZTF20acigmel (AT2020xnd)”. In: *arXiv e-prints*, arXiv:2110.05490, arXiv:2110.05490. arXiv: 2110.05490 [astro-ph.HE].
- Ho, A. Y. Q. et al. (June 2022). “Luminous Millimeter, Radio, and X-Ray Emission from ZTF 20acigmel (AT 2020xnd)”. In: *The Astrophysical Journal* 932.2, 116, p. 116. DOI: 10.3847/1538-4357/ac4e97. arXiv: 2110.05490 [astro-ph.HE].
- Ho, P. T. P., J. M. Moran, and K. Y. Lo (Nov. 2004). “The Submillimeter Array”. In: *The Astrophysical Journal Letters* 616.1, pp. L1–L6. DOI: 10.1086/423245. arXiv: astro-ph/0406352 [astro-ph].
- Högbom, J. A. (June 1974). “Aperture Synthesis with a Non-Regular Distribution of Interferometer Baselines”. In: 15, p. 417.
- Horesh, A. et al. (Dec. 2013). “An early and comprehensive millimetre and centimetre wave and X-ray study of SN 2011dh: A non-equipartition blast wave expanding into a massive stellar wind”. In: *Monthly Notices of the Royal Astronomical Society* 436.2, pp. 1258–1267. ISSN: 00358711. DOI: 10.1093/mnras/stt1645. arXiv: arXiv:1209.1102. URL: <https://ui.adsabs.harvard.edu/abs/2013MNRAS.436.1258H/abstract>.
- Humphreys, R. M. and K. Davidson (Oct. 1994). “The Luminous Blue Variables: Astrophysical Geysers”. In: *Publications of the Astronomical Society of the Pacific* 106, p. 1025. DOI: 10.1086/133478.
- Ichimaru, S. (June 1977). “Bimodal behavior of accretion disks: theory and application to Cygnus X-1 transitions.” In: *The Astrophysical Journal* 214, pp. 840–855. DOI: 10.1086/155314.
- Igumenshchev, I. V., R. Narayan, and M. A. Abramowicz (Aug. 2003). “Three-dimensional Magnetohydrodynamic Simulations of Radiatively Inefficient Accretion Flows”. In: *The Astrophysical Journal* 592.2, pp. 1042–1059. DOI: 10.1086/375769. arXiv: astro-ph/0301402 [astro-ph].
- Inoue, M. et al. (July 2014). “Greenland telescope project: Direct confirmation of black hole with sub-millimeter VLBI”. In: *Radio Science* 49.7, pp. 564–571. DOI: 10.1002/2014RS005450. arXiv: 1407.2450 [astro-ph.IM].

- Jackson, P. D., M. R. Kundu, and S. M. White (Feb. 1989). “Quiescent and flaring radio emission from the flare stars AD Leonis, EQ Pegasi, UV Ceti, Wolf 630, YY Geminorum and YZ Canis Minoris.” In: *Astronomy and Astrophysics* 210, pp. 284–294.
- Janssen, M. et al. (June 2019). “rPICARD: A CASA-based calibration pipeline for VLBI data. Calibration and imaging of 7 mm VLBA observations of the AGN jet in M 87”. In: *Astronomy and Astrophysics* 626, A75, A75. DOI: 10.1051/0004-6361/201935181. arXiv: 1905.01905 [astro-ph.IM].
- Jennison, R. C. (Jan. 1958). “A phase sensitive interferometer technique for the measurement of the Fourier transforms of spatial brightness distributions of small angular extent”. In: *Monthly Notices of the Royal Astronomical Society* 118, p. 276. DOI: 10.1093/mnras/118.3.276.
- Johnson, M. D. et al. (Apr. 2023). “Key Science Goals for the Next-Generation Event Horizon Telescope”. In: *Galaxies* 11.3, p. 61. DOI: 10.3390/galaxies11030061. arXiv: 2304.11188 [astro-ph.HE].
- Kassim, N. E. et al. (Dec. 1993). “Subarcminute Resolution Imaging of Radio Sources at 74 MHz With the Very Large Array”. In: *The Astronomical Journal* 106, p. 2218. DOI: 10.1086/116795.
- Keene, J. and C. Masson (Oct. 1986). “A compact density condensation around L1551-IRS 5: 2.7mm continuum observations with 4” resolution”. In: *Interstellar Processes: Abstracts of Contributed Papers*. Ed. by D. J. Hollenbach and J. Thronson H. A., pp. 7–8.
- Kerr, R. P. (Sept. 1963). “Gravitational Field of a Spinning Mass as an Example of Algebraically Special Metrics”. In: 11.5, pp. 237–238. DOI: 10.1103/PhysRevLett.11.237.
- Kim, J. -. et al. (Sept. 2018). “The limb-brightened jet of M87 down to the 7 Schwarzschild radii scale”. In: *Astronomy and Astrophysics* 616, A188, A188. DOI: 10.1051/0004-6361/201832921. arXiv: 1805.02478 [astro-ph.GA].
- Kochanek, C. S. (Mar. 2019). “The physics of flash (supernova) spectroscopy”. In: *Monthly Notices of the Royal Astronomical Society* 483.3, pp. 3762–3772. ISSN: 13652966. DOI: 10.1093/mnras/sty3363. eprint: 1807.09778. URL: <https://academic.oup.com/mnras/article/483/3/3762/5247719>.
- Kocz, J. et al. (Oct. 2019). “DSA-10: a prototype array for localizing fast radio bursts”. In: *Monthly Notices of the Royal Astronomical Society* 489.1, pp. 919–927. DOI: 10.1093/mnras/stz2219. arXiv: 1906.08699 [astro-ph.IM].
- Krichbaum, T. P. et al. (July 1998). “VLBI observations of the galactic center source SGR A\* at 86 GHz and 215 GHz”. In: *Astronomy and Astrophysics* 335, pp. L106–L110.

- Kulkarni, S. R. et al. (Oct. 1998). “Radio emission from the unusual supernova 1998bw and its association with the  $\gamma$ -ray burst of 25 April 1998”. In: *Nature* 395.6703, pp. 663–669. ISSN: 00280836. DOI: 10.1038/27139. URL: <https://ui.adsabs.harvard.edu/abs/1998Natur.395..663K/abstract>.
- Kutner, M. L. and B. L. Ulich (Nov. 1981). “Recommendations for calibration of millimeter-wavelength spectral line data.” In: *The Astrophysical Journal* 250, pp. 341–348. DOI: 10.1086/159380.
- Lamb, J. W. et al. (July 2022). “COMAP Early Science. II. Pathfinder Instrument”. In: *The Astrophysical Journal* 933.2, 183, p. 183. DOI: 10.3847/1538-4357/ac63c6. arXiv: 2111.05928 [astro-ph.IM].
- Laskar, T. et al. (Oct. 2013). “A reverse shock in GRB 130427A”. In: *Astrophysical Journal* 776.2, p. 119. ISSN: 15384357. DOI: 10.1088/0004-637X/776/2/119. arXiv: 1305.2453. URL: <http://www.cfa.harvard.edu/mmti/wfs.html>.
- Law, N. M. et al. (Dec. 2009). “The Palomar Transient Factory: System Overview, Performance, and First Results”. In: *Publications of the Astronomical Society of the Pacific* 121.886, p. 1395. DOI: 10.1086/648598. arXiv: 0906.5350 [astro-ph.IM].
- Leighton, R. B. (1977). *A 10-Meter Telescope for Millimeter and Sub-Millimeter Astronomy*. Tech. rep. AST 73-04908. California Institute of Technology.
- Louis, T. et al. (July 2014). “The Atacama Cosmology Telescope: cross correlation with Planck maps”. In: 2014.7, 016, p. 016. DOI: 10.1088/1475-7516/2014/07/016. arXiv: 1403.0608 [astro-ph.CO].
- Lourie, N. P. et al. (Dec. 2020). “The wide-field infrared transient explorer (WINTER)”. In: *Ground-based and Airborne Instrumentation for Astronomy VIII*. Ed. by C. J. Evans, J. J. Bryant, and K. Motohara. Vol. 11447. Society of Photo-Optical Instrumentation Engineers (SPIE) Conference Series, 114479K, 114479K. DOI: 10.1117/12.2561210. arXiv: 2102.01109 [astro-ph.IM].
- Luminet, J. -. (May 1979). “Image of a spherical black hole with thin accretion disk.” In: *Astronomy and Astrophysics* 75, pp. 228–235.
- Lyapin, A. et al. (Mar. 2020). “Optical observations of the optical and X-ray transient ATLAS19bcxp = SRGA J043520.9+552226 = SRGE J043523.3+552234: a likely BL Lac object”. In: *The Astronomer’s Telegram* 13576, p. 1.
- Maccarone, T. J. et al. (Dec. 2018). “Revealing the Galactic Population of Black Holes”. In: *Science with a Next Generation Very Large Array*. Ed. by E. Murphy. Vol. 517. Astronomical Society of the Pacific Conference Series, p. 711. arXiv: 1806.07270 [astro-ph.HE].
- Maccarone, T. J. et al. (Apr. 2019). “Astro2020 Science White Paper: Compact Stellar Jets”. In: *arXiv e-prints*, arXiv:1904.11845, arXiv:1904.11845. arXiv: 1904.11845 [astro-ph.HE].

- Macchetto, F. et al. (Nov. 1997). “The Supermassive Black Hole of M87 and the Kinematics of Its Associated Gaseous Disk”. In: *The Astrophysical Journal* 489.2, pp. 579–600. DOI: 10.1086/304823. arXiv: astro-ph/9706252 [astro-ph].
- MacGregor, A. M., R. A. Osten, and A. M. Hughes (Mar. 2020a). “Properties of M Dwarf Flares at Millimeter Wavelengths”. In: *The Astrophysical Journal* 891.1, 80, p. 80. DOI: 10.3847/1538-4357/ab711d.
- MacGregor, A. M., R. A. Osten, and A. M. Hughes (Mar. 2020b). “Properties of M Dwarf Flares at Millimeter Wavelengths”. In: *The Astrophysical Journal* 891.1, 80, p. 80. DOI: 10.3847/1538-4357/ab711d.
- MacGregor, M. A. et al. (Mar. 2018). “Detection of a Millimeter Flare from Proxima Centauri”. In: *The Astrophysical Journal Letters* 855.1, L2, p. L2. DOI: 10.3847/2041-8213/aaad6b. arXiv: 1802.08257 [astro-ph.EP].
- MacGregor, M. A. et al. (Apr. 2021). “Discovery of an Extremely Short Duration Flare from Proxima Centauri Using Millimeter through Far-ultraviolet Observations”. In: *The Astrophysical Journal Letters* 911.2, L25, p. L25. DOI: 10.3847/2041-8213/abf14c. arXiv: 2104.09519 [astro-ph.SR].
- MAGIC Collaboration et al. (Oct. 2018). “The broad-band properties of the intermediate synchrotron peaked BL Lac S2 0109+22 from radio to VHE gamma-rays”. In: *Monthly Notices of the Royal Astronomical Society* 480.1, pp. 879–892. DOI: 10.1093/mnras/sty1753.
- Margutti, R. et al. (2014). “A PANCHROMATIC VIEW OF THE RESTLESS SN 2009ip REVEALS THE EXPLOSIVE EJECTION OF A MASSIVE STAR ENVELOPE”. In: *The Astrophysical Journal* 780.38pp, p. 21. DOI: 10.1088/0004-637X/780/1/21.
- Margutti, R. et al. (Feb. 2019). “An Embedded X-Ray Source Shines through the Aspherical AT 2018cow: Revealing the Inner Workings of the Most Luminous Fast-evolving Optical Transients”. In: *The Astrophysical Journal* 872.1, 18, p. 18. DOI: 10.3847/1538-4357/aafa01. arXiv: 1810.10720 [astro-ph.HE].
- Mathieu, R. D. et al. (May 1997). “The Classical T Tauri Spectroscopic Binary DQ Tau.I.Orbital Elements and Light Curves”. In: *The Astronomical Journal* 113, p. 1841. DOI: 10.1086/118395.
- Matsuoka, M. et al. (Oct. 2009). “The MAXI Mission on the ISS: Science and Instruments for Monitoring All-Sky X-Ray Images”. In: 61, p. 999. DOI: 10.1093/pasj/61.5.999. arXiv: 0906.0631 [astro-ph.IM].
- Matsuoka, T. et al. (2019). “Radio Emission from Supernovae in the Very Early Phase: Implications for the Dynamical Mass Loss of Massive Stars”. In: *The Astrophysical Journal* 885.1, p. 41. ISSN: 0004-637X. DOI: 10.3847/1538-4357/ab4421. arXiv: 1909.05874. URL: <https://doi.org/10.3847/1538-4357/ab4421>.

- Mauerhan, J. C. et al. (Apr. 2013). “The unprecedented 2012 outburst of SN 2009ip: a luminous blue variable star becomes a true supernova”. In: *MNRAS* 430.3, pp. 1801–1810. ISSN: 0035-8711. DOI: 10.1093/MNRAS/STT009. arXiv: arXiv:1209.6320. URL: <https://ui.adsabs.harvard.edu/abs/2013MNRAS.430.1801M/abstract>.
- Mauron, N. and E. Josselin (2011). “The mass-loss rates of red supergiants and the de Jager prescription”. In: *Astronomy and Astrophysics* 526.19, p. 156. ISSN: 00046361. DOI: 10.1051/0004-6361/201013993. arXiv: 1010.5369. URL: <http://www.aanda.org>.
- McClintock, J. E. and R. A. Remillard (2009). “Black hole binaries”. In: *Compact Stellar X-ray Sources*, pp. 157–214. DOI: 10.1017/cbo9780511536281.005. arXiv: 0306213 [astro-ph].
- Mereminskiy, I. et al. (Mar. 2020). “SRG discovery of SRGA J043520.9+552226 = SRGE J043523.3+552234, an X-ray counterpart of optical transient ATLAS19bcxp”. In: *The Astronomer’s Telegram* 13571, p. 1.
- Metzger, B. D., P. K. Williams, and E. Berger (2015). “EXTRAGALACTIC SYNCHROTRON TRANSIENTS IN THE ERA OF WIDE-FIELD RADIO SURVEYS. I. DETECTION RATES AND LIGHT CURVE CHARACTERISTICS”. In: *Astrophysical Journal* 806.2. ISSN: 15384357. DOI: 10.1088/0004-637X/806/2/224. arXiv: 1502.01350.
- Miller-Jones, J. C. A. et al. (Apr. 2019). “A rapidly changing jet orientation in the stellar-mass black-hole system V404 Cygni”. In: *Nature* 569.7756, pp. 374–377. DOI: 10.1038/s41586-019-1152-0. arXiv: 1906.05400 [astro-ph.HE].
- Mirabel, I. F. and L. F. Rodríguez (Sept. 1994). “A superluminal source in the Galaxy”. In: *Nature* 371.6492, pp. 46–48. ISSN: 00280836. DOI: 10.1038/371046a0. URL: <https://ui.adsabs.harvard.edu/abs/1994Natur.371...46M/abstract>.
- Mirabel, I. F. and L. F. Rodríguez (Jan. 1999). “Sources of Relativistic Jets in the Galaxy”. In: 37, pp. 409–443. DOI: 10.1146/annurev.astro.37.1.409. arXiv: astro-ph/9902062 [astro-ph].
- Moriya, T. J. and N. Tominaga (2012). “Diversity of luminous supernovae from non-steady mass loss”. In: *Astrophysical Journal* 747.2, p. 118. ISSN: 15384357. DOI: 10.1088/0004-637X/747/2/118. arXiv: 1110.3807.
- Moriya, T. J. et al. (2013). “An analytic bolometric light curve model of interaction-powered supernovae and its application to type II<sub>n</sub> supernovae”. In: *Monthly Notices of the Royal Astronomical Society* 435.2, pp. 1520–1535. ISSN: 00358711. DOI: 10.1093/mnras/stt1392. arXiv: 1307.2644. URL: <https://academic.oup.com/mnras/article/435/2/1520/1041189>.

- Moriya, T. J. et al. (2014). “Mass-loss histories of type II<sub>n</sub> supernova progenitors within decades before their explosion”. In: *Monthly Notices of the Royal Astronomical Society* 439.3, pp. 2917–2926. ISSN: 13652966. DOI: 10.1093/mnras/stu163. URL: <https://academic.oup.com/mnras/article/439/3/2917/1109776>.
- Mundy, G. L. et al. (Jan. 1990). “Results from 1.4 Millimeter Wavelength Interferometry at the Owens Valley”. In: *Submillimetre Astronomy*. Ed. by G. D. Watt and A. S. Webster. Vol. 158, p. 155. DOI: 10.1007/978-94-015-6850-0\_54.
- Naess, S. et al. (2020). “The Atacama Cosmology Telescope: Detection of mm-wave transient sources”. In: *Arxiv preprint arXiv:2012.14347*. arXiv: 2012.14347. URL: <http://arxiv.org/abs/2012.14347>.
- Naess, S. et al. (July 2021). “The Atacama Cosmology Telescope: Detection of Millimeter-wave Transient Sources”. In: *The Astrophysical Journal* 915.1, 14, p. 14. DOI: 10.3847/1538-4357/abfe6d. arXiv: 2012.14347 [astro-ph.SR].
- Nakar, E. and R. Sari (Dec. 2010). “Early supernovae light curves following the shock breakout”. In: *Astrophysical Journal* 725.1, pp. 904–921. ISSN: 15384357. DOI: 10.1088/0004-637X/725/1/904. arXiv: 1004.2496. URL: <https://iopscience.iop.org/article/10.1088/0004-637X/725/1/904>  
<https://iopscience.iop.org/article/10.1088/0004-637X/725/1/904/meta>.
- Napier, P. J. et al. (May 1994). “The Very Long Baseline Array.” In: *IEEE Proceedings* 82.5, pp. 658–672. DOI: 10.1109/5.284733.
- Narayan, R., I. V. Igumenshchev, and M. A. Abramowicz (Dec. 2003). “Magnetically Arrested Disk: an Energetically Efficient Accretion Flow”. In: 55, pp. L69–L72. DOI: 10.1093/pasj/55.6.L69. arXiv: astro-ph/0305029 [astro-ph].
- Narayan, R. and R. Nityananda (Jan. 1986). “Maximum entropy image restoration in astronomy.” In: 24, pp. 127–170. DOI: 10.1146/annurev.aa.24.090186.001015.
- Narayan, R. and I. Yi (June 1994). “Advection-dominated Accretion: A Self-similar Solution”. In: *The Astrophysical Journal Letters* 428, p. L13. DOI: 10.1086/187381. arXiv: astro-ph/9403052 [astro-ph].
- Narayan, R. et al. (Nov. 2012). “GRMHD simulations of magnetized advection-dominated accretion on a non-spinning black hole: role of outflows”. In: *Monthly Notices of the Royal Astronomical Society* 426.4, pp. 3241–3259. DOI: 10.1111/j.1365-2966.2012.22002.x. arXiv: 1206.1213 [astro-ph.HE].
- Pacholczyk, A. G. (1970). *Radio astrophysics. Nonthermal processes in galactic and extragalactic sources*.
- Padin, S. et al. (May 1991). “The Owens Valley Millimeter Array”. In: *Publications of the Astronomical Society of the Pacific* 103, p. 461. DOI: 10.1086/132843.

- Palmer, H. P. et al. (Feb. 1967). “Radio Diameter Measurements with Interferometer Baselines of One Million and Two Million Wavelengths”. In: *Nature* 213.5078, pp. 789–790. DOI: 10.1038/213789a0.
- Panagia, N. and M. Felli (Feb. 1975). “The spectrum of the free-free radiation from extended envelopes.” In: *Astronomy and Astrophysics* 39, pp. 1–5.
- Parsons, A. et al. (Nov. 2008). “A Scalable Correlator Architecture Based on Modular FPGA Hardware, Reuseable Gateway, and Data Packetization”. In: *Publications of the Astronomical Society of the Pacific* 120.873, p. 1207. DOI: 10.1086/593053. arXiv: 0809.2266 [astro-ph].
- Pearson, T. J. et al. (Sept. 1984). “Image Formation by Self-Calibration in Radio Astronomy”. In: *ARA&A* 22.1, pp. 97–130. ISSN: 0066-4146. DOI: 10.1146/ANNUREV.AA.22.090184.000525. URL: <https://ui.adsabs.harvard.edu/abs/1984ARA%7B%5C%7DA..22...97P/abstract>.
- Penzias, A. A. and C. A. Burrus (Jan. 1973). “Millimeter-Wavelength Radio-Astronomy Techniques”. In: 11, p. 51. DOI: 10.1146/annurev.aa.11.090173.000411.
- Perley, D. A. et al. (2020). “The Zwicky Transient Facility Bright Transient Survey. II. A Public Statistical Sample for Exploring Supernova Demographics”. In: *The Astrophysical Journal* 904.1, p. 35. ISSN: 1538-4357. DOI: 10.3847/1538-4357/abbd98. arXiv: 2009.01242. URL: <https://doi.org/10.3847/1538-4357/abbd98>.
- Phillips, R. B. et al. (Feb. 1996). “Polarized Radio Emission From the Multiple T Tauri System HD 283447”. In: *The Astronomical Journal* 111, p. 918. DOI: 10.1086/117839.
- Phillips, T. G. and D. P. Woody (Sept. 1982). “Millimeter- And Submillimeter-Wave Receivers”. In: *Annual Review of Astronomy and Astrophysics* 20.1, pp. 285–321. ISSN: 0066-4146. DOI: 10.1146/annurev.aa.20.090182.001441.
- Planck Collaboration et al. (Sept. 2020). “Planck 2018 results. III. High Frequency Instrument data processing and frequency maps”. In: *Astronomy and Astrophysics* 641, A3, A3. DOI: 10.1051/0004-6361/201832909. arXiv: 1807.06207 [astro-ph.CO].
- Pooley, G. G. and D. A. Green (Oct. 1993). “Ryle Telescope observations of SN1993J at 15 GHz: the First 115 d”. In: *Monthly Notices of the Royal Astronomical Society* 264.1, pp. L17–L20. ISSN: 0035-8711. DOI: 10.1093/mnras/264.1.117. URL: <https://ui.adsabs.harvard.edu/abs/1993MNRAS.264L..17P/abstract>.
- Raymond, A. W. et al. (Mar. 2021). “Evaluation of New Submillimeter VLBI Sites for the Event Horizon Telescope”. In: *The Astrophysical Journal Supplement Series* 253.1, 5, p. 5. DOI: 10.3847/1538-3881/abc3c3. arXiv: 2102.05482 [astro-ph.IM].



- Rees, M. J. et al. (Jan. 1982). “Ion-supported tori and the origin of radio jets”. In: *Nature* 295.5844, pp. 17–21. DOI: 10.1038/295017a0.
- Reid, M. J. et al. (Jan. 1989). “Subluminal Motion and Limb Brightening in the Nuclear Jet of M87”. In: *The Astrophysical Journal* 336, p. 112. DOI: 10.1086/166998.
- Remillard, R. A. and J. E. McClintock (2006). *X-ray Properties of Black-Hole Binaries*. Tech. rep.
- Richards, P. L. et al. (Mar. 1979). “Quasiparticle heterodyne mixing in SIS tunnel junctions”. In: *Applied Physics Letters* 34.5, 345, p. 345. DOI: 10.1063/1.90782.
- Roesch, F. et al. (June 2023). “Radio Flaring of the Blazar S2 0109+22 on Historical Levels”. In: *The Astronomer’s Telegram* 16093, p. 1.
- Rogers, A. E. E., S. S. Doeleman, and J. M. Moran (Mar. 1995). “Fringe Detection Methods for Very Long Baseline Arrays”. In: *The Astronomical Journal* 109, p. 1391. DOI: 10.1086/117371.
- Russell, T. D. et al. (2015). “Radio monitoring of the hard state jets in the 2011 outburst of MAXI J1836-194”. In: *Monthly Notices of the Royal Astronomical Society* 450.2, pp. 1745–1759. ISSN: 13652966. DOI: 10.1093/mnras/stv723. arXiv: 1503.08634.
- Ruze, J. (Apr. 1966). “Antenna Tolerance Theory – A Review”. In: *IEEE Proceedings* 54, pp. 633–642.
- Ryle, M. (Mar. 1952). “A New Radio Interferometer and Its Application to the Observation of Weak Radio Stars”. In: *Proceedings of the Royal Society of London Series A* 211.1106, pp. 351–375. DOI: 10.1098/rspa.1952.0047.
- Sądowski, A. et al. (Dec. 2013). “Energy, momentum and mass outflows and feedback from thick accretion discs around rotating black holes”. In: *Monthly Notices of the Royal Astronomical Society* 436.4, pp. 3856–3874. DOI: 10.1093/mnras/stt1881. arXiv: 1307.1143 [astro-ph.HE].
- Salter, D. M., M. R. Hogerheijde, and G. A. Blake (Dec. 2008). “Captured at millimeter wavelengths: a flare from the classical T Tauri star DQ Tauri”. In: *Astronomy and Astrophysics* 492.1, pp. L21–L24. DOI: 10.1051/0004-6361/200810807. arXiv: 0810.4162 [astro-ph].
- Salter, D. M. et al. (Oct. 2010). “Recurring millimeter flares as evidence for star-star magnetic reconnection events in the DQ Tauri PMS binary system”. In: *Astronomy and Astrophysics* 521, A32, A32. DOI: 10.1051/0004-6361/201015197. arXiv: 1008.0981 [astro-ph.SR].
- Sari, R. and T. Piran (Aug. 1999). “Predictions for the Very Early Afterglow and the Optical Flash”. In: *The Astrophysical Journal* 520.2, pp. 641–649. DOI: 10.1086/307508. arXiv: astro-ph/9901338 [astro-ph].

- Satapathy, K. et al. (Jan. 2022). “The Variability of the Black Hole Image in M87 at the Dynamical Timescale”. In: *The Astrophysical Journal* 925.1, 13, p. 13. DOI: 10.3847/1538-4357/ac332e. arXiv: 2111.01317 [astro-ph.HE].
- Schwarzschild, K. (Jan. 1916). “On the Gravitational Field of a Mass Point According to Einstein’s Theory”. In: *Abh. Konigl. Preuss. Akad. Wissenschaften Jahre 1906,92, Berlin,1907* 1916, pp. 189–196.
- Shepherd, M. C., T. J. Pearson, and G. B. Taylor (May 1994). “DIFMAP: an interactive program for synthesis imaging.” In: *Bulletin of the American Astronomical Society*. Vol. 26, pp. 987–989.
- Smartt, S. J. (Sept. 2009). “Progenitors of Core-Collapse Supernovae”. In: 47.1, pp. 63–106. DOI: 10.1146/annurev-astro-082708-101737. arXiv: 0908.0700 [astro-ph.SR].
- Smith, N. (2017). “Interacting Supernovae: Types IIn and Ibn”. In: *Handbook of Supernovae*, pp. 403–429. DOI: 10.1007/978-3-319-21846-5\_38. arXiv: 1612.02006.
- Smith, N., K. H. Hinkle, and N. Ryde (2009). “Red supergiants as potential type IIn supernova progenitors: Spatially resolved 4.6  $\mu\text{m}$  CO emission around VY CMa and betelgeuse”. In: *Astronomical Journal* 137.3, pp. 3558–3573. ISSN: 00046256. DOI: 10.1088/0004-6256/137/3/3558. arXiv: arXiv:0811.3037. URL: <https://ui.adsabs.harvard.edu/abs/2009AJ...137.3558S/abstract>.
- Smith, N., J. C. Mauerhan, and J. L. Prieto (Mar. 2014). “SN 2009ip and SN 2010mc: core-collapse Type IIn supernovae arising from blue supergiants”. In: *MNRAS* 438.2, pp. 1191–1207. ISSN: 0035-8711. DOI: 10.1093/MNRAS/STT2269. arXiv: arXiv:1308.0112. URL: <https://ui.adsabs.harvard.edu/abs/2014MNRAS.438.1191S/abstract>.
- Smith, N. and R. Tombleson (2015). “Luminous blue variables are antisocial: Their isolation implies that they are kicked mass gainers in binary evolution”. In: *Monthly Notices of the Royal Astronomical Society* 447.1, pp. 598–617. ISSN: 13652966. DOI: 10.1093/mnras/stu2430. arXiv: 1406.7431. URL: <http://simbad.u-strasbg.fr/simbad/>.
- Soderberg, A. M. et al. (Jan. 2010). “A relativistic type Ibc supernova without a detected  $\gamma$ -ray burst”. In: *Nature* 463.7280, pp. 513–515. ISSN: 00280836. DOI: 10.1038/nature08714. arXiv: 0908.2817. URL: <https://ui.adsabs.harvard.edu/abs/2010Natur.463..513S/abstract>.
- Stirling, A. M. et al. (2001). “A relativistic jet from Cygnus X-1 in the low/hard X-ray state”. In: *Monthly Notices of the Royal Astronomical Society* 327.4, pp. 1273–1278. ISSN: 00358711. DOI: 10.1046/j.1365-8711.2001.04821.x. URL: <https://academic.oup.com/mnras/article/327/4/1273/1009199>.

- Tananbaum, H. et al. (Oct. 1972). “Observation of a Correlated X-Ray Transition in Cygnus X-1”. In: *The Astrophysical Journal* 177, p. L5. ISSN: 0004-637X. DOI: 10.1086/181042. URL: <https://ui.adsabs.harvard.edu/abs/1972ApJ...177L...5T/abstract>.
- Tetarenko, A. J. et al. (Aug. 2017). “Extreme jet ejections from the black hole X-ray binary V404 Cygni”. In: *Monthly Notices of the Royal Astronomical Society* 469.3, pp. 3141–3162. DOI: 10.1093/mnras/stx1048. arXiv: 1704.08726 [astro-ph.HE].
- Tetarenko, A. J. et al. (July 2021). “Measuring fundamental jet properties with multiwavelength fast timing of the black hole X-ray binary MAXI J1820+070”. In: *Monthly Notices of the Royal Astronomical Society* 504.3, pp. 3862–3883. DOI: 10.1093/mnras/stab820. arXiv: 2103.09318 [astro-ph.HE].
- Thompson, A. R., J. M. Moran, and J. Swenson George W. (2017). *Interferometry and Synthesis in Radio Astronomy, 3rd Edition*. DOI: 10.1007/978-3-319-44431-4.
- Tiede, P. (Aug. 2022). “Comrade: Composable Modeling of Radio Emission”. In: *The Journal of Open Source Software* 7.76, 4457, p. 4457. DOI: 10.21105/joss.04457.
- Tiede, P., A. E. Broderick, and D. C. M. Palumbo (Feb. 2022). “Variational Image Feature Extraction for the Event Horizon Telescope”. In: *The Astrophysical Journal* 925.2, 122, p. 122. DOI: 10.3847/1538-4357/ac3a6b.
- Tiede, P. et al. (Dec. 2022). “Measuring Photon Rings with the ngEHT”. In: *Galaxies* 10.6, p. 111. DOI: 10.3390/galaxies10060111. arXiv: 2210.13498 [astro-ph.HE].
- Tingay, S. J. et al. (Mar. 1995). “Relativistic motion in a nearby bright X-ray source”. In: *Nature* 374.6518, pp. 141–143. ISSN: 00280836. DOI: 10.1038/374141a0. URL: <https://www.nature.com/articles/374141a0>.
- Tonry, J. et al. (Dec. 2019). “ATLAS Transient Discovery Report for 2019-12-08”. In: *Transient Name Server Discovery Report* 2019-2553, p. 1.
- Tucker, J. R. (Nov. 1979). “Quantum limited detection in tunnel junction mixers”. In: *IEEE Journal of Quantum Electronics* 15, pp. 1234–1258. DOI: 10.1109/JQE.1979.1069931.
- Vadawale, S. V. et al. (Nov. 2003). “On the Origin of the Various Types of Radio Emission in GRS 1915+105”. In: *The Astrophysical Journal* 597.2, pp. 1023–1035. ISSN: 0004-637X. DOI: 10.1086/378672. arXiv: 0308096 [astro-ph]. URL: <https://ui.adsabs.harvard.edu/abs/2003ApJ...597.1023V/abstract>.

- Vargas-González, J. et al. (June 2023). “A systematic survey of millimetre-wavelength flaring variability of young stellar objects in the Orion Nebula Cluster”. In: *Monthly Notices of the Royal Astronomical Society* 522.1, pp. 56–69. DOI: 10.1093/mnras/stad926. arXiv: 2303.15516 [astro-ph.SR].
- Vink, J. (2020). “Supernova Remnant Evolution”. In: *Physics and Evolution of Supernova Remnants*. Springer, Cham, pp. 87–116. DOI: 10.1007/978-3-030-55231-2\_5. URL: [https://link.springer.com/chapter/10.1007/978-3-030-55231-2%7B%5C\\_%7D5](https://link.springer.com/chapter/10.1007/978-3-030-55231-2%7B%5C_%7D5).
- Walker, R. C. et al. (Mar. 2018). “The Structure and Dynamics of the Subparsec Jet in M87 Based on 50 VLBA Observations over 17 Years at 43 GHz”. In: *The Astrophysical Journal* 855.2, 128, p. 128. DOI: 10.3847/1538-4357/aaafcc. arXiv: 1802.06166 [astro-ph.HE].
- White, S. M. and M. R. Kundu (Oct. 1992). “Solar Observations with a Millimeter Wavelength Array”. In: *Solar Physics* 141.2, pp. 347–369. DOI: 10.1007/BF00155185.
- Whitehorn, N. et al. (Oct. 2016). “MILLIMETER TRANSIENT POINT SOURCES IN THE SPTpol 100 SQUARE DEGREE SURVEY”. In: *The Astrophysical Journal* 830.2, p. 143. ISSN: 0004-637X. DOI: 10.3847/0004-637x/830/2/143. arXiv: 1604.03507.
- Wielgus, M. et al. (Sept. 2020). “Monitoring the Morphology of M87\* in 2009-2017 with the Event Horizon Telescope”. In: *The Astrophysical Journal* 901.1, 67, p. 67. DOI: 10.3847/1538-4357/abac0d. arXiv: 2009.11842 [astro-ph.HE].
- Woody, D. P. et al. (Oct. 2004). “CARMA: a new heterogeneous millimeter-wave interferometer”. In: *Z-Spec: a broadband millimeter-wave grating spectrometer: design, construction, and first cryogenic measurements*. Ed. by C. M. Bradford et al. Vol. 5498. Society of Photo-Optical Instrumentation Engineers (SPIE) Conference Series, pp. 30–41. DOI: 10.1117/12.552446.
- Woosley, S. E. and J. S. Bloom (Sept. 2006). “The Supernova Gamma-Ray Burst Connection”. In: 44.1, pp. 507–556. DOI: 10.1146/annurev.astro.43.072103.150558. arXiv: astro-ph/0609142 [astro-ph].
- Wooten, A. and A. R. Thompson (Aug. 2009). “The Atacama Large Millimeter/Submillimeter Array”. In: *IEEE Proceedings* 97.8, pp. 1463–1471. DOI: 10.1109/JPROC.2009.2020572. arXiv: 0904.3739 [astro-ph.IM].
- Wright, M. C. et al. (2009). “Aperture Efficiency, Pointing and Primary Beam Calibration”. In: *CARMA Memos* 52.
- Yadlapalli, N., V. Ravi, and A. Y. Q. Ho (July 2022). “Models of Millimeter and Radio Emission from Interacting Supernovae”. In: *The Astrophysical Journal* 934.1, 5, p. 5. DOI: 10.3847/1538-4357/ac771f.
- Yao, Y. et al. (Aug. 2020a). “X-ray Brightening of AT2019wey”. In: *The Astronomer’s Telegram* 13932, p. 1.

- Yao, Y., D. Dong, and S. R. Kulkarni (Aug. 2020). “VLA observation of AT2019wey”. In: *The Astronomer’s Telegram* 13921, p. 1.
- Yao, Y. et al. (Nov. 2020b). “A Comprehensive X-ray Report on AT2019wey”. In: *arXiv e-prints*, arXiv:2012.00160, arXiv:2012.00160. arXiv: 2012.00160 [astro-ph.HE].
- Yao, Y. et al. (Nov. 2020c). “Multi-wavelength Observations of AT2019wey: a New Candidate Black Hole Low-mass X-Ray Binary”. In: *arXiv e-prints*, arXiv:2012.00169, arXiv:2012.00169. arXiv: 2012.00169 [astro-ph.HE].
- Yao, Y. et al. (Aug. 2022). “The X-Ray and Radio Loud Fast Blue Optical Transient AT2020mrf: Implications for an Emerging Class of Engine-driven Massive Star Explosions”. In: *The Astrophysical Journal* 934.2, 104, p. 104. DOI: 10.3847/1538-4357/ac7a41. arXiv: 2112.00751 [astro-ph.HE].
- Yuan, Q. et al. (2016). “Catching jetted tidal disruption events early in millimetre”. In: *Monthly Notices of the Royal Astronomical Society* 461.3, pp. 3375–3384. ISSN: 13652966. DOI: 10.1093/mnras/stw1543. arXiv: 1606.06830. URL: <https://academic.oup.com/mnras/article/461/3/3375/2608704>.
- Zauderer, B. A. et al. (Aug. 2011). “Birth of a relativistic outflow in the unusual  $\gamma$ -ray transient Swift J164449.3+573451”. In: *Nature* 476.7361, pp. 425–428. DOI: 10.1038/nature10366. arXiv: 1106.3568 [astro-ph.HE].

*Appendix A***SPRITE USER MANUAL****A.1 Introduction****Overview of SPRITE**

The Stokes Polarization Radio Interferometer for Time Domain Experiments (SPRITE) is, at the time of this document, a two element interferometer located at the Owens Valley Radio Observatory (OVRO). The scientific goal of SPRITE is to observe millimeter emission from high-energy and transient sources, building up well-sampled light curves over time to study variability. SPRITE is very fortunate to make use of two 10.4 m Leighton antennas (Leighton, 1977). These antennas were used as part of the Combined Array for Research in Millimeter-wave Astronomy (CARMA; Woody et al., 2004). When CARMA was decommissioned they were returned from the White Mountains back down to OVRO, where they now sit on the east-west arm of the tee. The two antennas used for SPRITE are numbered 1 and 2 - we call them "C1" and "C2" as that's how they were referred to at CARMA and this reflects how their computers are named as well. This document will cover all the basic functions required for collecting data successfully with SPRITE.

**List of Computers and Devices**

To maintain the security of these computers, to access any of these computers listed below, you must either be on the OVRO network or tunnel through the OVRO network. Please contact Rick Hobbs to ensure that your ssh key is added to be able to login to the OVRO network. Then, you can set up a tunnel within your ssh config file to handle logins to all of the below computers. It should be noted that any of these computers can be accessed using any other computer on the OVRO network! Once you have access to the OVRO network, you can login to it (or tunnel through it) using `ssh username@ssh.ovro.caltech.edu`

<b>Computer/Device Details</b>	<b>Info</b>
SPRITE computer Host name: 131.215.195.179 User name: sprite root pwd: sprite@OVRO2021	This is the main computer used to run the correlator and store/process data. It is located in the basement of the Meyer Building. Please contact Vikram Ravi to have your ssh key added if you need to access the computer.
Antenna computers Host name: c1.ovro.pvt and c2.ovro.pvt User name: comap	These computers directly control the antennas and are located in the sidecabs for the antennas. You will likely never need to use these computers directly, beyond rebooting them occasionally should issues with the control system arise.
COMAP CentOS machines Host name: comapcentos6-32- c1.ovro.pvt and comapcentos6-32- c2.ovro.pvt User name: comap	These computers run the GUI control system for the antennas and save information about the antenna states to an archive. Calculation of tilt parameters and optical pointing coefficients must be done on this computer as this requires access to the archive. Both of these computers share a single file system. Please contact either Vikram Ravi or Rick Hobbs to ensure your ssh key is added to this computer if you need access.
comap storage Host name: comap-storage User name: comap	This computer also shares a file storage system with the COMAP CentOS machines. In the event that you need to run any code (for example, python code to do tilt or pointing analysis), use this computer as you cannot use python while logged in through the CentOS machines.

<p>dsahead</p> <p>Host name: dsahead.ovro.pvt</p> <p>User name: user</p> <p>port number: 5903</p>	<p>This computer has a VNC set up on it that we use to keep the control system GUI running. As the control system has many windows, it is most convenient to not run it on a personal computer. There are two windows open on dsahead, one for C1 and one for C2 - login to the computer using port 5903 to access the VNC. If the computer has trouble gaining access to the antenna computers, try using the <code>ssh-add</code> command to add the ssh-keys to the keychain - this is often needed upon a computer restart</p>
<p>labserver2</p> <p>Host name: labserver2.ovro.pvt</p> <p>port number: 3389</p> <p>user name: Sprite</p> <p>password: sprite@OVRO</p>	<p>This computer hosts the labview interface for communicating with the antenna CAN modules. To access this computer, you should tunnel through the SPRITE machine - tunneling only through the OVRO network has been unreliable.</p> <p>Use this command: <code>ssh sprite -L localhost:3392:labserver2.ovro.pvt:3389</code> and use a remote desktop on port 3392 to access it</p>
<p>ROACH2 boards</p> <p>Host name: 192.168.10.100 and 192.168.10.101</p>	<p>The ROACH2 boards digitize and correlate the base-band signals. 192.168.10.100 is labeled high band but actually is low band while 192.168.10.101 is labeled low band but is actually high band. These are located in the rack just above the SPRITE computer</p>
<p>Red Pitaya</p> <p>Host name: rp-f07179.local</p> <p>username/pwd: root</p>	<p>The Red Pitaya controls the lobe rotator for SPRITE and is located in the sidecab of C2.</p>

## A.2 Controlling the Antennas

### COMAP Control System Usage

#### Basic Navigation

The COMAP control system can in theory be launched from any computer with a desktop - however, for convenience we will be using the VNC port 5903 on



dsahead. To launch, first open a terminal and log into the COMAP CentOS using the option `-XA` to enable both X-windows and authentication forwarding. Then, use the command `controlSystem startd` to start the control system. Then, once that is complete, use `controlSystem start viewer` to launch the GUI. Once you launch the GUI, you should see a number of individual windows pop up, as seen in Fig A.1. The following windows will be of interest to us:

- **comapViewer** This is the main window you will use to run commands to the telescope. You can use the "find" menu item to navigate to all of the below mentioned windows.
- **FrameGrabber** This feature will be useful when performing optical pointing measurements (described in a later section)
- **AzElEncoder** This window will show a plot of the current azimuth and elevation of the telescope
- **Weather** This window will show relative parameters such as humidity, wind speed, etc
- **DriveEngineTracker** This window contains a lot of very useful information. On the top, it shows today's date and the time in UTC as well as the current LST. Just underneath that it shows the expected vs actual az and el of the telescope. Then, under offsets you can see if any offsets to the pointing have

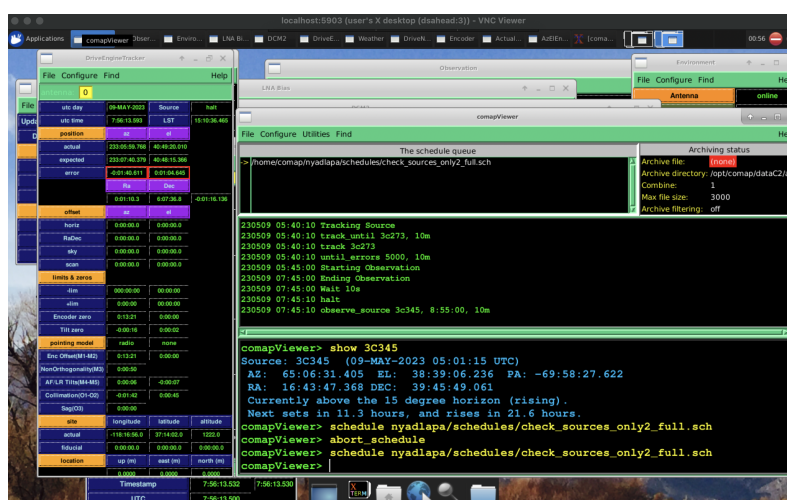


Figure A.1: A screenshot of the COMAP control system used for controlling C1 and C2

been applied. And finally you can see what the tilt zero values have been set to as well as the coefficients for both the optical and radio pointing model (to be discussed further in a later section).

Try your best not to accidentally close any of the windows. If you do, the only way to get them back is to relaunch the viewer, which is not a big deal but is a little annoying. In case you need to relaunch only the viewer, simply go to File, quit on the `comapViewer` window and then in the terminal just run `controlSystem start viewer` to relaunch all of the windows.

Next are just a few troubleshooting tips to try in case things aren't working. Sometimes when starting up the control system, you may find a message saying connection cannot be established to `c1.ovro.pvt` or `c2.ovro.pvt`. In this case, it may be that the antenna computer needs to be restarted. To do this, open a terminal on the SPRITE computer and enter `telnet powerc1.ovro.pvt` (and similar for `c2` if needed). The password is "power." You should see a screen like that in Fig A.2. Then follow these steps to power cycle the computer:

```
Enter request: 5 (password: power)
DS-RPC> off 1 (This turns off power to port 1, which is the Force
computer, which PXE boots.)
turn off pxe (Y/N)? Y
DS-RPC> on 1 (This turns on power to port 1)
turn on pxe (Y/N)? Y
```

Sometimes it requires multiple reboot cycles to finally reestablish connection to the computers. You can check the connection by using the command `ping c1.ovro.pvt` and checking to see if packets are coming in from the computer.

If you see an error that the control system "could not connect to `comapControl`," the issue is likely an error in the init files. If you go to your normal terminal window, ssh into the COMAP CentOS machine that is causing you problems and just type the command `comapControl`, it will likely tell you what line in the init file is causing the problem.

Additionally, it is very important to make sure there are not multiple instances of the control system running at once. For example, do not try to open the control system on your personal computer but also on the `dsahead` VNC for example. The communication between the antenna computer and the COMAP CentOS computers

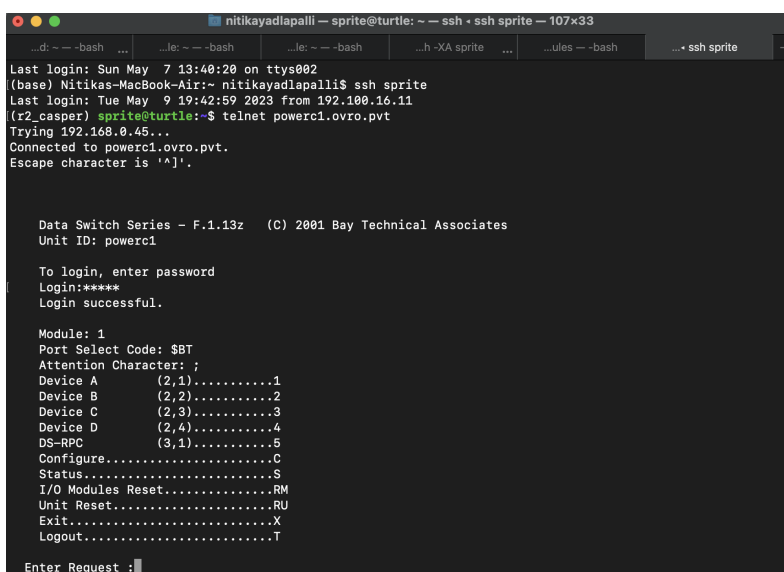
gets confused in this case and all the monitoring windows will look very bizarre. If you find that for example, the az/el encoder graph is jumping around all over the place or that telescope is not properly responding to commands, then this could be caused by multiple instances of the control system being run at once.

Sometimes you may find that the telescope drives are not responding to commands from the command line (for example, the drives are halted and refuse to stow upon command). In this case, first try to restart the control system, which often fixes the issue. If this doesn't work, it may be that the antenna drives ran into a limit switch or were not set to "remote control" mode. In this case, please contact James or Mark to check for the problem before continuing to attempt communication.

## Basic Commands

All of the commands that can be used in the control system can be found in the SPRITE SharePoint under SPRITE documents > Antenna > control\_system\_docs > commands (if you do not have access to the SPRITE sharepoint, please talk to Vikram about getting access). Here, I will just go over the more frequently used commands.

- **show**: Shows you where any source in the loaded catalogs is in the sky presently. So, if you use the command load 3C84 for example, it will show



```

nitikayadlapalli ~ sprite@turtle: ~ -- ssh - ssh sprite -- 107x33
Last login: Sun May 7 13:40:20 on ttys002
(base) Nitikas-MacBook-Air:~ nitikayadlapalli$ ssh sprite
Last login: Tue May 9 19:42:59 2023 from 192.100.16.11
(r2_casper) sprite@turtle:~$ telnet powerc1.ovro.pvt
Trying 192.168.0.45...
Connected to powerc1.ovro.pvt.
Escape character is '^]'.

Data Switch Series - F.1.13z (C) 2001 Bay Technical Associates
Unit ID: powerc1

To login, enter password
Login:*****
Login successful.

Module: 1
Port Select Code: $BT
Attention Character: ;
Device A (2,1).....1
Device B (2,2).....2
Device C (2,3).....3
Device D (2,4).....4
DS-RPC (3,1).....5
Configure.....C
Status.....S
I/O Modules Reset.....RM
Unit Reset.....RU
Exit.....X
Logout.....T

Enter Request :

```

Figure A.2: The telnet command line interface used for power cycling the antenna computers

you the RA and Dec of the source, its current azimuth and elevation, as well as its next rise and set time. This can be used for all of the planets as well as the sun and the moon.

- **track**: Allows you to track any named source. If you continue to track after the source has set, the telescope will a limit switch and stop moving; however, it is **HIGHLY** suggested that you keep track of the antenna position and not accidentally try and track a set source. So, for example, `track jupiter`
- **slew**: Slews the telescope to a specific azimuth and elevation. For example, `slew az=100, el=70`.
- **sky\_offset**: Allows you to apply small x and y offsets from wherever you are pointed. This is often useful when trying to center on a source. For example, `sky_offset x=00:00:30,y=00:00:30` will apply a 30 arcsecond offset in the positive x and y direction.
- **stow**: This will slew the telescope back to stow position.
- **halt**: This will apply the brakes on the telescope drives and prevent it from moving. When you are not observing with the telescope, you must use the `stow` and `halt` commands to move the telescope back into a safe position.
- **catalog**: Use this to upload new catalogs into the control system. For example, `catalog new_catalog.cat`
- **schedule**: Run a schedule by using `schedule sched_file.sch`
- **abort\_schedule**: Use this command to stop a schedule that is currently running.

A few other commands to update the pointing model of the telescope will be discussed in a later section.

## Writing Schedules

When writing schedules for SPRITE, you will open a file ending in the extension `.sch`. Place it in your working directory on the COMAP CentOS machine and then when you call the `schedule` command in the control system you can use the path to this schedule as the argument. When writing a new schedule file, you must begin by importing the SPRITE schedule library. To do this, make the first line of your new

schedule: import /home/comap/nyadlapa/schedules/spriteSchedLib.sch. If you've copied the `spriteSchedLib.sch` file to a new path and prefer to use that path instead, that is fine too. For normal SPRITE observing, you should only ever need the `observe_source` function, which takes three arguments: name of source, UTC start time, and duration of observation. The other two functions in `spriteSchedLib.sch` are for pointing calibration and will be discussed later. Looking at example schedules in `/home/sprite/schedules` on the SPRITE machine (or `/home/comap/nyadlapa/schedules` on the COMAP CentOS machines has all of the same content) may help.

### Reading from the COMAP Archive

The control system saves a lot of information about the state of the antenna to the archive, and we can access that data for any lengths of time that we may need. This can be very powerful, as it allows you to check the pointing of the telescope after the fact, allows you to use feature bits to define important portions of any observation, and more. A full list of all the register names that can be read from the archive is contained in the SharePoint at [SPRITE Documents > Antenna > control\\_system\\_docs > registers.yml](#). On the COMAP CentOS machines, you can use `/home/comap/nyadlapa/read_archive_test.py` to grab any data from the archive. The script needs the following arguments: the register file, the start time, the end time, the platform name for antenna you want to read data for, and the output file name. The register file is just a list of all registers you want saved to the output file. An example can be found at `/home/comap/nyadlapa/reg_test.txt`. The start and end times (in UTC) define the boundaries within which you want to read the specified register values from the register. The platform name is how the antenna is named within the archives - C1 is called "testbed" and C2 is called "C2". And finally, the output file should be an hdf5 file. So, for example, you may run `python read_archive_test.py -rf reg_test.txt -st 2023-apr-10:17:30:05 -et 2023-apr-10:20:30:05 -pl testbed -of C1_archive_data.hdf5`.

### Monitor and Control with CAN Modules

Much of the monitor and control for the antennas is done through a series of CAN modules. CAN stands for Controller Area Network, and is essentially just a protocol for sending and receiving messages between a host computer and multiple nodes in a single system. In our case, the CAN messages are sent between the antenna

computers to the CAN host computer. In short, the messages are 16 bytes long and encode information about which CAN node the message is meant for and which action is being taken. The information for how the messages are encoded and how to use the different APIs is given in the documents on the OVRO Sharepoint in projects > CANbus Documents. The document CARMA Software CANbus Documents > CANoverIP.pdf contains the relevant information about how to connect to the read and writing ports of the host computer. The folder CANbus APIs > APIS contains the information about how messages should be read and written for every API. In practice, there should be no reason to interface directly with these messages. All of the interaction with CAN nodes can be done using a LabVIEW program running on the labsrver2 computer. After logging into labsrver2 and opening up a remote desktop, open the LabVIEW program by clicking the icon called "CANbus Control Panel." When the program opens, the two tabs we are interested in will be the ones titled "CAN Hosts" and "Modules," as shown in the left and right panels, respectively, of Fig A.3. In the CAN Hosts tab, you can select which antenna to communicate with by double clicking on either C1 or C2. You will know that you are connected to the antenna if a black check mark appears next to the antenna name and the number of received packets is increasing. In the Modules tab, you will see all of the different APIs. Each API controls a different aspect of

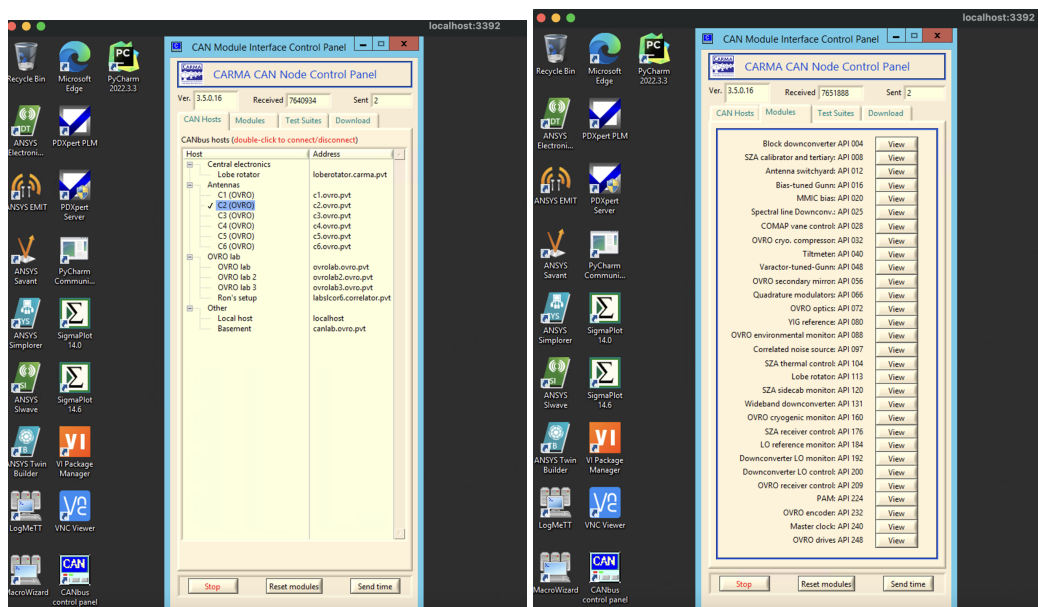


Figure A.3: LabVIEW program to interface with CAN modules that deal with monitor and control for C1 and C2

the antenna, and we only need a small subset of them for SPRITE. I will go into the usage for each relevant API as it comes up in the later sections.

In terms of troubleshooting usage of this LabVIEW interface, a few main issues may arise. First, you may find that the system is not responding to any mouse clicks. This occurs due to an undiagnosed memory leak in the program that causes it to, over time, take up large amounts of CPU power. To fix this, simply navigate to the task manager and the end the task called "CARMA CANbus control panel." Then, upon restarting the system everything should work fine.

Sometimes, you may find that upon a selecting an antenna the number of received packets does not begin to increase. This is caused by the server struggling to connect to the Internet. To fix this, navigate to the Windows control panel, and under "Network and Internet > Network and Sharing Center" find the option to "Troubleshoot problems." Run the troubleshooter to the end and open a browser and attempt to connect to any website (such as [www.google.com](http://www.google.com)). It sometimes takes multiple iterations of running the troubleshooter before the internet connection resets itself and the webpage is able to load. Once the webpage is able to load, navigate back to the LabVIEW program and you should be able to connect to the antenna computers again. We recognize this is a strange issue and to be honest, are not sure why this solution works!

### **A.3 Running the Correlator**

#### **ROACH2 Usage**

The ROACH2 boards, in short, receive analog RF signals, digitize them, correlate them, and write the output to .h5 files stored on the SPRITE computer. At present, SPRITE uses 2 ROACH2 boards, each of which can process 2 GHz of bandwidth. The SIS mixers in the receivers downconvert incoming sky signals down to the IF band of 1-9 GHz. The IF signal then passes through the second stage downconversion system (located in the Meyer building basement right near the SPRITE computer and the ROACH2 boards), which isolates the 3-5 GHz and 5-7 GHz components of that signal for both C1 and C2 and then converts them to baseband. The 3-5 GHz signals get sent to one ROACH2 while the 5-7 GHz signals get sent to the other one, hence why we call them "lowband" and "highband." Each of the ROACH2 boards contain two 5 Gsps ADCs, so in theory the ability to sample 2.5 GHz of bandwidth exists in each board; however, the correlator firmware we

use only supports 4 GHz of bandwidth. The correlator firmware was built by Jack Hickish, originally for the instrument AMI, using CASPER tools.

As soon as you login to the SPRITE computer, the conda environment `r2_casper` is already activated - this is the required environment for running the correlator. To initialize the correlator, run the following command:

```
python /home/sprite/SPRITE/sprite_correlator_sw/src
/corr_init_with_friend.py -v 1 -r 192.168.10.101 -s
192.168.10.100 -b ami_fx_sbl_wide_2014_Feb_07_1646.bof -a 50000.
```

The arguments to this script are the addresses of the 2 ROACH2 boards, the compiled firmware to program the boards with, and the accumulation time in samples. The script performs the following actions: programs the board with the specific file, calibrates the ADCs, sets the the specific accumulation length, and uses a pps signal to synchronize both boards. This last step is essential, as it ensures that all data is being captured at the exact same time. Once that step is complete, you can use the python script `/home/sprite/SPRITE/sprite_correlator_sw/src/corr_grab_h5.py` to collect data; however, you should rarely need to use this script directly. As described later, you will use a wrapper script to collect data in a more organized fashion in sync with the observing schedule.

### Red Pitaya Usage

The Red Pitaya is very small FPGA device meant to replace expensive lab equipment for simple uses. In our case, we use it to implement fringe stopping and phase switching for our baseline. The Red Pitaya in SPRITE presently is the model STEM 125-10 - this model has since stopped being available and has been replaced by the STEM 125-14. This means, all future modifications to the firmware will need adjusting to accommodate the new bit number. The 125 indicates that the sampling rate of the ADCs/DACs is 125 MHz while the 10/14 indicate the bit resolution of the ADCs/DACs. The FPGAs themselves can perform computations with a maximum resolution of 32 bits. The Red Pitaya itself is mounted on a small chassis in the sidecab of C2.

In order to program the Red Pitaya, you will need to run the function `init_rp` within `/home/sprite/SPRITE/red_pitaya_utils.py` on the SPRITE machine. This function will program the board with the default firmware file, set appropriate initial values for all registers, and write necessary information into the device's BRAM. It is necessary to use this script to re-program the board if ever there is a power outage.



Then, the functions `calc_phi_rate` and `calc_rp_error` will give you the the fringe rate for an observation of a source at a given RA/Dec at a given time and the fringe rate that is actually written to the Red Pitaya after taking into account finite bit resolution. All communication with the Red Pitaya is done using python package `casperfpga`. Ideally, aside from re-programming when necessary, there should be little need to interface directly with the Red Pitaya, as all of the necessary functions are written into the `corr_grab_h5.py` script. A diagram of the firmware as well as the compiled firmware and the Simulink file in case edits to the design ever need to be made are all contained within the directory `/home/sprite/SPRITE/firmware` on the SPRITE computer.

## **A.4 Receiver Calibration Procedures**

### **Local Oscillator Reference Signal**

SPRITE utilizes a type of receiver called an Superconductor-Insulator-Superconductor (SIS) receiver. They are called so because the first element in the receiving chain is an SIS mixer. In order to begin observations with these receivers, we will first need to ensure that the local oscillator (LO) signal to the mixer is properly set. A description and diagram of how this is done is given in Figure A.4. We will go through how to set up each of these steps of the process in practice.

To start, you must ensure that the synthesizer in the Meyer building basement that serves as the LO reference signal is set to the correct frequency. For observations at 90 GHz, we select a synthesizer frequency of 1.169610389610 GHz. This frequency should already be set and does not need adjusting. In the case of a power outage however, it may be wise to check that the frequency is still set once the synthesizer restarts.

This signal is sent over fiber to the antenna and its output power is monitored by CAN Node API 184. If you navigate to that API number in the CanBUS control panel LabVIEW program, you will see a screen like that shown in Figure A.5. In the upper left corner of this API, pay attention to the box titled "LO RF out, dBm." This value should be around 5 dBm. If it is too high or too low in only one antenna, you may try adjusting the attenuation values in the top middle section titled "LO Ref Attenuation." If the issue is affecting both antennas, you may try directly adjusting the power level on the synthesizer itself. Too little or too much power in the LO ref signal will cause difficulty in locking the oscillators or may cause poor performance of receiver tuning, as will be discussed in Section A.4. The LO ref should be fairly

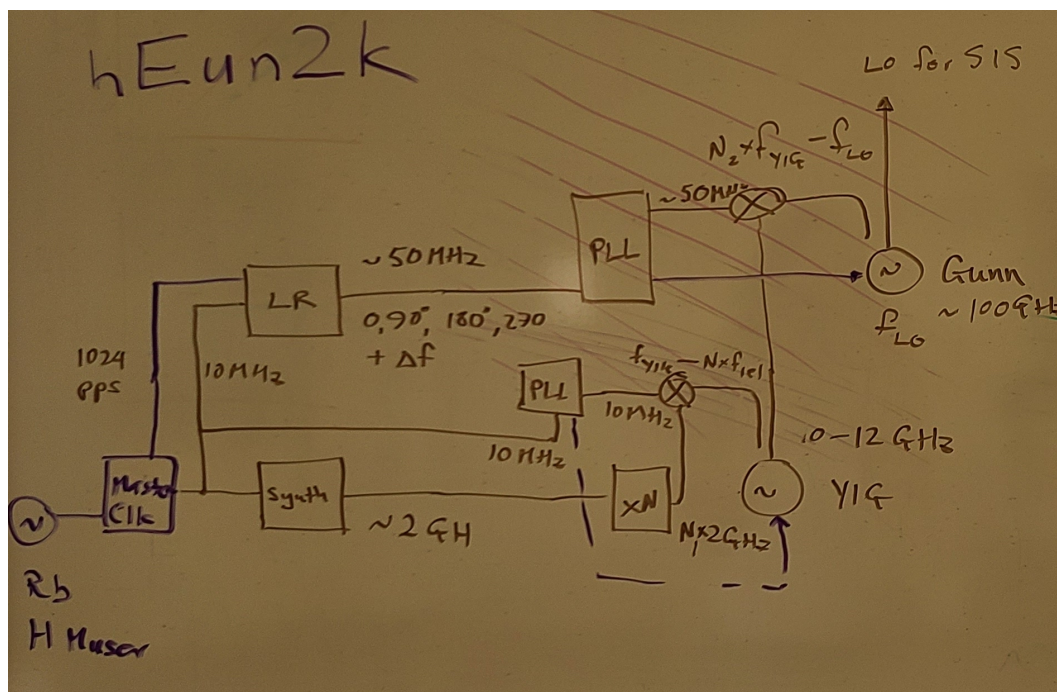


Figure A.4: Diagram describing how the LO reference signal for the SIS mixers is generated. It begins with a 10 MHz reference signal, generated by the master clock in the Meyer Building basement. Following the bottom branch of this diagram, this signal serves as the reference for a low phase noise synthesizer, also located in the Meyer building basement. The signal from this synthesizer is multiplied and a specific harmonic is selected and locked with the phase lock loop (PLL). Once the oscillator is locked, its signal can be multiplied again and mixed with the 50 MHz reference signal from the lobe rotator to serve as the input signal to the phase locking loop responsible for locking the Gunn oscillator. This final output signal from the Gunn will be used as the LO for the SIS mixer. The fact that the PLLs in both antennas are referenced by a mutual master clock ensures that the LO reference signals being generated by the SIS mixer do not have a significant phase difference between them - this prevents decoherence of the correlated visibility signals later. (Diagram drawn by James Lamb)

stable though - if you randomly see that power has dropped, try resetting the node using the "Reset Node" button on the far right and then set the power to 5 dBm.

### **Oscillator Locking**

After the LO ref frequency and power level is set, you can begin the procedure of locking both oscillators. The first oscillator that needs to be locked is the yttrium-iron-garnet (YIG) oscillator. For observations at 90 GHz, we tune the YIG to around 8.18 GHz ( $\times 7$  the LO reference frequency). As shown in Figure A.6, you can lock the YIG using CAN Node API 080. Under YIG Controls, check the box for "Lock?" and set the desired frequency in the blue box. As an aside, it should be mentioned that in the LabVIEW program, blue boxes indicate areas where the value can be set by the user whereas as cream boxes indicate the current value. In Figure A.6 for example, you can see that the user set the frequency to be 8 GHz, and the YIG was able to lock on 8.317 GHz. You can tell that the YIG was locked successfully when the green light comes up and the lock state says "Locked" under YIG Status.

After locking the YIG, you can move on to locking the higher frequency Gunn oscillator. This will be in CAN Node API 016, as shown in Fig A.7. First, ensure that the correct LO type is selected on the far right side of the panel. We want to select "3-mm OVRO." Then, check the box that says "Lock?," set the Gunn Freq to 90 GHz, and click "Set" to begin the locking. Then, if it is successful, the lock state should switch to "Locked." For both antennas, the Gunn cannot lock if the YIG isn't locked. Additionally, for C2, since the Gunn relies on the 50 MHz reference signal as well, if the Gunn is failing to lock you may want to ensure that the Red Pitaya is turned on and functioning properly.

### **Receiver Tuning**

After both of the oscillators are locked to the appropriate frequencies, the receiver can be tuned. Tuning the receiver requires setting the bias voltage across the SIS junction to the value that produces a sharply non-linear correlation between voltage and current. See Figure A.8 for a diagram and description of how the optimal bias voltage is chosen. To set the bias voltage in practice, you can use the "auto-tune" function in the LabVIEW program (see Figure A.9). In the auto-tune panel, set the frequency to the observing frequency of 90 GHz. When you click "set," it will automatically find and set the best bias voltage. To verify that the tuning was successful, you may measure a current voltage curve (IV-curve) for the mixer. To do this, look just under the graph panel where you can set the start, stop, and step

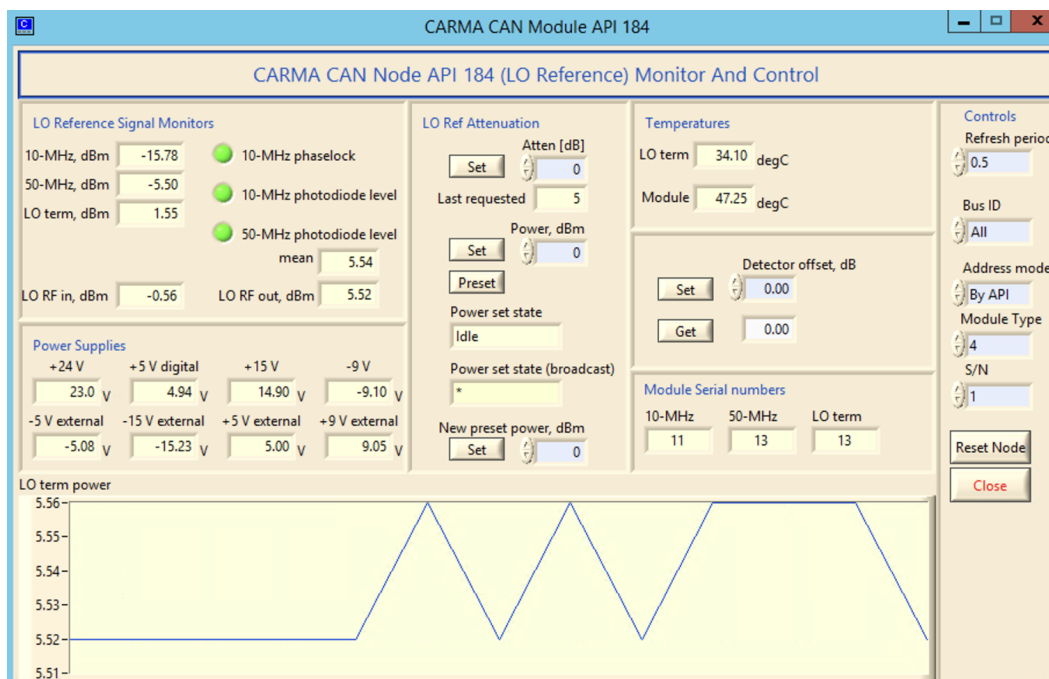


Figure A.5: CAN Node API 184, showing the status of the LO reference signal

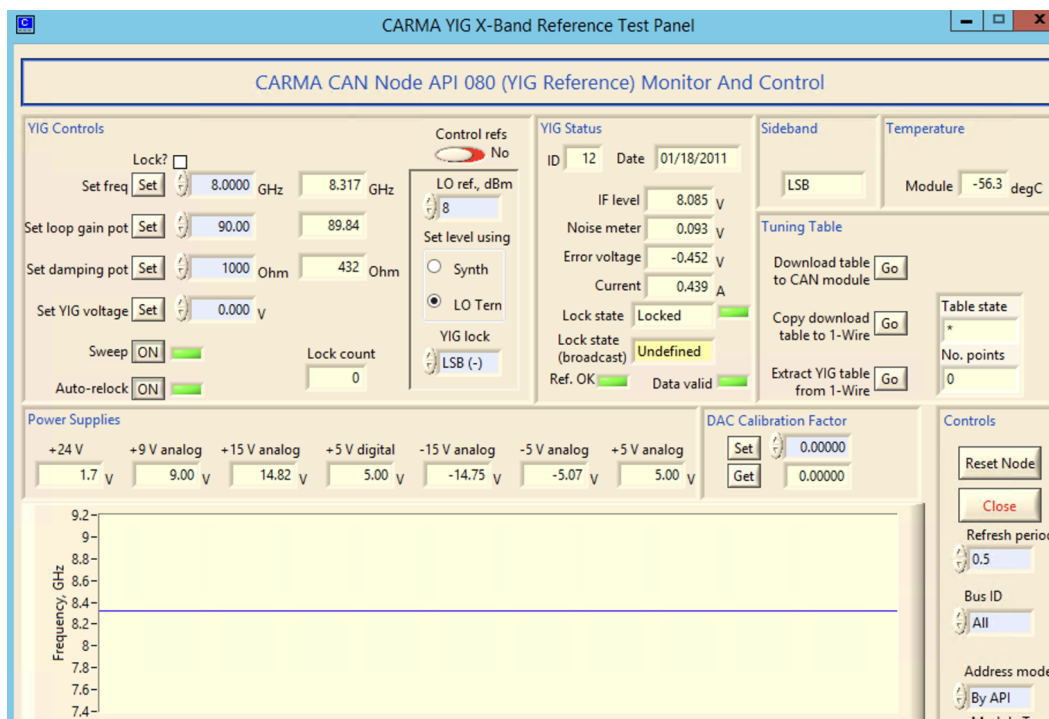


Figure A.6: CAN Node API 080, showing the status of the YIG oscillator

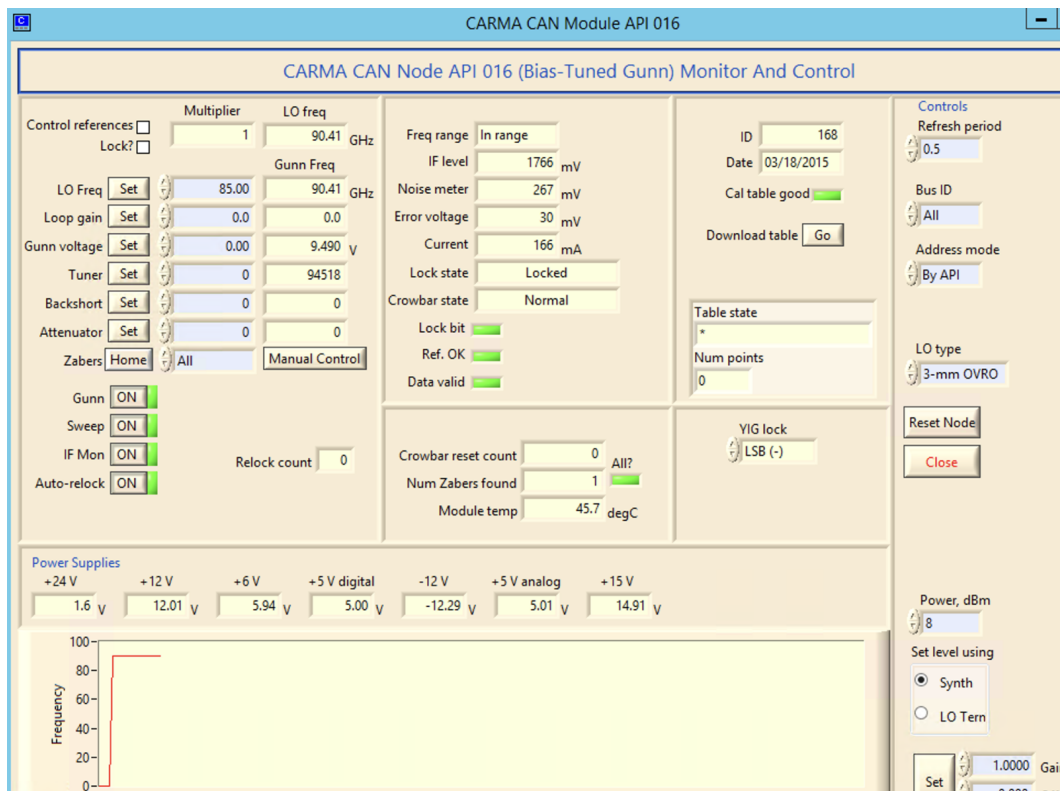


Figure A.7: CAN Node API 016, showing the status of the Gunn oscillator

size of the voltages to measure current for. Typically, we measure between 0 and 16 mV in intervals of 0.1 mV. An example of an IV-curve for a properly tuned mixer is shown in Figure A.9. We want to see a curve that has a shallow linear component just at the start, a relatively flat region up until the optimal bias voltage, and then a sharp jump with a steeply linear relationship after that. The sharp jump in current we seek occurs at the same voltage value which appears in the "Req  $V_j$ " box.

If the IV-curve does not display this shape, then there are a few things to troubleshoot which may help. First, you should check that the LO ref signal is not significantly above 5 dBm. If not, the most likely scenario is that the variable attenuator on the output of the Gunn oscillator is stuck (which happens not infrequently). This will result in too strong of an LO signal into the mixer. Typically, in the panel monitoring current, we want the "Actual  $I_j$ " value to be around  $45 \mu\text{A}$ . If you find that the current is much greater than that and the attenuation value is stuck at 100, then that indicates a stuck attenuator. To fix this, try and manually set the attenuation value to 100 and then back to 0 - this action often forces the stepper motor which controls the attenuator to rotate slightly past its stuck position and unstick itself. If this does not

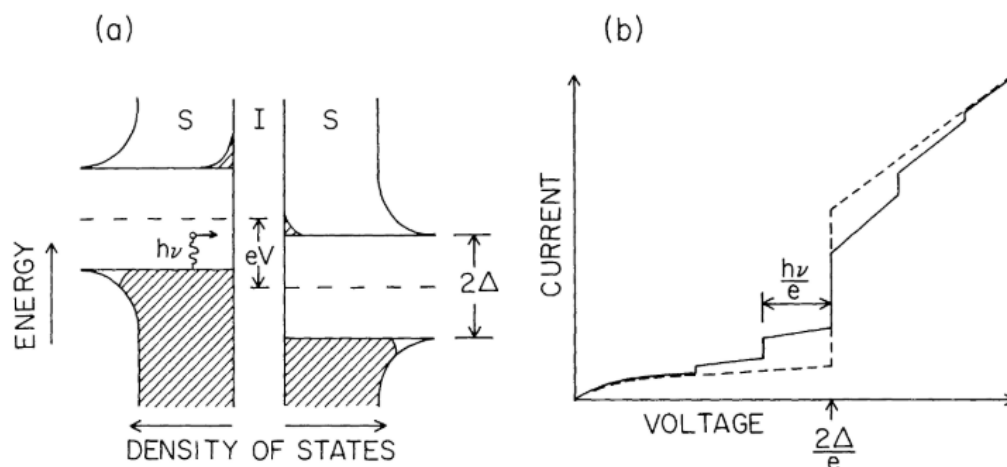


Figure A.8: A diagram, reproduced from (Phillips and Woody, 1982), of SIS mixer behavior. The left panel (a) shows a diagram of electron density of states as a function of electron energy. As characteristic of superconducting materials, there is an energy gap where the density of states is zero. The right panel (b) shows the amount of current across the junction as a function of the bias voltage. When the bias voltage is 0, the energy gaps completely overlap, so there are no empty states for electrons to tunnel to from one superconducting layer to the other. As you increase the bias voltage, there is a shallow linear relationship between voltage and current. However, as the bias voltage reaches a value such that the energy gaps are completely offset from each other, the amount of current across the junction sharply increases and the linear slope steepens. The voltage that triggers this sharp increase is the ideal bias voltage for the mixer. To see a practical example, refer to the IV curve of antenna 1 in Figure A.9.

work, then it's best to contact James or Mark at OVRO and have them take a look at the attenuator in person.

### Power Level Adjustment

Once the receiver is tuned, the final step before being ready to observe is to adjust the power level of the downconverted signal in each antenna before the signal is modulated to an optical signal to be sent over fiber back to the Meyer Building. In the antenna, there are four modes that can be observed: the sky, an ambient temperature load, a temperate controlled hot load, and a reflecting vane. We want to adjust the value of the attenuator following the SIS mixer stage such that an observation of the ambient load results in a 0.3 dBm signal. To do this, we will need the two CAN APIs shown in Figure A.10. To start, in the OVRO optics module, ensure that the "Rx select state" is set to "3-mm Rx." If not, choose that option with the "Select

Rx" box. Next, ensure that the PAM module is reading from the correct receiver - the 3 mm receivers are labeled "Rx 2," so ensure that is selected in "Select Rx." Next, under the Calibration Load in the OVRO optics module, select the calibrator named "Ambient." Once the calibrator state updates, navigate back to the PAM and set a value of 0.3 mW in the "Set IF power" box. The attenuation value should change and you should see the total power measurement in the live view of the PAM change. Then, when you change the calibration state back to sky, you should see the power in the PAM drop to something around 0.09 mW. Cloudy or rainy conditions could lead to this value being higher. However, if weather conditions are good and the sky power is still suspiciously high, you may need to go back and ensure that the oscillators are locked and the receiver is properly tuned. If those seem alright as well, you may want to check the compressor vacuum pressure as well as the temperatures in the receiver. If those are very high, the receiver will also perform poorly.

## A.5 Antenna Calibration Procedures

### Setup

For the tilt zero and optical pointing calibrations, you will need access to [springbok.caltech.edu](http://springbok.caltech.edu), which is a GitLab repository where all of the instrument

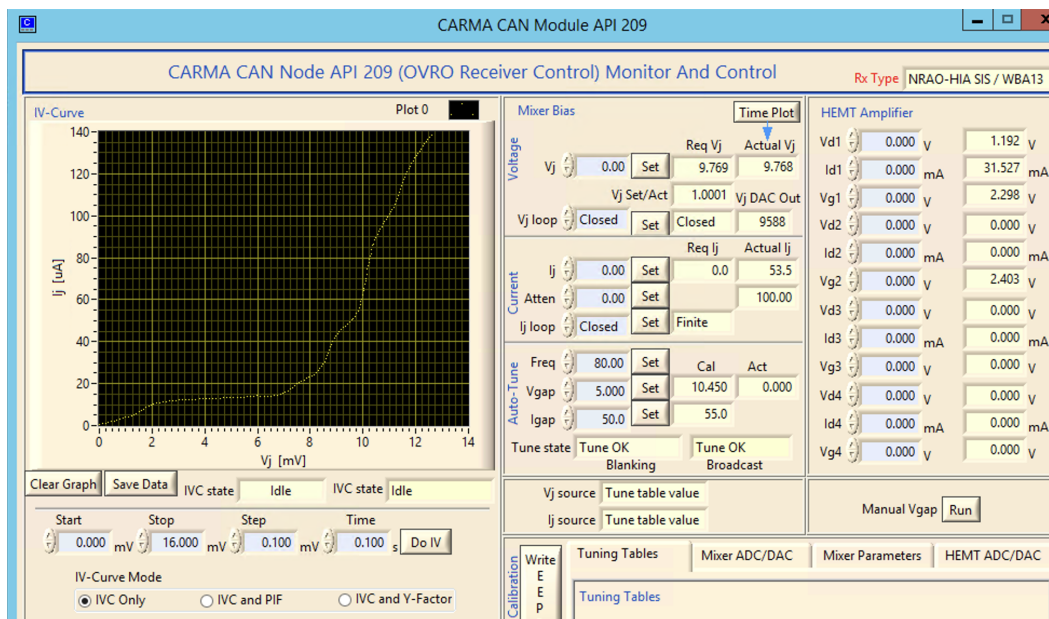


Figure A.9: CAN Node API 209, showing the options for tuning the receiver and taking an IV curve of the receiver.

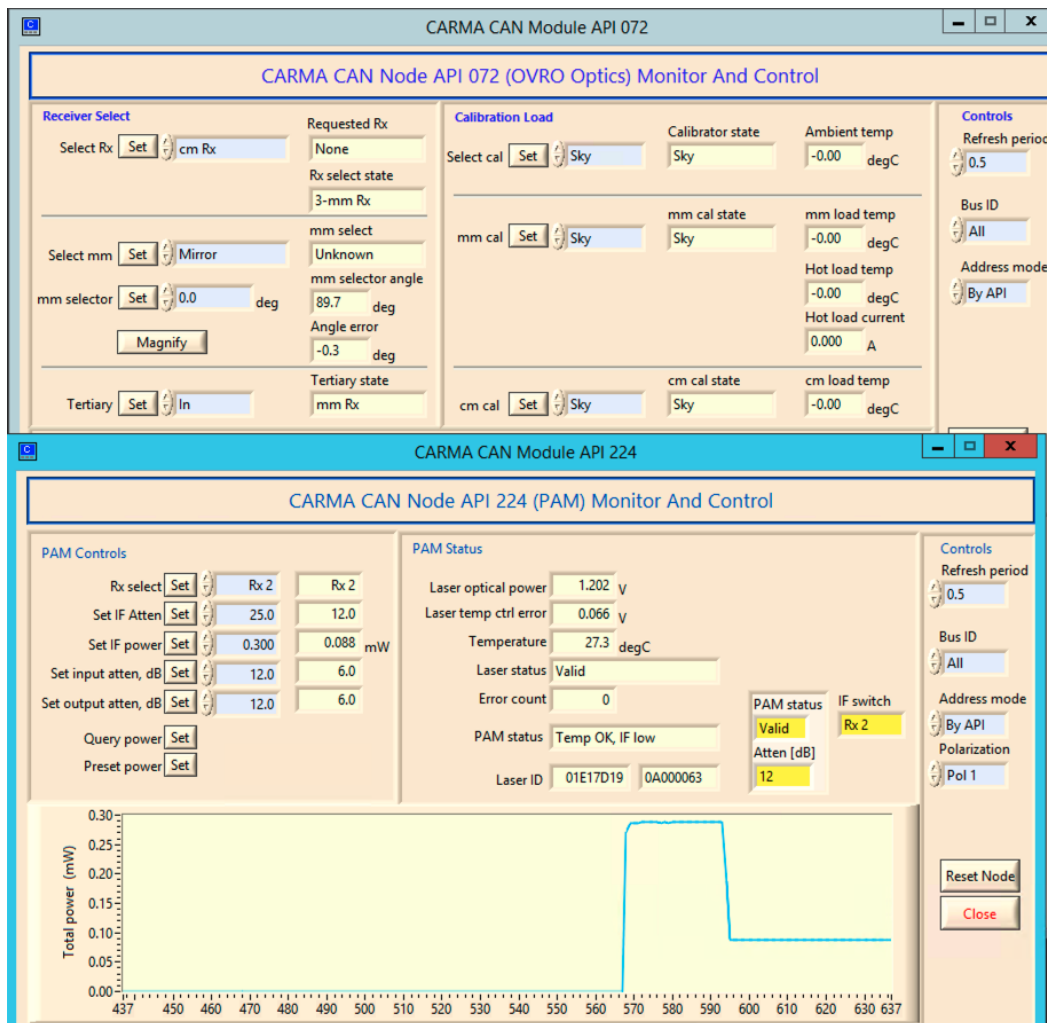


Figure A.10: CAN Node APIs 070 and 224, showing the panels for controlling the telescope optics and the PAM.

code for the COMAP project is located. We will be using scripts and procedures developed for COMAP for part of our calibration. To request access, please ask Rick Hobbs.

Additionally, to be able to update changes to tilt zero values and optical pointing coefficients, you will need to be able to make changes to the `init` files that the control system reads upon startup. To do this, please add your public ssh key to springbok using this link: <http://springbok.caltech.edu/profile/keys>. Then, in your working directory on a COMAP centOS computer, clone the repo <http://springbok.caltech.edu/comap/observing> and checkout the branch `ny/dev`. The files of interest will be `conf/comap/pointingDriveEngineC1.init` and `conf/comap/pointingDriveEngineC2.init`. You will want to make and push



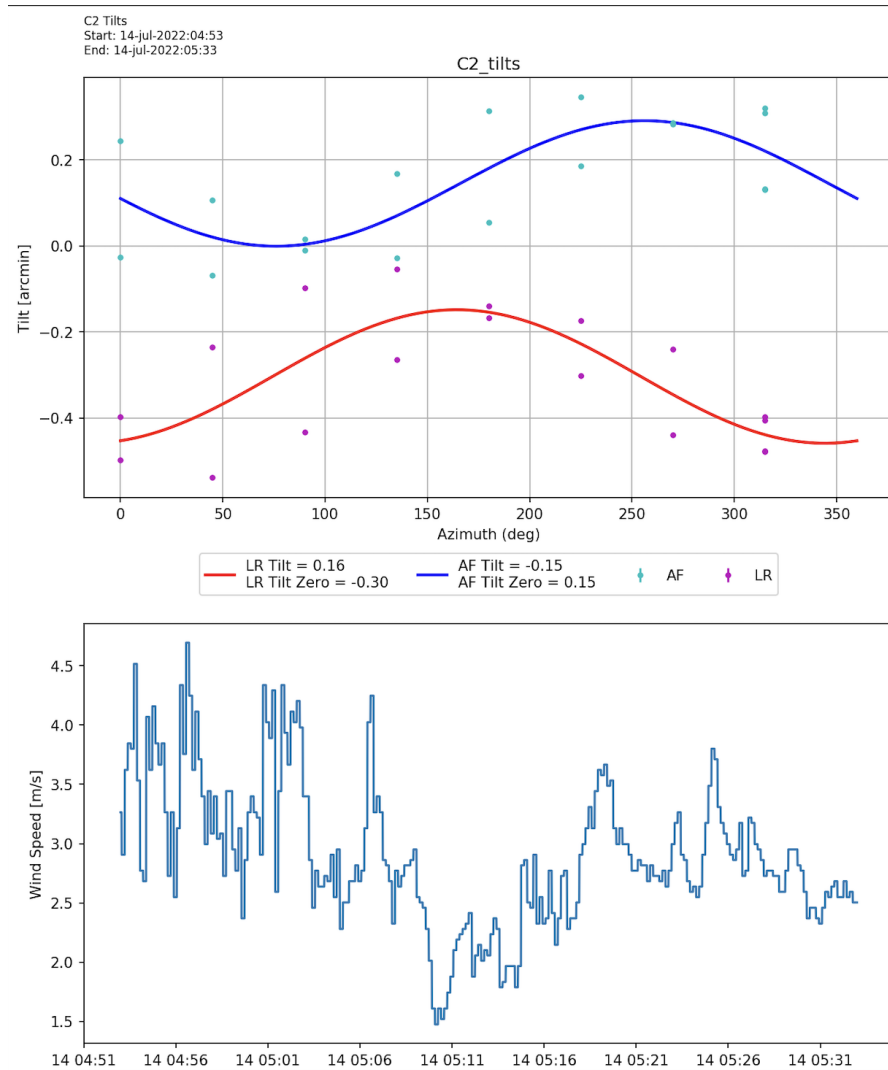


Figure A.11: An example output file from the `process_tilts.py` script

changes using the copy of the repo that is within your working directory. When you are ready for those changes to be read by the control system, go to the stable area at `/home/comap/proj/comapProjectStable/comaptcp/gcpComap/control/conf`, ensure that the branch `ny/dev` is checked out, and just pull the changes. It is VERY IMPORTANT that you never make any changes directly to the files in the stable area and that you do not modify any files besides the init files mentioned above. This is because the COMAP project shares this directory with us.

### Tilt Zeros

The first step in calibrating the antennas is setting the tilt zero values in the COMAP control system. In the base of the antennas, there exists a digital level that writes

values to the COMAP archive. These values are used for determining the tilt and tilt-zero values of the antenna base – the tilt zeros must be recorded in the control system before proceeding with the pointing model. This procedure needs to be redone quite rarely. If you haven't already, clone this gitlab repository: <http://springbok.caltech.edu/comap/comapDriveAnalysis> and switch to the branch `nyadlapa`. Alternatively, if you ever need to make changes to this code we are about to use, you could make your own branch from `nyadlapa`.

To begin, open the COMAP control system and run the schedule `tilt.sch` contained within `comapDriveAnalysis/tilt`. This schedule will rotate the telescope through a set of different azimuths, recording the digital level values at each azimuth. Make sure you record the start time and end time of the schedule. To analyze this data, login to `comap-storage` and use `comapDriveAnalysis/tilt/process_tilts.py`. This code takes four arguments: the register file, start time, end time, and platform name (see Sect. A.2 for more details). The code will create an output directory called `tiltdata` in whichever location you ran the code from, so try and be sure to not run the code within the git repo. Within `tiltdata/<platform name>` you will find a `.png` file showing a plot of the results of the tilt data as well as the wind speed with time. An example of this is shown in Figure A.11. If you see that the wind speed was higher than around 5 m/s, you may want to retry taking this data at a later date, as the wind strongly affects the measurements. The values we care about are "LR Tilt Zero" and "AF Tilt Zero." The control system command for setting the tilt zero values is `tilts 0,<LR tilt zero in hh:mm:ss>,<AF tilt zero in hh:mm:ss>`. You will want to add these commands to the `init` script for each antenna.

### Optical Pointing

The first step in correcting the pointing of the telescopes is done by using a small optical camera mounted underneath the antenna surface. This camera looks through a small hole in the antenna surface and can be used to center on the locations of bright stars. The brightest stars can be seen during the day and most other reasonably bright stars can be seen starting around twilight. In short, you will use this camera to image several bright stars at different azimuths and elevations and measure their offsets from their expected positions. From there, terms describing the alignment of the mount and the optical camera aperture are calculated by analyzing the offset data and the corrections are loaded into the control system.

To begin, you may want to look over the memo titled "Pointing the Leighton Antennas" written by Dave Woody. You can find it in the SPRITE SharePoint under the Antenna folder. On page 3 of this memo, you will see the equations outlining the pointing model as well as the 8 coefficients of the model,  $M_1$  through  $M_5$  and  $A_1$  through  $A_3$ . The  $M$  coefficients describe terms related to the antenna mount (so will be shared by the optical and radio pointing models) while the  $A$  terms are related to the telescope aperture (so will be different for optical and radio pointing models). In order to obtain the coefficients, we first need to measure the sky offsets required to center stars in our optical camera for stars at a variety of azimuths and elevations. To start taking data, first open the lens cap on the camera by using the command `setCameraState on` in the `comapViewer` window. Additionally, ensure that we are using the optical model by running the command `model optical, ptel=0` in the `comapViewer` window. Next, start up the frame grabber for optical camera by selecting `Utilities > Frame Grabber` on the `comapViewer` window of the control system. A set of windows like those shown in Figure A.12 should pop up, but the image box will be totally black. Once you slew to a star, you will want to click "Next Frame" many times until an image of the star pops up. It often takes 5-10 clicks to get the image to pop up, so don't be discouraged if it takes a bit. Once the image pops up, you should be able to clearly see the star in the frame. To record information about its offset, use "Find Peak" and then "Move" to calculate and apply the offset. You will then need to click "Next Frame" to see the results of the move. Do this iteratively until the star is centered on the crosshairs. When the star is center click the long bar at the bottom that says "Press here when the star is centered in the image." DO NOT PRESS CENTER - it is in red for a reason (which is unknown to me, but surely a good reason?). In order to observe a range of azimuths and elevations, you may want to observe the same sources but separated by many hours or just visit a large number of sources in one shorter sitting - either way is fine. A reference for bright stars and their names in the control system as well as their magnitudes can be found at:

`/home/comap/proj/comapProjectStable/comaptcp/gcpComap/control/ephem/stars.cat` on the COMAP CentOS machines. In order to ensure a good fit to the coefficients, you'll want a minimum of a ten measurements; however, more is of course better.

Once you feel you've collected data on enough stars, quit the frame grabber, set the camera state to off, and stow the telescope. Then, log into `comap-storage` to use the script `comapDriveAnalysis/pointing/process_pointing_v2.py` to

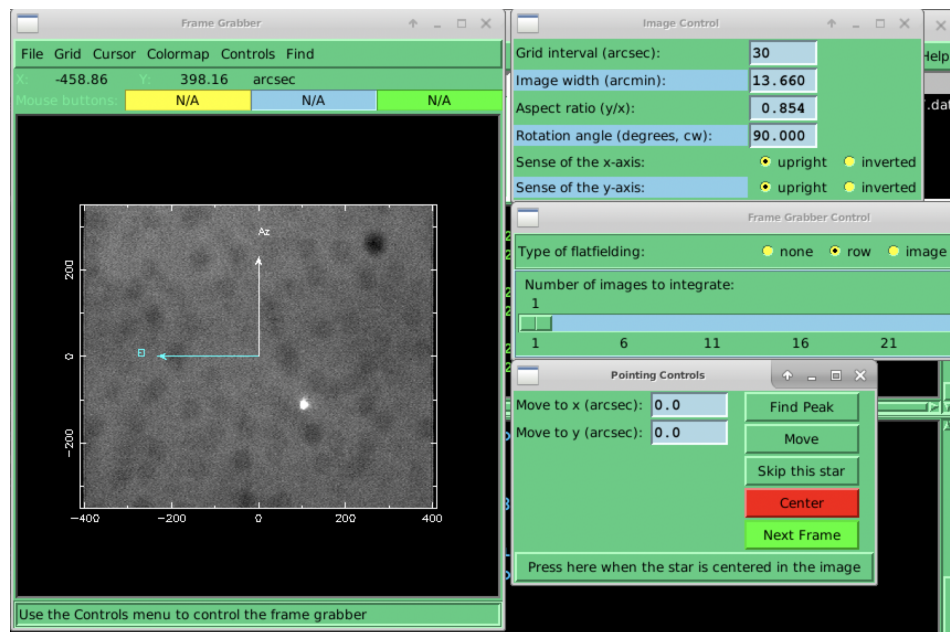


Figure A.12: Frame Grabber utility in COMAP control system

fit for the coefficients. Similar to the analyze tilt scripts, this code also takes four arguments: the register file, start time, end time, and platform name. You'll want to look at the .txt file that was created from this script and scroll down to where it displays "New pointing constants in arcmin." We want to enter the Case A coefficients into the control system. Note that instead of using "A," this code uses "O" to denote the aperture coefficients. You may also notice that one value is given for O2+M2 - in reality, we only need to set one of these coefficients and the other can be zero. You can update the mount coefficients using the command `setPointingMountCoeff M1,M2,M3,M4,M5` in the control system. Note that for C2, M2 should equal zero; however, for C1, due to some preset encoder offsets, M2 is actually 57'. To update the optical aperture coefficients, use the command `setPointingApertureCoeff optical,01,02,03`. Make sure to add these updates to the init script for each antenna.

### Radio Pointing

After computing the mount and optical aperture coefficients, we can move to computing the radio aperture coefficients. As mentioned previously, we do not need to recalculate the mount coefficients, just the aperture coefficients. To do this, we will track a source, step the antenna through different x- and y- offsets, and measure the autocorrelation power for that antenna recorded by the correlator. The x- and

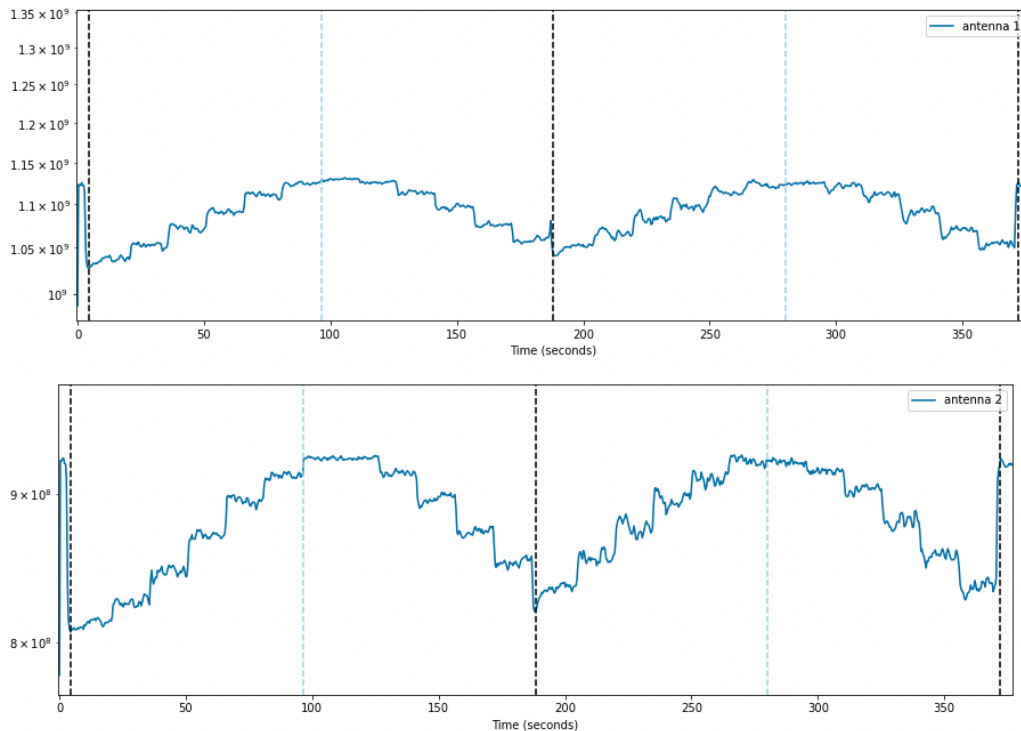


Figure A.13: Recorded power in the correlator vs time as each antenna sweeps through offsets in increments of 10 arcseconds between -1 and 1 arcminute across the disk of Jupiter. The black dotted lines demarcate the transition between stepping through offsets in  $x$  and offsets in  $y$ . The light blue dotted lines represent times where the telescope is passing through zero offsets. The top panel represents antenna 1 and the bottom panel represents antenna 2.

$y$ - offset for which the power is maximized will be the radio pointing offset of the antenna.

First, ensure that the receiving system is properly tuned/calibrated by following the steps outlined in sections A.4, A.4, and A.4. Then, ensure that the telescope is using the radio model by using the command `model radio` in the `comapViewer` window. This will load the current radio pointing coefficients. To do this measurements, you will need to pick a large, bright, and resolved source to track - good options include Jupiter, Saturn, and the moon.

If you do not want to run the correlator, you can see a live monitor of the radio power through the antenna using the PAM (API 224) in the LabVIEW program. Then, once you are tracking a source, use the `sky_offset` function in the COMAP control system to apply small incremental offsets (steps of 10-30 arcseconds depending on how large you think your error is) in the  $x$ - and  $y$ - directions independently out

to a reasonable distance beyond the edge of the source and keep track of how the measured power changes with position. From here you may get a rough estimate of what the offset is by seeing at which x- and y-offsets the measured power is maximized.

To do this in a more automated way, you may write a schedule using the `pointing_scan` function defined within `spriteSchedLib.sch`. This function inputs the name of source, the start time of the scan, the total amount of offset you want to explore, and the incremental step sizes to try. You can see an example at:

`/home/sprite/schedules/single_dish_pointing.sch`. Then, use this schedule alongside the code that runs the correlator (described in section A.6) to record data. Once the data is recorded, you may use the notebook

`/home/sprite/nitika/notebooks/single_dish_radio_pointing.ipynb` to analyze the output. The only thing you should need to edit in this notebook is the name of the input file in the top cell. This notebook reads the times from the correlator output file and gets a record of the telescope's x- and y-offsets during those times from the COMAP archive. Then, it compares the measured brightness with time to the offsets with time and calculates the telescope offset in each direction. The plot in Figure A.13 shows the power in the correlator as a function of time as one of these scans is taking place.

To refine the pointing model, you can use interferometric pointing by keeping one antenna fixed on the source center and performing a five-point scan with the other (repeating the procedure for both antennas). Within the SPRITE schedule library, the five-point scan can be achieved with the function `five_point_scan` which takes 3 inputs: the name of the source, the start time of the observation, and offset to try. The function will then slew the telescope by the offset amount in the +x, -x, +y, -y directions, leaving 90 seconds in between scans. You will need to use the correlator to record this data, but then a simple fit to the five points to find the location of the peak brightness should yield a finer estimate of the pointing coefficients.

Whichever methods you use to measure the offsets, make sure to update the measured coefficients in the `init` scripts. The amount of x-offset equals the change in O1, whereas the amount of y-offset equals the change in O2. O3 should be left as zero for the radio pointing coefficients. You will need to add these values to the current radio pointing coefficients to obtain the new ones. The command to set them is `setPointingApertureCoeff radio, O1, O2, 0`.

## A.6 Setting up an Observation

Once you have ensured that all the necessary calibration procedures from sections A.4 and A.5 are completed, you can move on to taking data from astronomical sources. To do this, we have developed a set of tools that will help you write schedules and coordinate those schedules between the antenna and the correlator. Much of the code necessary for conducting observations is in a git repository (<https://github.com/nitikayad96/SPRITE>), which is cloned on the SPRITE computer at `/home/sprite/SPRITE`.

### Source Catalog

All of the sources that SPRITE may be interested in observing should be maintained in the SPRITE source catalogs. These catalogs are located in two locations: on the SPRITE computer at `/home/sprite/SPRITE/catalog_files/` and on the COMAP CentOS computers at `/home/comap/sprite_catalog_files/`. If you want to add any new sources, either append them to the end of the appropriate existing catalog or just create a new catalog file in that same directory. Each catalog file will need to have a comment specifying the catalog type at the top, either `calibrator` or `science`. It's important that anytime you make changes to the catalog files, that you sync the changes between the SPRITE and COMAP CentOS computers. The format of adding new sources is `epoch source_name RA Dec`. Whatever name you write in this catalog is the name that will be read by the COMAP control system. Other catalogs are loaded into the control system as well, including planets and bright stars, but these cannot be edited by us. Anytime you modify a catalog file, you will need to use the `catalog` function within the COMAP control system to ensure the updates are loaded in for use in subsequent schedules.

### Tools for Writing a Schedule

As introduced in section A.2, schedule files are text files that end in `.sch` extensions and can be passed to the COMAP control system to communicate to the antennas when and how long they should be pointing at different sources. Begin the file by adding the line

```
import /home/comap/nyadlapa/schedules/spriteSchedLib.sch
```

to the top of the schedule. The file `spriteSchedLib.sch` contains a set of functions written specifically for running SPRITE. Of course, if you have copies of either this or the catalog file in a different location on the COMAP CentOS computers, you can change those opening two lines to reflect those new file paths.

For schedules that help you determine pointing offsets, you can use the function `pointing_scan` for single dish pointing or `five_point_scan` for interferometric pointing. To write a normal schedule for observing a list of sources that entails slewing to different sources and tracking them for fixed amounts of time, we will use the function `observe_source`. The syntax for using this function is `observe_source source name, start time, observation duration`. The source name must reflect something in a catalog loaded into the control system and is case sensitive. The start time is the UTC time that you want the observation to begin and is in the format `HH:MM:SS`. The duration represents how long the antenna should track this source for and accepts time in seconds, minutes, or hours. So, for example, the following values are all equivalent: `3600s`, `60m`, or `1h`. Each source should be specified in a new line. Additionally, after the import statement but before any observe source statements, you will need to add a reference date for the observation in this format: `# reference date: YYYY-MM-DD`. This will be the date that the schedule was written - for running the same schedule on future days, the SPRITE codebase can then read this date and update all of the observing times accordingly such that for each day the sources are observed at the same altitudes/azimuths. You can see examples of schedules within `/home/sprite/schedules/` on the SPRITE computer.

### **Full Correlator Code**

To run the correlator for normal observing, we use the following python script located on the SPRITE computer: `/home/sprite/SPRITE/get_correlator_data.py`. This code takes three required and three optional arguments. The required arguments are: the schedule file that will be running on the COMAP control system, the path to where the catalog files directory, and the output directory of where `.hdf5` files from the correlator will be stored. The convention we presently use to label correlator files is with 6 digit numbers, incrementing by 1 for each new observation (for example, at `/mnt/data/000042`). The code will not allow you to write new observation files into a pre-existing non-empty directory. The optional arguments can be used to specify not to include routine parts of the observing sequence, like switching the ambient load into place to measure the system temperature, checking that the altitudes of all sources to make sure they are always above the  $15^\circ$  horizon, and automatically adding gain calibrator scans for each science target. Assuming you do not use these optional arguments at all, the full correlator code will perform the following functions.



First, it will check that the given output directory is not currently in use for another observation. Then, it will use the `get_full_schedule` within the `sprite_utils` library to create the full observing schedule given an input schedule file. The first step of this function is to take the initial `.sched`, advance the times based on the reference date in the file, rearrange the sources so that the schedule may start based on the current time, and ensure that all of the sources are risen and none of the observations are overlapping. The initial schedule inputted by the observer should have scans of the following types: science targets, flux calibration, and bandpass calibration. The `get_full_schedule` will identify the science sources, and add gain calibration scans every five minutes (unless you use the option to not add any gain calibration scans!). For each source, this function will also calculate the appropriate phase rate to set within the Red Pitaya. Then, this information all gets passed along to the `corr_grab_h5` script (discussed in Section A.3) which sets up the serial connection to the ROACH2 boards and begins the data acquisition from the correlator, using the source information to populate the header information for each output file. Both ROACH2 will run in parallel by calling separate processes on the SPRITE computer.

A third process is called on the SPRITE computer as well which controls moving the ambient load in and out of the receiver path at intervals of 15 seconds for every 5 minutes of observation per source. This is done by sending a message to through socket connections to C1 and C2 via the appropriate port numbers for CAN communication. CAN messages are 16 bytes long, and contain information about whether we are writing or writing to the node, the CAN ID which specifies element of the system is being communicated to, the message size, and the message itself. For, for example, this is how you would construct a message for moving the ambient load into the view of the receiver:

Byte 1	Byte 2	Byte 3	Byte 4	Byte 5	Byte 6	Byte 7	Byte 8
MODE	CANId/ AC (Byte 1)	CANId/ AC (Byte 2)	CANId/ AC (Byte 3)	CANId/ AC (Byte 4)	BusId/ Filter (Byte 1)	BusId/ Filter (Byte 2)	Msg Size (0 – 8)
Byte 9	Byte 10	Byte 11	Byte 12	Byte 13	Byte 14	Byte 15	Byte 16
MsgData/ AM (Byte 1)	MsgData/ AM (Byte 2)	MsgData/ AM (Byte 3)	MsgData/ AM (Byte 4)	MsgData (Byte 5)	MsgData (Byte 6)	MsgData (Byte 7)	MsgData (Byte 8)

Figure A.14: Message structure for CAN over IP communication

31	30	29	28	27	26	25	24	23	22	21	20	19	18	17	16	15	14	13	12	11	10	9	8	7	6	5	4	3	2	1	0			
0	0	0	0	0					0x081										72															
			0	0	0	0	1	0	0	0	0	0	0	1	0	1	0	0	1	0	0	0	0	0	0	0	0	0	0	0	0	0	1	
0x02				0x02				0x90				0x01																						
CANId (Byte4)				CANId (Byte3)				CANId (Byte2)				CANId (Byte1)																						

Figure A.15: Message structure for CAN ID bytes, using an example of controlling the ambient load of the antenna.

Referencing, Figure A.14, you need to populate the data for each of the 16 bytes to send a message. Byte 1 represents the the message mode - set this to 2 to write a message to the CAN node. Bytes 2-5 represents the CANId, which is further divided into a 29 bit message that contains information regarding where the message is going. Referencing Figure A.15, since each byte must contain 8 bits, we simply set of the first 3 bits of the message to 0. Bit 28 refers to the "host process" and should be set to 0, indicating that the message should be sent to the CAN node and not stopped at the host computer. Bit 27 refers to the address mode, and should be set to 0 to reference the address by its API number. Bits 26-17 refer to the the message type while bits 16-9 refer to the API number. Referencing the documents contained in `CANbus APIs > APIS`, or ust checking the API number on the LabView program, you'll see that the API number for OVRO Optics Control is 072. Referencing the documentation for API 72, the message type for the calibration load command is 0x081. Bits 08-00 are the node location code, and should be set to 1.

Moving on to the full message, bytes 6-7 reference the bus ID of the messages - if you do not know which bus number specific nodes are located on, just use 0xFF for both of these bytes. Byte 8 specifies the message size, and can be between 0-8. Looking at the calibration load documentation, only the first byte is used, so we can set byte 8 to 1. Finally, putting the ambient load in place requires setting the byte to 0x01, so we set that as byte 9, and leave the other bytes as 0. Then, we produce the final 16 byte message for sending the command to move the ambient load into place: `0201029001ffff01010000000000000000`. The function `switch_cal_load` within `sprite_utils` shows how the socket connections with the CAN host are established and how messages are sent.

These three processes in `get_correlator_data` are repeated for each source in the full schedule until the observation is complete. In order to run an observation, you need to both run the correlator code on the SPRITE computer and run the corresponding schedules on both antenna 1 and antenna 2. It should be noted that there is no communication between the correlator and the antennas - all of the

coordination is done by specifying the UTC times that each observation should start. Thus, if one of the antennas does not slew to the source before the specified UTC time, the antenna schedule will become desynchronized from the correlator, and the rest of the correlated data will be meaningless. So, it is very important to ensure that you leave ample time (at least 5 minutes) between starting the schedule and the time the first source is supposed to be observed. If you suspect that something was wrong in the antenna positions during your observation, you can get the antenna positions as a function of time from the COMAP archive using the procedures described in Section A.2.

### **A.7 Reducing Observations**

Once you have a completed observation, you can use the `/home/sprite/SPRITE/reduce_sequence.py` script to reduce the observation. This script has three modes of running: `reduce`, `flag`, or `catalog`. The `reduce` mode will process the entire sequence. The applied calibrations are: sideband separation of the data, dividing out a set of model visibilities containing the correct lobe rotation rate and geometric delay corrections, removing cable delay, and applying a spectral system temperature correction. Following this, an average bandpass is derived from the bandpass calibrator and the correction is applied to all sources. Then, using scans on Uranus as flux calibration, the flux solution is derived using a model for the brightness temperature of Uranus (which is a function of its ephemeris) and the solution is applied to all scans. Finally, the gains of the science targets are corrected using scans on gain calibrators. The final output of this script will be a list of calibrated data files for each track in `.npz` format.

You can also use the flagging mode of this script to flag single scans that you are know are bad quality. The `catalog` mode will show a list of what scans are present in a single observation.

### **A.8 Putting It All Together: Observing Checklist**

With the information in this cookbook, you should have all of the tools to run a full observing schedule with SPRITE! To conclude, here are a list of steps that you can refer to that should be performed to run a schedule:

1. Check the weather conditions. If it is overcast, raining, or very windy, please do not observe and ensure the antennas are stowed and halted.

2. Assuming good weather, open the LabView program that monitors and controls data from the CAN modules.
3. Check that the power levels in the LO reference signal are about 5 dBm in both antennas and make adjustments if necessary.
4. Ensure that the YIG oscillator is locked in both antennas.
5. Ensure that the Gunn oscillator is locked in both antennas.
6. Check the receiver tuning in both antennas by plotting IV curves. Retune the receivers if necessary.
7. Ensure that the power level when observing the ambient load is around 0.3 dBm in both antennas. Ensure that the blank sky level is around *sim*0.09 mW.
8. Though most likely not necessary, calculate and update tilt zero and pointing coefficients if needed.
9. Write a schedule for up to 24 hours of observations.
10. Set the correlator to run using the created schedule.
11. Run the schedule in the control system of both antennas and ensure that the antennas are not going to miss the start UTC time of the first source.
12. Run the data reduction script to create calibrated data products that can be used for science analysis.

*Appendix B***EHT SYNTHETIC DATA GENERATION TUTORIAL**

Generation of synthetic data is essential for testing and validation of imaging algorithms used for analysis of Event Horizon Telescope (EHT) data. This appendix is meant to guide those wishing to generate new sets of synthetic data through the process of creating it. The specific examples shown in this appendix will use code written for generation of synthetic data based on 2017 and 2018 observations of M87; however, modifying the code to accommodate future years of data or include model types and formats not yet included should be fairly straightforward. The code discussed is located in the following Github repository: <https://github.com/nitikayad96/M872018synthdatagen>. Due to data confidentiality, this repository is private - should you need access to this code, please contact Nitika to be added as a collaborator. To use this code, you must have `eht-imaging` installed on your computer.

To begin, the process in which synthetic data is generated is largely very similar for both 2017 and 2018. The main input parameters needed are: a `.uvfits` file for the observation you are trying to simulate uv-coverage, gain behavior of each station, and the models you are trying to simulate observations for. For specifying the `.uvfits` files, you can create a list of input observation files in the variable called `obs_list`. Each file in the list will have synthetic data generated based on it for all the specified models. The list of models you want the synthetic data to represent is specified in the variable called `synth_list`. If you would like to use a predefined geometric model, the options are: `cres`, `ecres`, `ring`, `disk`, `dblsrc`, `point+disk`, `disk`, `point+edisk`. The definitions of these models are given within the function `add_synth`. The `add_synth` function also accepts files ending in `.fits` or `.txt`, so you may pass custom created models (such as GRMHD models) to the code. The flux of geometric models must be defined using the variable `F_cmpt`. This value is also used to rescale the flux values per pixel for models given in `.txt` format. For `.fits` input model files, the compact flux will be that defined in the input file. Some of the predefined geometric models also required a radius, which is usually chosen each year based on the pre-imaging size constraints of M87. This value is set in the variable `r_cmpt`. The variable `F_jet` defines the flux density of the large scale jet that is added to the model, in addition to

the compact flux component. Because of the addition of the large scale jet, the size of the ground truth images created from this script have a field of view of  $2000 \mu\text{as}$ . The large field of view also prevents spurious high-frequency features from arising in the uv-data.

For defining the gain behaviour of the telescope, there are two methods that may be used. In general, the telescope gains are defined by two values: the gain offset and the gain perturbation. The gain offset defines how much the station gain is offset from 1, and is constant across scans. The gain perturbation, on the other hand, defines how much the gain varies between scans. In the synthetic data code, there are two values defined for each station:  $g_{\text{offset}}$  and  $g_p$ . These do not define a fixed value, but define a distribution from which a value can randomly be chosen. So, to choose the fixed gain offset, a random value is selected from the Gaussian distribution with  $\mu = 1$ ,  $\sigma = g_{\text{offset}}$ . Then, the amount of the gain is perturbed from that value is chosen per scan from a Gaussian distribution with  $\mu = 0$ ,  $\sigma = g_p$ . This means, running the data generation code multiple times will not recreate the same realization of gains. For the 2017 data, reproducing the same data was done by initializing the code with a seed value. For the 2018 synthetic data generation however, we first selected a realization of the gains that felt suitable and saved it to a `caltable`. In `eht-imaging`, a `caltable` is just a text file that contains information about the gain per scan per station. That is why in the 2018 data generation script, you are asked to provide a path to the `caltable`, through the variable `caltable_dir`, along with the input `.uvfits` file. It is important when specifying these that the date of the observations for which the `caltable` was created for matches the date of the `.uvfits` file being used to simulate the observations. By default, the synthetic data generation code also adds thermal noise, field rotation errors, and polarization leakage. These options can be modified however, using the list of terms starting with `add_th_noise`.

Lastly, ensure that you set the output directory of where the generated data should be saved. In the 2017 script, the variable is called `save_path` while in the 2018 script it is called `outputdir`. Once these are all set, run the script simply by using the syntax `python gendata2017.py` or `python gendata2018_with_inputcaltable.py`. The output data from this will include all the specified noise and will **not** be network calibrated (`netcal`). Should you need network calibrated synthetic data, refer to the `ipython` notebook titled `netcal_syntheticdata`. In the second cell, you will need to modify the variables `indir`, `obsfiles`, and `outdir` to set the in-

put directory of non-netcal data, the uvfits M87 observations used to make the non-netcal data, and output directory the netcal data should be saved to. After making those modifications, simply run all of the cells in the notebook to create a network-calibrated version of each synthetic dataset.